

LARGE EDDY SIMULATION OF OSCILLATORY FLOW OVER A MOBILE RIPPLED BED
USING AN EULER-LAGRANGE APPROACH

A Dissertation Presented

by

Daniel Stokes Hagan

to

The Faculty of the Graduate College

of

The University of Vermont

In Partial Fulfillment of the Requirements
for the Degree of Doctor of Philosophy
Specializing in Mechanical Engineering

May, 2018

Defense Date: January 9, 2018
Dissertation Examination Committee:

Yves Dubief, Ph.D., Advisor
Erik Monsen, Ph.D., Chairperson
Mandar Dewoolkar, Ph.D.
Douglas Fletcher, Ph.D.
Cynthia J. Forehand, Ph.D., Dean of the Graduate College

Abstract

A volume-filtered Large-Eddy Simulation (LES) of oscillatory flow over a rippled mobile bed is conducted using an Euler-Lagrange approach. As in unsteady marine flows over sedimentary beds, the experimental data, referenced in this work for validation, shows quasi-steady state ripples in the sand bed under oscillatory flow. This work approximately reproduces this configuration with a sinusoidal pressure gradient driven flow and a sinusoidally rippled bed of particles. The LES equations, which are volume-filtered to account for the effect of the particles, are solved on an Eulerian grid, and the particles are tracked in a Lagrangian framework. In the Discrete Particle Method (DPM) used in this work, the particle collisions are handled by a soft-sphere model, and the liquid and solid phases are coupled through volume fraction and momentum exchange terms. Comparison of the numerical results to the experimental data show that the LES-DPM is capable of capturing the mesoscale features of the flow. The large scale shedding of vortices from the ripple peaks are observed in both datasets, which is reflected in the good quantitative agreement between the wall-normal flow statistics, and good qualitative agreement in ripple shape evolution. Additionally, the numerical data provides three insights into the complex interaction between the three-dimensional flow dynamics and bed morphology: (1) there is no observable distinction between reptating and saltating particle velocities, angular velocities or observed Shields parameters; (2) the potential motion of the mobile bed may create issues in the estimation of the bed shear stress used in classical models; and, (3) a helical pairing of vortices is observed, heretofore not known to have been identified in this type of flow configuration.

Citations

Material from this dissertation will be submitted for publication in peer-reviewed journals at the beginning of 2018 in the following form:

Hagan, D., Dubief, Y., Desjardins, O., Wengrove, M.. (2018). LES of oscillatory flow over a rippled bed using an Euler-Lagrange approach. *Journal of Fluids Engineering*.

Hagan, D., Dubief, Y., Desjardins, O., Wengrove, M.. (2018). Defining the fluid-bed interface and calculating bed shear stress. *Journal of Geophysical Research*.

Hagan, D., Dubief, Y., Desjardins, O., Wengrove, M.. (2018). Helical pairing instability in a rough-wall oscillatory flow. *Journal of Turbulence*.

Table of Contents

Citations	ii
List of Figures	1
1 Introduction, Literature Review, and Motivation	1
1.1 Introduction	1
1.2 Literature Review	2
1.2.1 General scour and bedforms	2
1.2.2 Ripple formation: Unidirectional flow	8
1.2.3 Ripple formation: Oscillatory flow	14
1.3 Motivation	18
2 Methodology & Results	20
2.1 Governing Equations & Numerical Methodology	20
2.1.1 Gas/Fluid Phase	21
2.1.2 Low-Pass Filtering	22
2.1.3 Filtered Incompressible Navier-Stokes Equations	23
2.1.4 Smagorinsky Model	24
2.1.5 Germano's Dynamic Smagorinsky Model	25
2.1.6 Lagrangian Averaging	28
2.1.7 Solid Phase	29
2.1.8 Momentum exchange	30
2.1.9 Collision Model	32
2.1.10 Adhesion Model	34
2.1.11 Fluid and Solid Coupling	35
2.1.12 Operating parameters	36
2.2 Simulation Configuration & Methodology	37
2.3 Results	41
2.3.1 Data Analysis	41
2.3.2 Flow Evolution, Vorticity, Velocity Streamlines	42
2.3.3 Wall-Normal Flow Statistics	50
2.3.4 Bed Shear Stress	56
2.3.5 Q-Criterion & Vortex Identification	61
2.3.6 Fluid-Bed Interface	64
2.3.7 Ripple Shape Comparison	67
2.3.8 Characterization of Ripple Erosion	70
2.3.9 Potential Sources of Error	74
2.4 Conclusion	77

3 Ongoing Work & Plan for Publications	79
3.0.1 Viability of LES-DPM for this Flow Configuration	79
3.0.2 Ongoing Work: Bed Shear Stress	79
3.0.3 Ongoing Work: Helical Vortex Pairing	80
3.0.4 Ongoing Work: Integral Method Analysis	83
3.0.5 Plan for Publications	83
3.0.6 Future Work	84
Bibliography	85
Appendices	91
A Additional Wall-Normal Statistics	91
A.1 Wall-Normal Locations of Maximum Streamwise Velocities	91
A.2 Wall-Normal TKE Profiles at Different Locations on Ripple	92
A.3 Wall-Normal Reynolds Stress Profiles at Different Locations on Ripple	95
A.4 Wall-Normal Profiles of Reynolds stresses (Wall-Normal, Streamwise, Spanwise) at Different Locations on Ripple	97
B Integral Method	107
B.1 Fukagata Integral approach for two-dimensional wall-bounded flows	107
C Nelder-Mead Optimization technique	109
C.1 Rosenbrock function example	111
C.2 Application to Integral Method	111
D 1D $k - \epsilon$ turbulence model code	113
D.1 Governing Equations	113
D.2 Reynolds Averaged Navier-Stokes (RANS) Equations	114
D.3 Boussinesq approximation for the Reynolds stress tensor	116
D.4 High Reynolds number $k - \epsilon$ turbulence model	117
D.5 Low Reynolds number $v^2 - f$ $k - \epsilon$ turbulence model	118
D.6 Low Reynolds Launder-Sharma $k - \epsilon$ turbulence model	119
D.7 $k - \omega$ turbulence model	120
D.8 1D RANS Equations	120
D.9 Algorithm	121

D.10 Boundary Conditions	122
D.11 Discretization	122
D.12 The tridiagonal system	123
D.13 Solving the tridiagonal system using the Thomas algorithm	125
D.14 Simulation parameters	126

List of Figures

1.1	Naturally occurring ripples in a sand bed under wave motion. Photo taken in Puerto Rico by Meagan Wengrove.	2
1.2	Flow over a backward facing step, with sand filled behind the step, is generated by a sluice gate. Erosion is observed directly behind the step, and the sand aggregates downstream of the scour hole in a mound. Nik Hassan and Narayanan (1985).	3
1.3	A boundary layer flows past an circular cross-sectioned verticle pier. A scour hole is observed in a teardrop shape around the pier. Briaud et al. (1999).	4
1.4	Flow over a horizontal circular cross-sectioned pipeline. Small scale scouring is observed below the pipeline, until the scouring reaches a threshold at which underflow of the fluid occurs and exponentially scours below the pipeline. Mounds are observed both upstream and downstream of the pipeline. Chiew (1990).	5
1.5	In LES, the smallest scales of the flow are modeled with sub-grid scale models. If a flow structure is smaller than the computational grid sizing, the grid can not resolve it, and it must be modeled.	6
1.6	Predictions of scour hole for flow over a horizontal circular cross-sectioned pipeline. The squares represent the experimental data, and lines are numerical results. Although the treatment of bed as a continuum results in decent scour hole predictions, the mound that forms directly behind the scour hole is not well predicted. This solid phase modeling does not accurately predict the mound's size, or even its existence, depending of if RANS or LES is used to model the fluid flow. Liang et al. (2005).	8
1.7	Experimental ripple formation and migration of an erodible bed, under directional flow. Florez and de Moraes Franklin (2016).	10
1.8	Ripple formation in a particle bed at the bottom of circular pipe. The results of the LES-DPM simulation show good agreement with experimental data, and demonstrate the validity of this method for predicting ripple formation. Arolla and Desjardins (2015).	12
1.9	Fully resolved DNS-IB simulation of directional flow over a particle bed. Due to excessively high computational cost, a very small domain was used, and no bedforms were observed. Derkse (2015).	12
1.10	Fully resolved DNS-IB simulation of directional flow over a particle bed. The authors published two different papers with varying domain size, showing that the domain size was still affecting the magnitude of the bedforms, indicating that domain size, and thus computational feasibility, can still be an issue for fully resolved simulations. Kidanemariam and Uhlmann (2014).	13
1.11	Analytical solution streamwise velocity profiles in oscillatory flow between two infinite plates. Y is the wall-normal direction, and the walls are located at positions $Y = \pm 1$. The profiles are shown for the first half of the oscillation period, at phase times $\varphi = \frac{n\pi}{4}$, for $n = 0, 1, 2, 3$. DiLiberto and Ciafalo (2009).	14
1.12	Two-dimensional, non-turbulent analytical solution of oscillatory flow over a sinusoidally rippled bed. The streamlines show a vortex form on the downstream side of the ripple, which is shed back in the free flow when the flow reverses directions. Blondeaux and Vittori (1991).	16
1.13	Two-dimensional, non-turbulent analytical solution of oscillatory flow over a sinusoidally rippled bed. The vorticity shows a vortex form on the downstream side of the ripple, which collides and pairs with a second vortex when the flow reverses directions, and then both are shed back to the free flow. Blondeaux and Vittori (1991).	17

1.14	Fully resolved DNS-IB simulation of oscillatory flow of particle chains, initially oriented in the streamwise direction. As the flow develops, the chains are reoriented to align in the spanwise direction. Mazzuoli et al. (2016).	18
2.1	(a) Tenneti's drag coefficient for a range of Re_p . (b) Semilog plot of the drag coefficient. $Re_p = 100$ (red), $Re_p = 200$ (blue), $Re_p = 300$ (green), $Re_p = 400$ (black), $Re_p = 500$ (magenta), and power law fit of $Re_p = 100$ (dashed black). In this work, $Re_{p,max} \simeq 300$, and $\psi_p \leq 0.7$. For these conditions, the relationship between the ψ_p and F follows a power law fit, with $\alpha = 4.516$	32
2.2	Soft-sphere model collision between two different sized particles. Once the particles overlap an amount δ , or are within the buffer region λ_{col} of each other, a spring force is generated between them.	33
2.3	Experimental setup in the small-oscillatory flow tunnel at the Naval Research Laboratory. The test section is monitored by the laser and high-speed cameras of the PIV system. Photo courtesy of the Naval Research Laboratory and Frank et al.	38
2.4	Time evolution of the freestream streamwise velocity. The experimental values are denoted by the blue line, the numerical results are represented by the red line. There is some variation in the symmetry and magnitude of the experimental velocity.	38
2.5	Initial configuration of the simulation. The flow is driven by a sinusoidal pressure gradient in the streamwise direction. The morphology of the particle bed is initially sinusoidal.	40
2.6	Packing configuration of the particle bed. The flat stretch of bed shown here is meant only to illuminate the BCC packing structure of the bed, and is not used in the simulation.	41
2.7	Numerical 2D spanwise-averaged vorticity, shown at phase angles $\frac{n\pi}{4}$, for $n = 0, 1, \dots, 6, 7$. The data is normalized by the particle diameter in both directions. The formation of shear layers at the ripple crest is even more evident than in the experimental data. The formation of the vortices off the ripple crest can be seen clearly, and in addition, as the flow changes directions, the old vortices are shed into the free stream, as at phase angle $5\pi/4$	44
2.8	Numerical velocity field overlayed on vorticity, shown at phase angles $\frac{n\pi}{4}$, for $n = 0, 1, \dots, 6, 7$. The data is normalized by the particle diameter in both directions. The velocity field helps to identify the shed vortices.	45
2.9	Experimental vorticity, shown at phase angles $\frac{n\pi}{4}$, for $n = 0, 1, \dots, 6, 7$. The data is normalized by the particle diameter in both directions. The formation of shear layers at the ripple crest is seen at phase angles in which the pressure gradient is producing higher free stream velocities. The resulting vortex shedding, can be seen most clearly at phase angles $\pi/2, 3\pi/4, 3\pi/2$, and $7\pi/4$	46
2.10	Experimental velocity field overlayed on vorticity, shown at phase angles $\frac{n\pi}{4}$, for $n = 0, 1, \dots, 6, 7$. The data is normalized by the particle diameter in both directions. The velocity field helps to identify the shed vortices at phase angles $3\pi/4$ and $7\pi/4$	47
2.11	Numerical velocity streamlines overlayed on the 2D spanwise-averaged velocity field, shown at phase angles $\frac{n\pi}{4}$, for $n = 0, 1, \dots, 6, 7$. Only a single ripple is shown, and the data is normalized by the particle diameter in both directions.	48
2.12	Experimental velocity streamlines overlayed on the velocity field, shown at phase angles $\frac{n\pi}{4}$, for $n = 0, 1, \dots, 6, 7$. The data is normalized by the particle diameter in both directions.	49

2.13 Streamwise velocity profiles in the wall-normal direction, at the ripple crest, shown at phase angles $\frac{n\pi}{4}$, for $n = 0, 1, \dots, 6, 7$. The velocity is normalized by the maximum achieved freestream streamwise velocity, U_∞ . The wall-normal position is normalized by the half-height of the channel, h . The experimental results are denoted by a blue line, and the numerical results by a red line. In some cases, the range of the PIV data was limited, therefore, the entire profile was not available.	51
2.14 Streamwise velocity profiles in the wall-normal direction, at the ripple trough, shown at phase angles $\frac{n\pi}{4}$, for $n = 0, 1, \dots, 6, 7$. The velocity is normalized by the maximum achieved freestream streamwise velocity, U_∞ . The wall-normal position is normalized by the half-height of the channel, h . The experimental results are denoted by a blue line, and the numerical results by a red line. In some cases, the range of the PIV data was limited, therefore, the entire profile was not available.	52
2.15 Streamwise velocity profiles in the wall-normal direction, at the ripple face, shown at phase angles $\frac{n\pi}{4}$, for $n = 0, 1, \dots, 6, 7$. The velocity is normalized by the maximum achieved freestream streamwise velocity, U_∞ . The wall-normal position is normalized by the half-height of the channel, h . The experimental results are denoted by a blue line, and the numerical results by a red line. In some cases, the range of the PIV data was limited, therefore, the entire profile was not available.	53
2.16 Streamwise velocity profiles in the wall-normal direction, averaged over the entire wavelength of the ripple, shown at phase angles $\frac{n\pi}{4}$, for $n = 0, 1, \dots, 6, 7$. The velocity is normalized by the maximum achieved freestream streamwise velocity, U_∞ . The wall-normal position is normalized by the half-height of the channel, h . The experimental results are denoted by a blue line, and the numerical results by a red line. In some cases, the range of the PIV data was limited, therefore, the entire profile was not available.	54
2.17 Turbulent kinetic energy (TKE) wall-normal profiles, averaged over the entire wavelength of the ripple, shown at phase angles $\frac{n\pi}{4}$, for $n = 0, 1, \dots, 6, 7$. The TKE is normalized by the square of the maximum achieved freestream streamwise velocity, U_∞ . The wall-normal position is normalized by the half-height of the channel, h . The experimental results are denoted by a red line, and the numerical results by a blue line. In some cases, the range of the PIV data was limited, therefore, the entire profile was not available.	54
2.18 Reynolds stress wall-normal profiles, averaged over the entire wavelength of the ripple, shown at phase angles $\frac{n\pi}{4}$, for $n = 0, 1, \dots, 6, 7$. The Reynold stress is normalized by the square of the maximum achieved freestream streamwise velocity, U_∞ . The wall-normal position is normalized by the half-height of the channel, h . The experimental results are denoted by a blue line, and the numerical results by a red line. In some cases, the range of the PIV data was limited, therefore, the entire profile was not available.	55
2.19 Bed shear stress over an immobile rippled bed, per Blondeaux (1991). The ripple peak are at the extants of the plot, and the ripple trough is centered. A no-slip condition is assumed at the bed-fluid interface. As the flow moves from left to right, a strong negative peak is observed on the downstream ripple face. Therefore, the fluid would compel the solid phase to move from the trough to the peak, thus maintaining or increasing the ripple peak. The opposite is observed when the flow reverses.	57
2.20 Bed-fluid interface and velocity field superimposed over the Q-criterion field. Only the right hand side of the a single ripple is shown. It becomes clear that there is still fluid velocity “within” the ripple as a vortex interacts with the ripple.	58

2.21	Simplified view of a vortex impacting the right hand side of a ripple. The vortex has been shed as the fluid moves from left to right, and then reverses directions. Depending on how the bed-fluid interface is defined, the sign of the calculated bed shear stress may be affected. For simplicity, x is interface-parallel, the y -direction is defined as the wall-normal, and the fluid velocity u is defined as parallel to the bed-fluid interfaces, in the negative x -direction.	59
2.22	Experimental bed shear stress (blue line), numerical bed shear stress (red line), and numerical top wall shear stress (green line), over a single ripple. The first half of the oscillation presents much closer qualitative bed shear stresses. There is phase lag, of approximately $\pi/4$, between top wall shear stress and the pressure gradient forcing, as the top wall shear stress does not go to zero until phase angles $\pi/4$ and $5\pi/4$	60
2.23	Numerical free stream velocity (thick blue line) and the evolution of bed shear stress at different locations on the ripple. The top wall is denoted by magenta line and diamond marker, the ripple crest is denoted by the black line with square marker, the ripple trough is denoted by the blue line with circle marker, and the ripple face is denoted by the red line with triangle marker. A phase lag of $\pi/4$ is observed between the bed shear stress at the top wall and the free stream velocity. By contrast, the further down the ripple, the greater the phase lead between the bed shear stress and the freestream velocity.	61
2.24	Numerical Q-criterion isocontours at phase time 0. Free stream velocity is zero.	63
2.25	Numerical Q-criterion isocontours at phase time $\pi/4$. The fluid is accelerating from left to right.	64
2.26	Numerical Q-criterion isocontours at phase time $\pi/2$. The fluid has achieve maximum free stream velocity, from left to right.	64
2.27	Numerical Q-criterion isocontours at phase time $3\pi/4$. The fluid is decelerating, but is still moving from left to right.	65
2.28	Numerical Q-criterion isocontours at phase time π . The freestream velocity has decelerated to zero, and is about to begin accelerating from right to left.	65
2.29	Numerical bed interface, as determined by assuming the bed has a solid volume fraction $\langle \psi_p \rangle = \langle \psi_p \rangle_{threshold}$. The data has been normalized by the particle diameter.	66
2.30	Experimental and numerical ripple comparison. The numerical ripple is space and phase-time averaged. The data has been normalized by the particle diameter. The blue line denotes experimental data, the red line denotes numerical data.	68
2.31	The locations of the ripple peaks are compared. The biggest discrepancy is seen at phase time $5\pi/4$, where the locations differ by roughly $3d_p$. The data has been normalized by the particle diameter. Blue circles denote the experimental data, and red triangles denote the numerical data.	69
2.32	Best-fit circles are used to determine the radius of curvature of ripples at their peaks, shown at phase angles $\frac{n\pi}{4}$, for $n = 0, 1, \dots, 6, 7..$ The data has been normalized by the particle diameter. The blue line denotes experimental data, the red line denotes numerical data.	70
2.33	The evolution of the best-fit circles, used to determine the radius of curvature of ripples at their peaks, are shown over a whole period. The data has been normalized by the particle diameter. The blue line denotes experimental data, the red line denotes numerical data. The first half period shows good qualitative agreement between the radii of curvature. However, the second half does not.	71
2.34	Numerical bed interface and the particles that have been eroded by the flow, at phase angle $\pi/4$. Reptating, or sliding and/or rolling, particles are red. Particles that are saltating, or momentarily entrained before returning to the bed, are blue. The data has been normalized by the particle diameter.	72

2.35	Saltating and reptating particle velocities, at phase angle $\pi/4$. The particle velocities are normalized by the maximum freestream velocity, and the particle positions are normalized by the particle diameter. Red denotes reptation, and blue denotes saltation.	72
2.36	Velocity distributions, shown at phase angles $\frac{n\pi}{4}$, for $n = 0, 1, \dots, 6, 7$. The red line denotes reptating particles, the blue line denotes saltating particles, and the black line denotes all eroded particles (reptating plus saltating particles). The particle velocities are normalized by the maximum freestream velocity.	73
2.37	Saltating and reptating particle angular velocities, at phase angle $\pi/4$. The particle positions are normalized by the particle diameter. Red denotes reptation, and blue denotes saltation.	74
2.38	Particle angular velocity distributions, shown at phase angles $\frac{n\pi}{4}$, for $n = 0, 1, \dots, 6, 7$. The red line denotes reptating particles, the blue line denotes saltating particles, and the black line denotes all eroded particles (reptating plus saltating particles).	75
2.39	Shields parameter distributions, shown at phase angles $\frac{n\pi}{4}$, for $n = 0, 1, \dots, 6, 7$. The red line denotes reptating particles, the blue line denotes saltating particles, and the black line is the all eroded particles (reptating plus saltating particles).	76
3.1	Schematic of intertwining vortices in a shear layer, per the work of Comte et al. (1992). . . .	81
3.2	Helical pairing of vortices at phase time $\frac{8\pi}{12}$. One vortex is shed from the ripple, and as the flow reverses, the newly formed shear layer develops into a second vortex, which interacts with the existing vortex and the two become entwined.	81
3.3	Helical pairing of vortices at phase time $\frac{9\pi}{12}$. One vortex is shed from the ripple, and as the flow reverses, the newly formed shear layer develops into a second vortex, which interacts with the existing vortex and the two become entwined.	82
3.4	Helical pairing of vortices at phase time $\frac{10\pi}{12}$. One vortex is shed from the ripple, and as the flow reverses, the newly formed shear layer develops into a second vortex, which interacts with the existing vortex and the two become entwined.	82
A.1	Maximum velocities of streamwise profiles, averaged over the entire wavelength of the ripple, shown at phase angles $\frac{n\pi}{4}$, for $n = 0, 1, \dots, 6, 7$. The velocities are normalized by the maximum achieved freestream streamwise velocity, U_∞ . The wall-normal position is normalized by the particle diameter. The experimental data is denoted by blue triangles, and the numerical results by red circles.	92
A.2	Turbulent kinetic energy (TKE) wall-normal profiles, at the ripple crest, shown at phase angles $\frac{n\pi}{4}$, for $n = 0, 1, \dots, 6, 7$. The TKE is normalized by the square of the maximum achieved freestream streamwise velocity, U_∞ . The wall-normal position is normalized by the half-height of the channel, h . The experimental results are denoted by a red line, and the numerical results by a blue line. In some cases, the range of the PIV data was limited, therefore, the entire profile was not available.	93
A.3	Turbulent kinetic energy (TKE) wall-normal profiles, at the ripple trough, shown at phase angles $\frac{n\pi}{4}$, for $n = 0, 1, \dots, 6, 7$. The TKE is normalized by the square of the maximum achieved freestream streamwise velocity, U_∞ . The wall-normal position is normalized by the half-height of the channel, h . The experimental results are denoted by a red line, and the numerical results by a blue line. In some cases, the range of the PIV data was limited, therefore, the entire profile was not available.	93

A.4	Turbulent kinetic energy (TKE) wall-normal profiles, at the ripple face, shown at phase angles $\frac{n\pi}{4}$, for $n = 0, 1, \dots, 6, 7$. The TKE is normalized by the square of the maximum achieved freestream streamwise velocity, U_∞ . The wall-normal position is normalized by the half-height of the channel, h . The experimental results are denoted by a red line, and the numerical results by a blue line. In some cases, the range of the PIV data was limited, therefore, the entire profile was not available.	94
A.5	Reynolds stress wall-normal profiles, at the ripple crest, shown at phase angles $\frac{n\pi}{4}$, for $n = 0, 1, \dots, 6, 7$. The Reynolds stress is normalized by the square of the maximum achieved freestream streamwise velocity, U_∞ . The wall-normal position is normalized by the half-height of the channel, h . The experimental results are denoted by a blue line, and the numerical results by a red line. In some cases, the range of the PIV data was limited, therefore, the entire profile was not available.	95
A.6	Reynolds stress wall-normal profiles, at the ripple trough, shown at phase angles $\frac{n\pi}{4}$, for $n = 0, 1, \dots, 6, 7$. The Reynolds stress is normalized by the square of the maximum achieved freestream streamwise velocity, U_∞ . The wall-normal position is normalized by the half-height of the channel, h . The experimental results are denoted by a blue line, and the numerical results by a red line. In some cases, the range of the PIV data was limited, therefore, the entire profile was not available.	96
A.7	Reynolds stress wall-normal profiles, at the ripple face, shown at phase angles $\frac{n\pi}{4}$, for $n = 0, 1, \dots, 6, 7$. The Reynolds stress is normalized by the square of the maximum achieved freestream streamwise velocity, U_∞ . The wall-normal position is normalized by the half-height of the channel, h . The experimental results are denoted by a blue line, and the numerical results by a red line. In some cases, the range of the PIV data was limited, therefore, the entire profile was not available.	96
A.8	Reynolds wall stress wall-normal profiles, at the ripple crest, shown at phase angles $\frac{n\pi}{4}$, for $n = 0, 1, \dots, 6, 7$. The Reynolds wall stress is normalized by the square of the maximum achieved freestream streamwise velocity, U_∞ . The wall-normal position is normalized by the half-height of the channel, h . The experimental results are denoted by a blue line, and the numerical results by a red line. In some cases, the range of the PIV data was limited, therefore, the entire profile was not available.	98
A.9	Reynolds wall stress wall-normal profiles, at the ripple trough, shown at phase angles $\frac{n\pi}{4}$, for $n = 0, 1, \dots, 6, 7$. The Reynolds wall stress is normalized by the square of the maximum achieved freestream streamwise velocity, U_∞ . The wall-normal position is normalized by the half-height of the channel, h . The experimental results are denoted by a blue line, and the numerical results by a red line. In some cases, the range of the PIV data was limited, therefore, the entire profile was not available.	98
A.10	Reynolds wall stress wall-normal profiles, at the ripple face, shown at phase angles $\frac{n\pi}{4}$, for $n = 0, 1, \dots, 6, 7$. The Reynolds wall stress is normalized by the square of the maximum achieved freestream streamwise velocity, U_∞ . The wall-normal position is normalized by the half-height of the channel, h . The experimental results are denoted by a blue line, and the numerical results by a red line. In some cases, the range of the PIV data was limited, therefore, the entire profile was not available.	99
A.11	Reynolds wall stress wall-normal profiles, averaged over the entire wavelength of the ripple, shown at phase angles $\frac{n\pi}{4}$, for $n = 0, 1, \dots, 6, 7$. The Reynold wall stress is normalized by the square of the maximum achieved freestream streamwise velocity, U_∞ . The wall-normal position is normalized by the half-height of the channel, h . The experimental results are denoted by a blue line, and the numerical results by a red line. In some cases, the range of the PIV data was limited, therefore, the entire profile was not available.	100

A.12 Reynolds streamwise stress wall-normal profiles, at the ripple crest, shown at phase angles $\frac{n\pi}{4}$, for $n = 0, 1, \dots, 6, 7$. The Reynolds wall stress is normalized by the square of the maximum achieved freestream streamwise velocity, U_∞ . The wall-normal position is normalized by the half-height of the channel, h . The experimental results are denoted by a blue line, and the numerical results by a red line. In some cases, the range of the PIV data was limited, therefore, the entire profile was not available. 101

A.13 Reynolds streamwise stress wall-normal profiles, at the ripple trough, shown at phase angles $\frac{n\pi}{4}$, for $n = 0, 1, \dots, 6, 7$. The Reynolds wall stress is normalized by the square of the maximum achieved freestream streamwise velocity, U_∞ . The wall-normal position is normalized by the half-height of the channel, h . The experimental results are denoted by a blue line, and the numerical results by a red line. In some cases, the range of the PIV data was limited, therefore, the entire profile was not available. 101

A.14 Reynolds streamwise stress wall-normal profiles, at the ripple face, shown at phase angles $\frac{n\pi}{4}$, for $n = 0, 1, \dots, 6, 7$. The Reynolds wall stress is normalized by the square of the maximum achieved freestream streamwise velocity, U_∞ . The wall-normal position is normalized by the half-height of the channel, h . The experimental results are denoted by a blue line, and the numerical results by a red line. In some cases, the range of the PIV data was limited, therefore, the entire profile was not available. 104

A.15 Reynolds streamwise stress wall-normal profiles, averaged over the entire wavelength of the ripple, shown at phase angles $\frac{n\pi}{4}$, for $n = 0, 1, \dots, 6, 7$. The Reynold wall stress is normalized by the square of the maximum achieved freestream streamwise velocity, U_∞ . The wall-normal position is normalized by the half-height of the channel, h . The experimental results are denoted by a blue line, and the numerical results by a red line. In some cases, the range of the PIV data was limited, therefore, the entire profile was not available. 102

A.16 Reynolds spanwise stress wall-normal profiles, at the ripple crest, shown at phase angles $\frac{n\pi}{4}$, for $n = 0, 1, \dots, 6, 7$. The Reynolds spanwise stress is normalized by the square of the maximum achieved freestream streamwise velocity, U_∞ . The wall-normal position is normalized by the half-height of the channel, h . The experimental results are denoted by a blue line, and the numerical results by a red line. In some cases, the range of the PIV data was limited, therefore, the entire profile was not available. 103

A.17 Reynolds spanwise stress wall-normal profiles, at the ripple trough, shown at phase angles $\frac{n\pi}{4}$, for $n = 0, 1, \dots, 6, 7$. The Reynolds spanwise stress is normalized by the square of the maximum achieved freestream streamwise velocity, U_∞ . The wall-normal position is normalized by the half-height of the channel, h . The experimental results are denoted by a blue line, and the numerical results by a red line. In some cases, the range of the PIV data was limited, therefore, the entire profile was not available. 104

A.18 Reynolds spanwise stress wall-normal profiles, at the ripple face, shown at phase angles $\frac{n\pi}{4}$, for $n = 0, 1, \dots, 6, 7$. The Reynolds spanwise stress is normalized by the square of the maximum achieved freestream streamwise velocity, U_∞ . The wall-normal position is normalized by the half-height of the channel, h . The experimental results are denoted by a blue line, and the numerical results by a red line. In some cases, the range of the PIV data was limited, therefore, the entire profile was not available. 105

A.19 Reynolds spanwise stress wall-normal profiles, averaged over the entire wavelength of the ripple, shown at phase angles $\frac{n\pi}{4}$, for $n = 0, 1, \dots, 6, 7$. The Reynold spanwise stress is normalized by the square of the maximum achieved freestream streamwise velocity, U_∞ . The wall-normal position is normalized by the half-height of the channel, h . The experimental results are denoted by a blue line, and the numerical results by a red line. In some cases, the range of the PIV data was limited, therefore, the entire profile was not available. 106

Chapter 1

Introduction, Literature Review, and Motivation

1.1 Introduction

Dune and ripple formation in aeolian and subaqueous mobile beds have implications in both industry and nature. This phenomenon can be found in industrial processes involving mobile beds disturbed by shear flow, such as pipelines. In nature, the erosion of riverbeds and the modification of coast lines, as well the formation of sand dunes in deserts, can be attributed to these same processes. Since the morphology of the mobile bed and the characteristics of the flow are coupled, understanding the influence of the bed on the flow is important. Ripples can be formed by unidirectional flow, as in rivers, or oscillatory flow, as in coastal areas, as in Figure 1.1. Although this work focuses on oscillatory flow, the mechanisms of ripple formation are similar to unidirectional flow. In both cases, instabilities in the bed are the catalyst for ripple formation. The irregularities in the bed, whether they be roughness or small scale bed forms, cause a phase lag between the shear stress at the bed interface and the morphology of the bed interface itself. This phase lag is a result of fluid inertia, and as the lag increases, the out of phase bed shear stress will pull sediment from the troughs to the peaks of the bed disturbances. As the peaks grow and the troughs deepen, the process is exacerbated by the now larger bed forms, completing a positive feedback loop. Once the ripples have formed, they strongly



Figure 1.1: Naturally occurring ripples in a sand bed under wave motion. Photo taken in Puerto Rico by Meagan Wengrove.

impact the flow dynamics. From an engineering perspective, it is highly desirable to understand and predict the effects of the bedform on the flow.

1.2 Literature Review

1.2.1 General scour and bedforms

Although the focus of this work is on subaqueous ripples, the work done, and approaches used, in the field of bed scour, are closely related. Much experimental work has been done, such as from a sluice gate over an apron (Nik Hassan and Narayanan 1985), and scour at different shaped structures, such as vertical piers (Briaud et al. 1999) and horizontal pipelines (Chiew 1990), as shown in Figures 1.2, 1.3, and 1.4, respectively. But, with advancements in computing capabilities and algorithm efficiency, numerical simulations have become a viable alternative to experimental research. Unlike an experiment, which requires probes and/or imaging capabilities to capture data from the system, Computational Fluid Dynamics (CFD) has the advantage of access to data at any time or place in the simulation. Numerical simulations also allow for easier parametric studies. CFD has its own limitations, e.g. boundary conditions, limited domain size, computational costs, etc. Yet CFD, with its access to full four-dimensional information, enables detailed investigation

into the physics at play and can be used as a complement to experimental or field observational work, providing access to information beyond the reach of experimental methods.

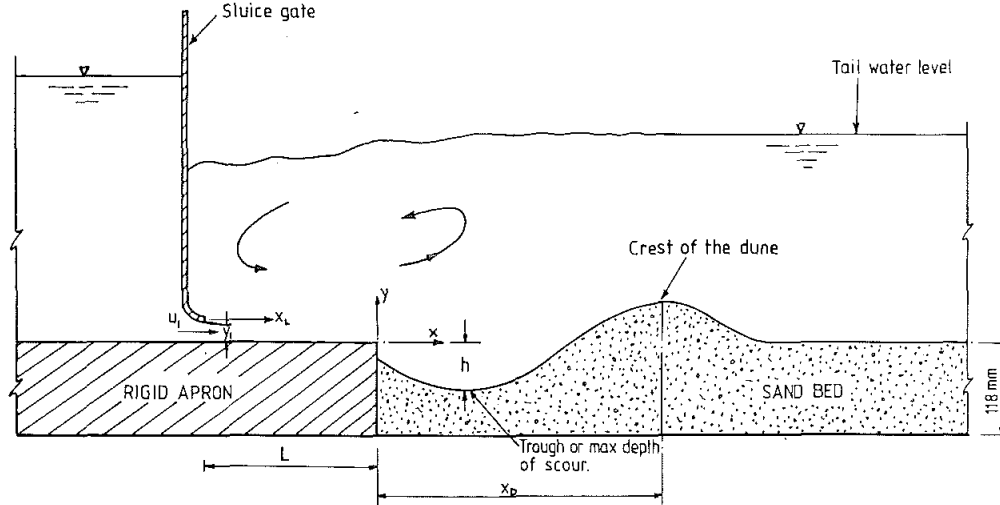


Figure 1.2: Flow over a backward facing step, with sand filled behind the step, is generated by a sluice gate. Erosion is observed directly behind the step, and the sand aggregates downstream of the scour hole in a mound. Nik Hassan and Narayanan (1985).

Numerical studies of scour have traditionally treated the sediment bed as a continuum, so the bed load, and if represented, the suspended load, are treated as scalar concentrations. The morphology of the sediment bed is governed by a bed load transport equation and the suspended load is governed by the convection-diffusion transport equation. The majority of the work that uses this bed load approach use either Reynolds Averaged Navier-Stokes (RANS) simulations or Large Eddy Simulation (LES) to model flow. It is important to note that these methods model all (RANS) or small-scale (LES) flow structures, and must rely on turbulence models for non-laminar flows. By design, RANS solvers use time-averaged equations. Flow variables are decomposed into two components, the time-averaged value, and the fluctuation. Therefore, RANS solvers cannot accurately predict strongly time-dependent phenomena, like the oscillatory flow over a rippled bed presented in this work. LES applies the flow variables through a low-pass filter, removing the small-scale structures. The large scales of the flow are fully resolved directly, but the small scales are modeled in order to reduce computational cost, per Figure 1.5. Since sediment scour occurs at the interface between the fluid and the sediment bed, exactly where the smallest scales of the flow are generated, LES may be filtering out

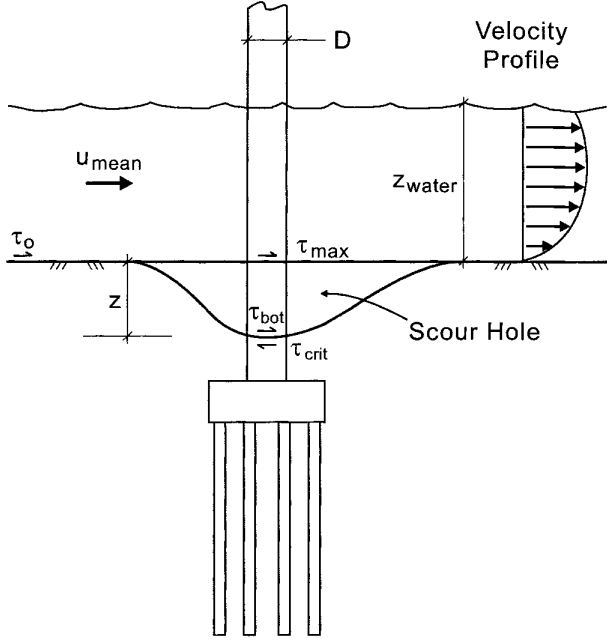


Figure 1.3: A boundary layer flows past an circular cross-sectioned verticle pier. A scour hole is observed in a teardrop shape around the pier. Briaud et al. (1999).

flow characteristics that are crucial to scouring processes. However, the literature has shown the capability of LES to describe the mesoscale features of the flow, as shown in the following sections.

Mutlu Sumer (2007) provides a good general review of mathematical and numerical bed load modeling. Tao and Yu (2013) have also compiled a thorough and clear review of these methods; a synopsis of this portion of their review follows. Although there are many variations of the bed load transport equations and approaches to couple the flow to the sediment phase, they are fundamentally similar in that they do not model the individual sediment particles. The heart of this method is based on the relationship between the sediment bed height and the rate of sediment flux. Paola and Voller (2005a) derived a generalized Exner equation for the mass balance of sediment:

$$\frac{\partial h}{\partial t} = -\frac{1}{1-\lambda} (\nabla \cdot \mathbf{q}) \quad (1.1)$$

Where h is the height of the sediment bed, λ is the porosity of the sediment bed, and \mathbf{q} is the sediment flux vector (containing both bed load and suspended load fluxes). See Tao and Yu (2013) for the various forms the

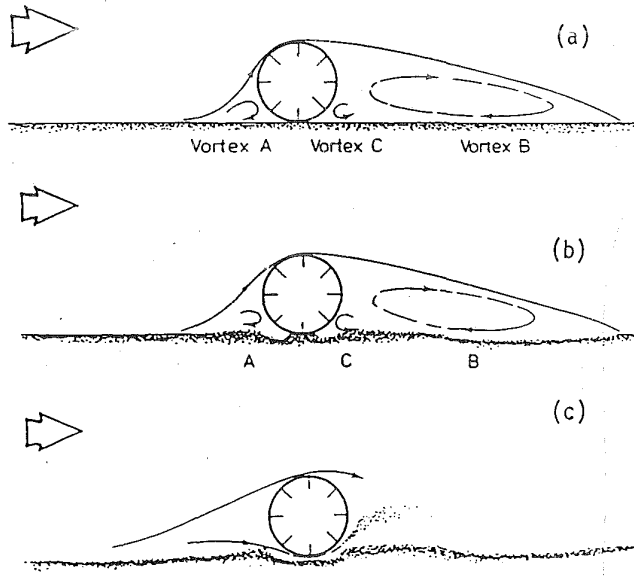


Figure 1.4: Flow over a horizontal circular cross-sectioned pipeline. Small scale scouring is observed below the pipeline, until the scouring reaches a threshold at which underflow of the fluid occurs and exponentially scours below the pipeline. Mounds are observed both upstream and downstream of the pipeline. Chiew (1990).

Exner equation can take. To determine the change to the sediment bed height, the flux \mathbf{q} must be determined. The sediment flux vector \mathbf{q} is a function of bed shear stress and the characteristics of the sediment (diameter, density, etc.), for which there are a variety of empirical formulas. Tao and Yu (2013) selected three such commonly used formulas, one of which is reproduced below in Equation 1.2. The Van Rijn equation (1984) assumes a constant critical bed shear stress, τ_b^* ,

$$\mathbf{q}_b^* = \frac{0.053}{d^{*0.3}} 8 \left(\frac{\tau_b - \tau_b^*}{\tau_b^*} \right) \quad (1.2)$$

For any formulation of bed sediment flux, \mathbf{q}_b^* , the direction of the flux is determined by the critical bed shear stress, τ_b^* , above which incipient sediment particle motion is observed. For a given sediment, the critical Shields stress number

$$\Theta^* = \frac{\tau_b^*}{(s-1)\rho_p g d^3} \quad (1.3)$$

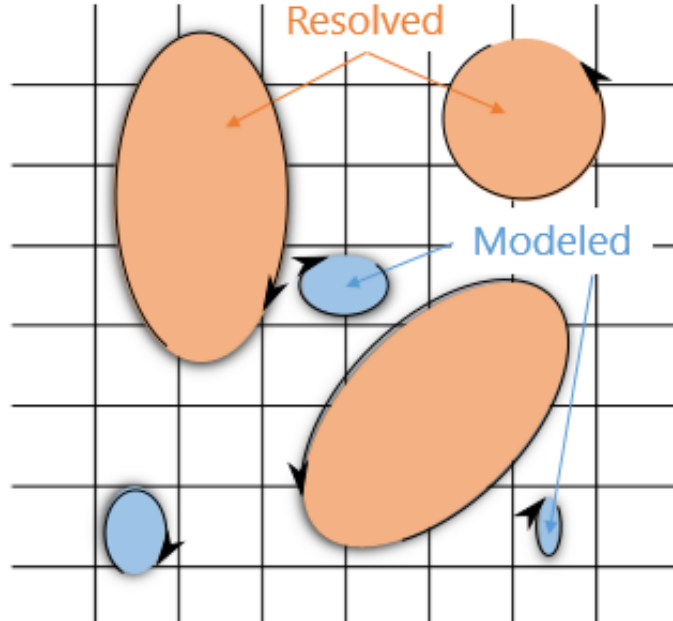


Figure 1.5: In LES, the smallest scales of the flow are modeled with sub-grid scale models. If a flow structure is smaller than the computational grid sizing, the grid can not resolve it, and it must be modeled.

defines this threshold. $\tau_b^* = \rho u_f^2$ is the critical bed shear stress, u_f is the shear velocity, s is the specific density of a sediment particle, ρ_p is the density of a sediment particle, d is the diameter, and g is gravity. If $\Theta > \Theta^*$ then there is motion of the sediment particles. Incipient motion can also be determined by use of critical velocity at or near the wall, rather than the critical bed shear stress. If the effects of the suspended load are not to be ignored, then any entrained sediment is governed by the transport equation:

$$\frac{\partial c}{\partial t} + \nabla \cdot (c\mathbf{u}) = \nabla \cdot (D\nabla c) \quad (1.4)$$

Where c is the suspended load concentration and D is the diffusivity.

Since the individual sediment particles themselves are not modeled, various physical effects of the bed morphology and flow structures are accounted for with correction factors. When the slope of the bed morphology takes on an angle greater than the angle of repose for the sediment, τ_b^* is multiplied by a slope correction factor to model the potential sliding of individual sediment particles and the increased exposure to the effects of the fluid. For highly turbulent flows, the effects of turbulence and lift forces are significant and must be addressed with additional correction factors, in the same form as that for slope correction. Thus,

to include the effects of bed slope angle, turbulence, and lift forces, the modified critical bed shear stress becomes

$$\tau_{b,modified}^* = (r_{slope} \cdot r_{turbulence} \cdot r_{lift}) \cdot \tau_b^* \quad (1.5)$$

Coupling the governing equations of the sediment to the flow has been done a couple of ways. The most commonly used method loosely couples the sediment bed load, suspended load, and bed morphology to the flow solver using the following algorithm (2013), whereby: (1) the flow field is solved with current bed morphology; (2) the change to the bed morphology is calculated with the Exner equation; (3) the flow-bed interface boundary is updated accordingly; and, (4) the flow field is solved for the new bed morphology.

The various forms of the bed load methodology have been used extensively in the literature. Olsen and Melaaen (1993), Olsen and Kjellesvig (1998), Roulund et al. (2005), and Liu and Garcia (2008) have simulated vertical circular piles using this technique. Olsen and Melaaen (1993) and Olsen and Kjellesvig (1998) used RANS flow solvers with a $k - \epsilon$ turbulence model, and Van Rijn's (1987) bed load concentration formulation in concert with the convection-diffusion transport equation for sediment concentration. Roulund et al. (2005) used a RANS flow solver with a $k - \omega$ turbulence model, and the bed load rate of Engelund and Fredsoe (1976). Liu and Garcia (2008) simulated 3D flow around a circular pile and 2D wall jet scour. They utilized a RANS flow solver with a $k - \epsilon$ turbulence model and the bed load rate of Engelund and Fredsoe (1976). Brørs (1999), Li and Cheng (1999), and Liang et al. (2005) have used the bed load methodology to simulate the flow and scour below a pipeline, which is represented by a cylinder lying on an erodible sediment bed axially perpendicular to the flow. In their work, Liang et al. show that treatment of the bed as a continuum, whether paired with RANS or LES flow solvers, while somewhat accurately modeling the scour hole depth under the horizontal pipeline, does not result in accurate predictions of the scour mound behind the scour hole. Brørs (1999) used a RANS flow solver with a $k - \epsilon$ turbulence model and a bed load transport rate for a horizontal bed with a slope correction factor. Li and Cheng (1999) use a potential flow model and an iterative process to model transient height of the sediment bed using a critical velocity methodology. Liang et al. (2005) compare the results of a RANS solver with a $k - \epsilon$ closure model against a spatially filtered Navier-Stokes solver with a sub-grid scale (SGS) model. Both solvers are coupled with the bed load rate model of Van Rijn (1987). Hogg et al. (1997) simulated a 2D turbulent wall jet over an erodible boundary

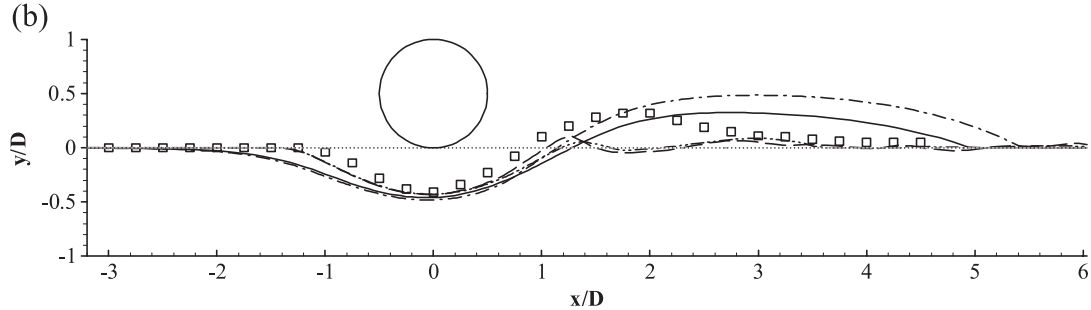


Figure 1.6: Predictions of scour hole for flow over a horizontal circular cross-sectioned pipeline. The squares represent the experimental data, and lines are numerical results. Although the treatment of bed as a continuum results in decent scour hole predictions, the mound that forms directly behind the scour hole is not well predicted. This solid phase modeling does not accurately predict the mound's size, or even its existence, depending of if RANS or LES is used to model the fluid flow. Liang et al. (2005).

using a RANS solver and the bed load transport rate of Meyer-Peter and Muller (1948). Chou and Fringer (2010) used LES and the bed load transport rate of Meyer-Peter and Muller (1948) to simulate a 3D turbulent boundary layer over an erodible surface.

An alternative numerical approach to the bed load transport method is the Discrete Particle Model (DPM), which is used in this work. The DPM treats the fluid as a continuum and the particles as distinct entities. The model is two-way coupled, whereby the fluid feels the effects of each particle, and each particle feels the effect of the the surrounding fluid. The model was pioneered by Cundall and Strack (1979). The details of the model are illustrated in Section 2.1, following the application by Pepiot and Desjardins (2012). Zhu et al. (2007, 2008) review the theoretical developments of the method and provide a summary of DPM applications and findings. The DPM has many applications, including fluidized beds (see the review of DPM application to fluidized beds by Deen et al. (2007)) and other particle-fluid flows. However, there has been limited application to the study of scour. Zamankhan (2009) used LES and DPM to simulate 3D flow over a pipeline, and found good agreement with experimental results.

1.2.2 Ripple formation: Unidirectional flow

Ripple formation under unidirectional flow has received substantial attention in the literature. Since the mechanism by which ripples form is based on an instability at the bed interface due to the inertia of the fluid, Benjamin (1959) calculated the phase lag of the bed shear stress over a wavy boundary. Kennedy (1963) developed an analytical model of flow over an erodible bed, and addressed the phase lag phenomena as

crucial to the formation of ripples at the bed interface. Thomas (1964) found that spherical particles resting at the bottom of a pipe would form “clumps or islands” at fluid velocities only slightly greater than that required for incipient motion, likely due to the phase lag of the bed shear.

Engelund and Fredsøe (1982) provide a review of bed formations including ripples, dunes, and antidunes. Charru et al. (2013) review sand ripples and dunes, formed mostly from unidirectional flows. Best (2005) provides a review of the fluid dynamics of river dunes, focused on mostly two-dimensional bedforms. As noted by Yalin (1977), bedforms are statistically two-dimensional in the spanwise direction. Church’s review of bed material transport and morphology of alluvial river channels (2006) breaks down the different types of bed transport (suspension, bedload, saltation) and defines them according to the non-dimensional Shields number, which determines the ability of the flow to cause transport of the particles in the bed.

Richards (1980) and Sumer and Bakioglu (1984) both use stability analysis on steady flow over an erodible bed, determining algebraic expressions for the flux of the erodible bed as a function of bed shear stress. Nakagawa and Tsujimoto (1984) used spectral analysis of experimental results to determine sediment wavelet lengths from the bed profile measurements.

Kuru et al. (1995) conducted a series of experiments of channel flow over an erodible bed and concluded that turbulence is not required for the formation of evolution of the bed from its initial flat configuration. Additionally, the authors found that increasing the flow rate did not dramatically alter the mechanisms that erode the bed. Coleman et al. (2003) conducted a series of experiments in which erodible bed development was measured for laminar and turbulent flows. They found that the sediment wavelet lengths, λ , are not dependent on the flow characteristics, but on the size of sediment. The sediment wavelet length is given by $\lambda = 175d^{0.75}$, where the wavelet length and sediment size, d , are both in millimeters. Coleman and Nikora (2009) conducted PIV-based experiments of turbulent and laminar flows. They found that seed waves, previously referred to as “wavelets”, which become ripples and/or dunes, develop in a two-stage process. The first stage consists of the motion of random patches of sediment due to attached eddies. The second stage involves the interactions of the patches, which lead to bed disturbances. These disturbances then generate more seed waves downstream. Florez and de Moraes Franklin (2016) experimentally investigate the formation and migration of ripples in a sand bed under fully developed turbulent flow in a closed conduit, finding that the celerity of ripple crests decrease with time, as the ripple wavelengths tend to increase. The ripples they observed are shown in Figure 1.7.

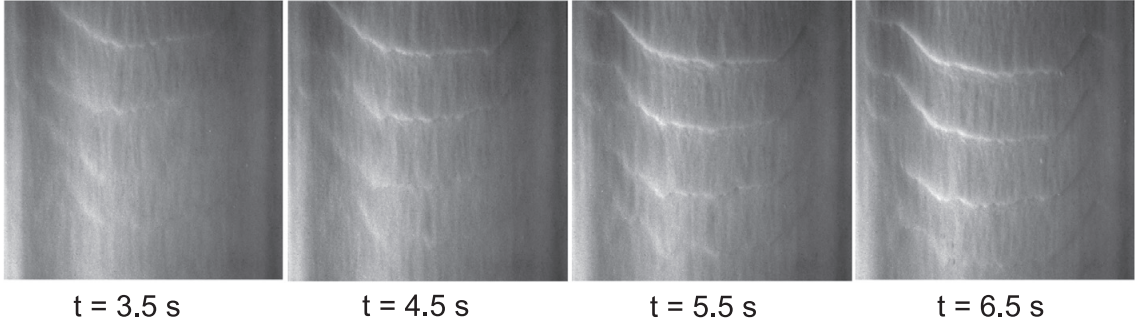


Figure 1.7: Experimental ripple formation and migration of an erodible bed, under directional flow. Florez and de Moraes Franklin (2016).

Charru and Hinch (2006a) propose a method to predict ripple formation by treating the sediment bed as scalar and using a conservation equation which contains erosion-rate and deposition-rate terms. The authors introduce a stabilizing term to account for the phenomena that ripples do not grow when the fluid viscosity is increased, which is a departure from the Exner approach (2005b) which places an algebraic dependence of the particle flux on the bed shear stress. In the second part of their study of ripple formation, Charru and Hinch (2006b) find that ripples can form in oscillating flow at flow velocities lower than that required in unidirectional flows. Zedler and Street (2001) performed a LES over an erodible bed, where the sediment was treated a scalar concentration, and its behavior modeled by a transport equation. Thus, the interaction between entrained sediment and the flow was neglected. Nonetheless, the results compared favorably to experimental results in the literature.

Yue et al. (2005) ran a LES over a two-dimensional dune, but the open channel flow free surface was tracked using a level-set method, finding that the depth of fluid above the dune had considerable impact on the flow structures. The work of Stoesser et al. (2008) is similar to that of Yue et al. (2005), a LES over two-dimensional dunes of similar dimensions. Observations included vortical separation from the peak of the dune and the “boil” phenomena originating from hairpin vortices. Khosronejad and Sotiropoulos (2014) use LES and sediment concentration transport equation, combined with an IB, to define the fluid-sediment interface. Fröhlich et al. (2005) use LES to simulate flow over a wall with periodic hill-like protrusions. Grigoriadis et al. (2009) performed an LES over fixed dunes, which were modeled using an immersed boundary technique. Unlike Stoesser et al. (2008) and Omidyeganeh and Piomelli (2011), Grigoriadis et al. (2009) did not find that the horseshoe vortices lead to “boils” at the surface. Omidyeganeh and Piomelli (2011) performed a LES

of flow over a two-dimensional dune, observing separation of flow at the dune peak, spanwise vortices in this separated shear layer, developing into horseshoe structures, the ejection of fluid between the legs of these structures known as “boils”, and, after reattachment, the generation of streamwise Taylor-Gortler vortices on upstream side of the dune.

Sun and Xiao (2016) demonstrate that modeling particles by volume-filtering the Navier-Stokes equations is able to capture the essential features of sediment transport at a fraction of the computational cost of fully resolving individual particles, as with immersed boundary techniques. Schmeeckle (2014) uses LES and momentum exchange between the particles and the fluid to show that saltation is not a good model for sediment transport in unidirectional flow. Instead, bed load, also known as surface creep or reptation, and entrainment, by turbulent structures called sweeps, are the main modes of sediment transport under higher Reynolds number unidirectional flows. Duran et al. (2012) use a two-way couple RANS-DEM solver to simulate turbulent sediment transport, but the effects of the particles on the surrounding fluid are excluded. Maurin et al. (2015) simulate low Shields number bedload transport, in which no particle entrainment occurs, by utilizing spatially-averaged Navier-Stokes equations to model the fluid in an Eulerian framework, and a DEM to model the particles in a Lagrangian framework.

Utilizing the same numerical code used in this work, Arolla and Desjardins (2015) modeled the liquid-slurry flow of particles at the bottom of a turbulent pipe. Per the previous work of Capecelatro and Desjardins (2013a), Arolla and Desjardins use volume-filtered Euler-Lagrange LES, where the simulations are four-way coupled, allowing for particle-particle soft sphere contact, particle-fluid, and fluid-particle interactions. The evolution of the liquid-bed interface is characterized through the statistical analysis of the flow velocity, particle concentration, and other parameters. Like the simulation that is the focus of this paper, Arolla and Desjardins (2015), the flow is resolved on a grid that is of the same order as the particle diameter. Capecelatro and Desjardins (2013c), while still coupling the particles with other particles and the fluid, showed the validity of this method for predicting bedforms, as shown if Figure 1.8. In the form of a code called NGA, these works all utilize the numerical methodology described in Desjardins et al. (2008), which is described in more detail in the Numerical Methodology Section 2.1.

Although limited, some numerical work has been conducted in which the solid phase is fully resolved. Derksen (2015) conducted full resolved DNS-IB simulations of the erosion of a granular bed by turbulent flow, per Figure 1.9. Simulations were conducted over a range of Shields numbers, but bedforms were not

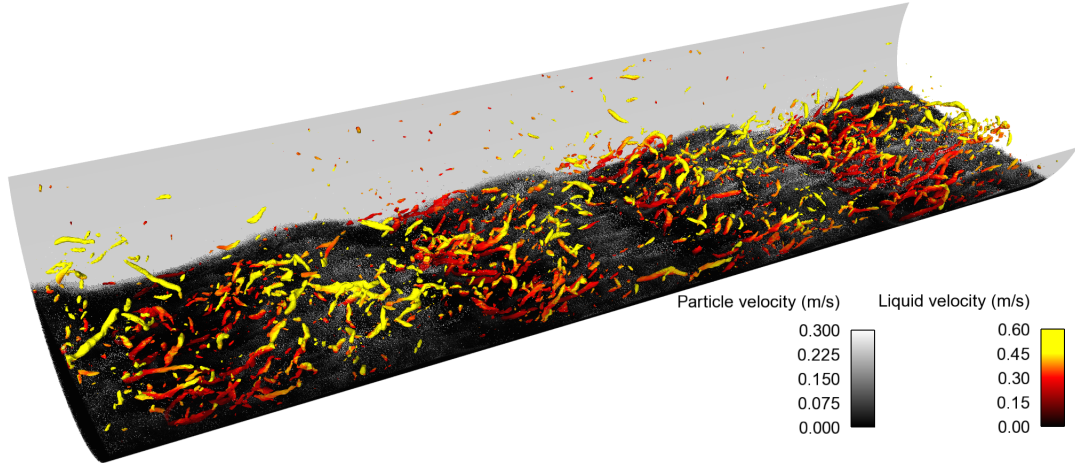


Figure 1.8: Ripple formation in a particle bed at the bottom of circular pipe. The results of the LES-DPM simulation show good agreement with experimental data, and demonstrate the validity of this method for predicting ripple formation. Arolla and Desjardins (2015).

captured due to the limited nature of the domain, which was only 45 particle diameters. Kidanemariam and

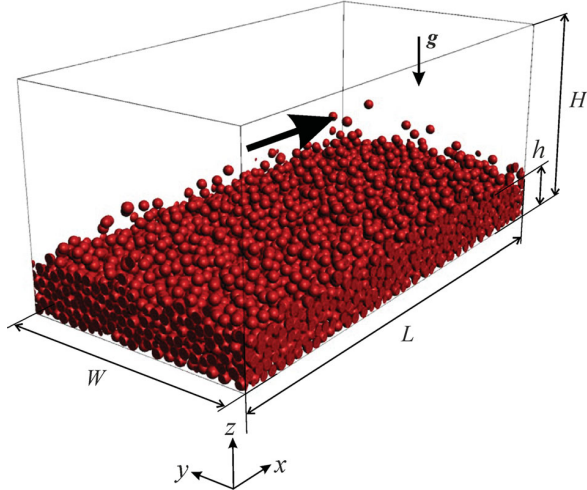


Figure 1.9: Fully resolved DNS-IB simulation of directional flow over a particle bed. Due to excessively high computational cost, a very small domain was used, and no bedforms were observed. Derksen (2015).

Uhlmann (2014) have conducted a fully resolved DNS of flow over a mobile sediment bed, as shown in Figure 1.10. The sediment particles are each individually resolved using an immersed boundary technique, and the simulations are four-way coupled, with particle-particle interactions using a soft-sphere contact model.

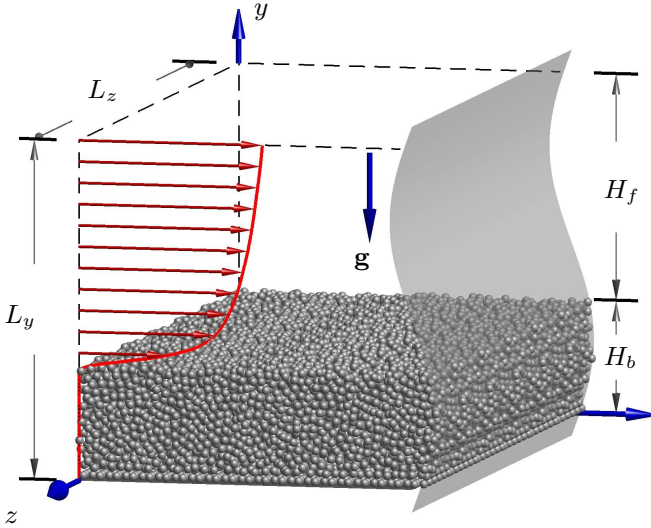


Figure 1.10: Fully resolved DNS-IB simulation of directional flow over a particle bed. The authors published two different papers with varying domain size, showing that the domain size was still affecting the magnitude of the bedforms, indicating that domain size, and thus computational feasibility, can still be an issue for fully resolved simulations. Kidanemariam and Uhlmann (2014).

The emergence of smaller dunes and larger “vortex” dunes were observed, and the wavelength, amplitude, and celerity of the emergent dunes were found to be in good agreement with experimental data. However, as the authors note, fully resolving all scales of the flow and sediment bed has a computational cost, and some goals are still a challenge, such as limits to domain size and simulation running time. Kidanemariam and Uhlmann (2017) continue by extending the computational domain, but otherwise using the same configuration as their previous work (2014). The minimum domain length that accommodated bed deformation showed pattern formation in the range of 75-100 particle diameters. In a much longer domain, the range is 100-110 particle diameters. Two regimes of pattern growth were identified. The initial growth regime is exponential and independent of the domain length. The second is nonlinear and strongly constrained by the domain length. The authors note that, for smaller domains, the second regime is steady, demonstrating a wavelength equal to the domain length.

1.2.3 Ripple formation: Oscillatory flow

The analytical solution to the canonical case of laminar oscillatory flow between two infinite flat plates was given by Landau and Lifshitz (1959). The more explicit derivation by Loudon and Tourdesillas (1998), and Figure 1.11, show the streamwise velocity profiles for the first half of the oscillation period, as shown by DiLiberto and Ciafalo (2009).

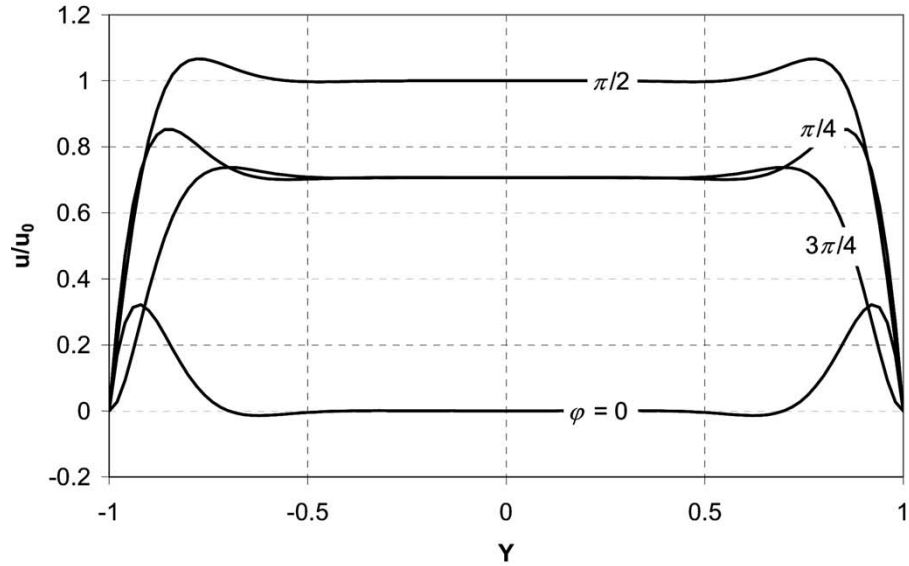


Figure 1.11: Analytical solution streamwise velocity profiles in oscillatory flow between two infinite plates. Y is the wall-normal direction, and the walls are located at positions $Y = \pm 1$. The profiles are shown for the first half of the oscillation period, at phase times $\varphi = \frac{n\pi}{4}$, for $n = 0, 1, 2, 3$. DiLiberto and Ciafalo (2009).

The study of the formation of ripples under oscillatory flow goes back to the seminal experimental work of Bagnold (1946), in which a section of a sandy bed was oscillated through still water, focusing on “vortex ripples” as opposed to “rolling grain” ripples. Vortex ripples have a much larger ripple amplitude to ripple wavelength ratio than rolling grain ripples. And, therefore, vortices are shed off these larger vortex ripples. The critical flow velocities and bed perturbation amplitudes were measured for a range of grain diameters and densities. These measurements were found to hew closely to an empirical model. Sleath (1976) continued the work of Bagnold (1946) by focusing on the rolling grain ripples that Bagnold did not. Sleath (1976) calculated the theoretical solution of oscillatory flow over an a rigid wavy bed, and conducted experiments by oscillating a bed in still water (which can be shown to be identical to oscillatory flow over a still bed). Gundogdu

and Carpinlioglu (1999a) (1999b) present a review of pulsatile flow theory, focusing on classifications and relevant experimental and theoretical work of the time.

Kaneko and Honji (1979) computed oscillatory flow over a wavy wall, finding that, when the ratio of the wavelength of the wavy wall to Stokes layer thickness was greater than 26, a “double structure” of upper and lower regions of recirculation was observed. The works of Sleath (1976) and Kaneko and Honji (1979) cite the steady streaming of the induced mean flow as the cause of ripple formation. This phenomena drags particles from the troughs to the peaks of the bed deformations, a positive feedback loop that causes the ripples to grow.

Sleath (1987) conducted experiments of oscillatory flow over rough beds, consisting of a single layer of fixed sand, gravel, or pebbles. Jensen et al. (1989) experimentally examine the effect of the Reynolds number on smooth walls and the effect of ratio of the amplitude of the oscillatory flow to the roughness of the wall for rough walls. The experimental work of Hino et al. (1976) on transition to turbulence showed that the critical Reynolds number for transition decreases with increasing frequency of oscillation. Hino et al. (1983) also noted the suppression of turbulence in the acceleration phase and the explosive and violent bursting motion at the beginning of the deceleration phase. Chen et al. (2007) experimentally studied the boundary layer structure of shallow open-channel flow over smooth and rough beds for a range of oscillatory periods, water depths and velocity amplitudes. Three stages were identified. The acceleration phase suppresses turbulence, the deceleration phase displays flame-like turbulent structures, and flow reversal. Dixen et al. (2008) experimentally investigate the effects of surface roughness, packing pattern, packing density, and number of layers of the roughness elements on an oscillating wave boundary layer. The authors found that the bed friction factor and boundary layer turbulence do not seem to be particularly sensitive to these parameters. In addition, the phase lag of bed friction velocity does not vary greatly with the ratio of oscillation amplitude to bed roughness. Corvaro et al. (2014) studied the turbulent structures in an oscillatory flow over a bed of plastic spheres.

Blondeaux (1990) and Vittori and Blondeaux (1990) use linear, and weakly nonlinear, stability analyses to create a predictive model of sand ripple formation, and their time development, under sea waves. But, as noted by Charru and Hinch (2006b), the lack of growth rate measurements, fundamental to testing stability theories, is problematic. In the second part of their study of ripple formation, Charru and Hinch (2006b) find that ripples can form in oscillating flow at flow velocities lower than that required in unidirectional flows.

Blondeaux and Vittori (1991) utilized the equations of Sleath (1984) to solve the vorticity equation and Poisson equation on a curvilinear grid over sinusoidal bed. The solution is purely two-dimensional and laminar, but the authors were able to describe the fundamental processes. In Figures 1.12 and 1.13, vortices are clearly shown to shed from the ripple crests. And, upon flow reversal, a pair of vortices, one old and one new, begin to be shed into the freestream.

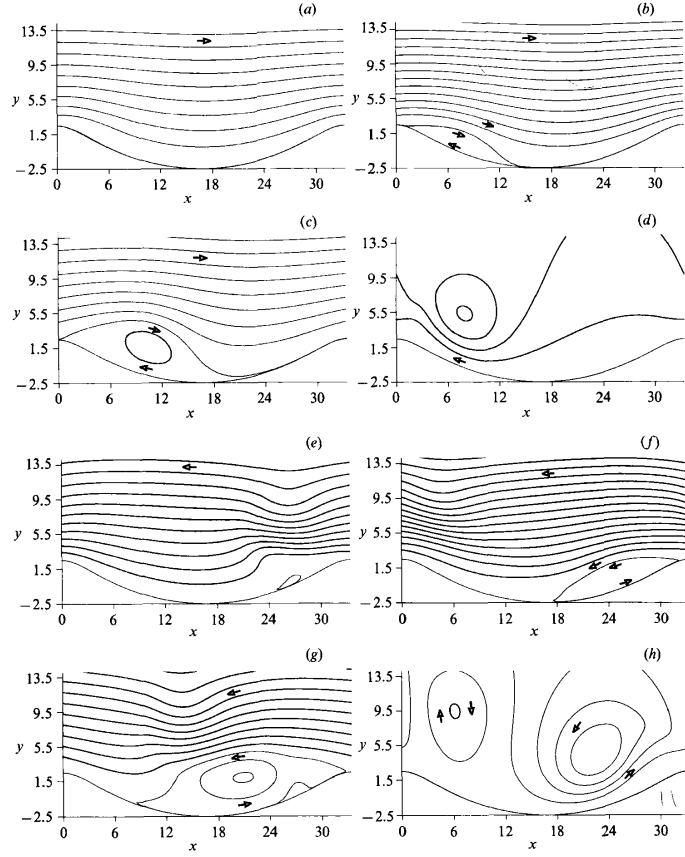


Figure 1.12: Two-dimensional, non-turbulent analytical solution of oscillatory flow over a sinusoidally rippled bed. The streamlines show a vortex form on the downstream side of the ripple, which is shed back in the free flow when the flow reverses directions. Blondeaux and Vittori (1991).

Spalart and Baldwin (1989) conducted DNS of an oscillating turbulent boundary layer over a limited range of Reynolds numbers. Akhavan et al. (1991) investigated the transition to turbulence in oscillatory Stokes flows using DNS, and identified four flow regimes. The regimes are laminar, disturbed laminar (during acceleration), intermittently turbulent (during deceleration), and fully turbulent. Di Liberto and Ciofalo (2009) ran DNS of oscillatory flow in a plane channel, and were able to confirm the four flow regimes iden-

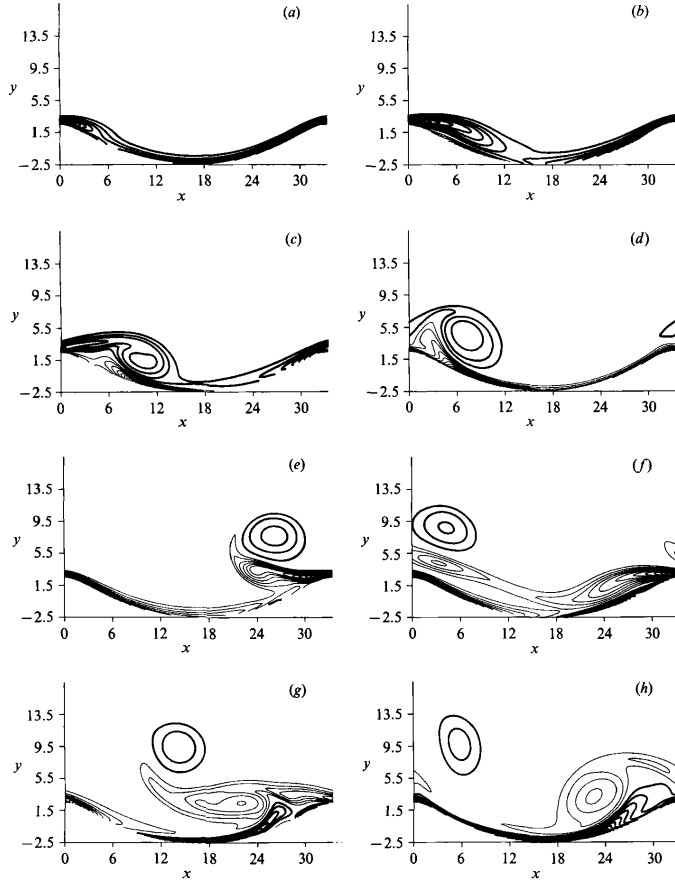


Figure 1.13: Two-dimensional, non-turbulent analytical solution of oscillatory flow over a sinusoidally rippled bed. The vorticity shows a vortex form on the downstream side of the ripple, which collides and pairs with a second vortex when the flow reverses directions, and then both are shed back to the free flow. Blondeaux and Vittori (1991).

tified by Akhavan et al. (1991). Vittori and Verzicco (1998) performed numerical simulations of oscillatory flow over a wavy wall, confirming that imperfections of the boundary are fundamental to the production of disturbances associated with turbulence. Yakhot et al. (1999) conducted numerical simulations of laminar oscillatory flow in a square duct. Different flow regimes were characterized as a function of Reynolds number. The authors note that the induced velocity experiences a phase lag relative to the pressure oscillations, which can vary from zero to $\pi/2$ for slow and fast oscillations, respectively. Ding and Zhang (2011) performed a 3D Lattice Boltzmann simulation of oscillatory flow over a rough bed composed of fixed particles in two packing configurations, to confirm the phase lead of skin friction velocity over the free stream velocity. Kirca

et al. (2016) use a RANS solver combined with a random-walk particle model to track individual particles released periodically from the same position in an oscillating open channel flow.

Hsu et al. (2000) studied oscillatory flow over flat plates using both RANS and LES techniques, focusing on the transition from laminar to turbulent regimes as a function of Reynolds number. Scotti and Piomelli (2001) conducted DNS and LES of an oscillating turbulent channel. In comparing to the DNS and experimental data, the validity of the LES for this flow configuration is demonstrated.

Fornarelli and Vittori (2009) use DNS and an immersed boundary technique to simulate oscillatory flow over a rough wall, composed of fixed spherical particles. In a similar manner to Fornarelli and Vittori (2009), Ghodke and Apte (2016) examine the effects of wall roughness on an oscillatory flow using a DNS and immersed boundary method to model the wall roughness with fully resolved fixed particles. The highly resolved simulations show that the velocity and pressure fluctuations are non-Gaussian in their distribution. Mazzuoli et al. (2016) perform fully resolved DNS-IB simulations of particle chain formation under an oscillatory flow, as shown in Figure 1.14. The simulations are performed on a smooth wall and a rough wall, composed of fixed particles. Even when the particles are initially aligned in chains in the streamwise direction, the oscillating flow causes the particles to realign into chains in the spanwise direction.

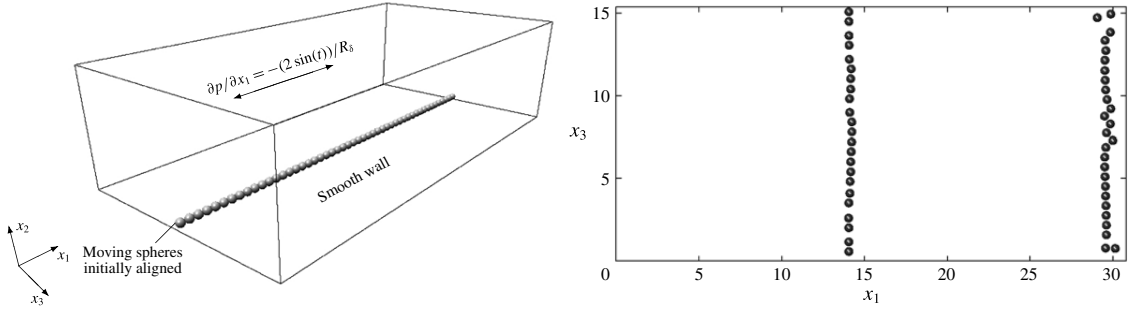


Figure 1.14: Fully resolved DNS-IB simulation of oscillatory flow of particle chains, initially oriented in the streamwise direction. As the flow develops, the chains are reoriented to align in the spanwise direction. Mazzuoli et al. (2016).

1.3 Motivation

Due to limitations in both experimental data collection and fully resolved DNS-IB numerical simulations, the work presented here is designed to capture the mesoscale features of both the fluid and solid phases, while

maintaining computational feasibility. In the LES used in this work, the fluid is resolved at the largest scales and modeled only at the smallest scales. This approach is paired with a DPM in which particles are individually modeled by volume-averaging the governing equations of the flow, and particle-particle interactions are controlled by a soft-sphere collision model and simple adhesion model. In general, this approach has shown good fidelity to experimental mixed-phase flows. And, specifically, this code has demonstrated it's applicability to unidirectional ripple formation in pipe flow. As will be shown in the following sections, application of the LES-DPM approach to the flow configuration in this work shows good agreement with experimental results and illuminates some previously unobserved phenomena.

Chapter 2

Methodology & Results

2.1 Governing Equations & Numerical Methodology

The gas/fluid phase is governed by the Low Mach Approximation incompressible Navier-Stokes equations, and the solid phase particles are described by the Discrete Particle Model (DPM), or Lagrangian Particle Tracking (LPT) method, as described by Capelat and Desjardins (2013b) and Pepiot and Desjardins (2012). These equations are implemented in an arbitrarily high-order, massively parallel numerical code capable of direct numerical simulations (DNS), described by Desjardins et al. (2008). However, in this work, a Large Eddy Simulation (LES) was conducted. Using the same methodology as Arolla and Desjardins (2015), the large scales of the flow are resolved, but the smaller scales are modeled at the sub-grid scale (SGS).

This code is staggered in both space and time, and, in this work, spatial and temporal integrations are second-order accurate. The scheme conserves mass, momentum, and energy. Time advancement is done using a fractional step Crank-Nicolson scheme. A second-order Runge-Kutta scheme is employed to solve for the position, velocity, and angular velocity of each particle. The coupling between the fluid and solid phases is achieved through the volume fraction and interphase forcing terms, which is discussed in the following sections. For the full details, the reader is referred to Desjardins et al. (2008) and Pepiot and Desjardins (2012). The following serves as an overview of their methodology found in Arolla and Desjardins (2015),

in which this methodology was shown to satisfactorily predict ripple formations under directional pipe flow, and as shown in the previous Chapter in Figure 1.8.

2.1.1 Gas/Fluid Phase

Taking into account the volume occupied by the particles, the continuity equation is

$$\frac{\partial}{\partial t} (\psi_f \rho_f) + \nabla \cdot (\psi_f \rho_f \mathbf{u}_f) = 0, \quad (2.1)$$

where ψ_f is the volume fraction of the fluid, ρ_f is the density of the fluid, and \mathbf{u}_f is the velocity of the fluid. With the addition of a source term for the exchange of momentum with the solid phase, \mathbf{F}_{inter} , the conservation of momentum equation becomes

$$\frac{\partial}{\partial t} (\psi_f \rho_f \mathbf{u}_f) + \nabla \cdot (\psi_f \rho_f \mathbf{u}_f \mathbf{u}_f) = \nabla \cdot (\boldsymbol{\tau} - \mathbf{R}) + \mathbf{F}_{pgrad} + \mathbf{F}_{gravity} - \mathbf{F}_{inter}. \quad (2.2)$$

$\mathbf{F}_{pgrad} = \mathbf{p}_{x,0} \cos(\omega t)$ is the oscillating pressure gradient driving the flow. The gravity force is $\mathbf{F}_{gravity} = \psi_f \rho_f \mathbf{g}$. \mathbf{R} is the unresolved sub-grid stress that results from spatially filtering the velocity field, and $\boldsymbol{\tau}$ is the stress tensor

$$\boldsymbol{\tau} = -p \mathbf{I} + \boldsymbol{\sigma} + \mathbf{R}. \quad (2.3)$$

The pressure is denoted by p and the viscous stress tensor, $\boldsymbol{\sigma}$ is defined as

$$\boldsymbol{\sigma} = \mu (\nabla \mathbf{u}_f + \nabla \mathbf{u}_f^T) - \frac{2}{3} \mu \nabla \cdot \mathbf{u}_f \mathbf{I}, \quad (2.4)$$

where μ is the dynamic viscosity.

The isotropic part of \mathbf{R} is absorbed into pressure, and the anisotropic part of \mathbf{R} is

$$\mathbf{R} - \frac{1}{3} trace(\mathbf{R}) \simeq \mu_t (\nabla \mathbf{u}_f + \nabla \mathbf{u}_f^T). \quad (2.5)$$

The turbulent viscosity, μ_t , is dynamically calculated by a Smagorinsky model (1963) (1991) (1992) in conjunction with the Lagrangian averaging of Meneveau (1996). Since the flow is complex, Meneveau's method follows a parcel of fluid in a Lagrangian framework and uses its history to determine the μ_t .

2.1.2 Low-Pass Filtering

Large Eddy Simulations (LES) solve a set of low-pass spatially-filtered Navier-Stokes equations. A generic function f can be broken down into the low-pass filtered component, \bar{f} , and the unfiltered component, f' :

$$f = \bar{f} + f'. \quad (2.6)$$

Consider the use of Fourier transforms to decompose any function f into the sum of sinusoidal frequencies that make it up. Lower frequencies represent larger scale information and higher frequencies represent smaller scale information. In this case, a low-pass filter retains the low wave number components (lower frequency, or larger scale information) of f and cuts off the high wave number components (higher frequency, or smaller scale information).

In the work presented here, the grid itself is the low-pass filter, otherwise known as a grid-filter. As a comparison, the grid for a properly set up Direct Numerical Simulation (DNS) must be resolved, or small enough, to capture even the smallest scales of the flow. In this paper, a coarser grid is used, which does not resolve all the smallest scales of the flow. Therefore, this coarser grid is only resolving the larger scale information of what would have been the DNS, and essentially filtering out the smaller scale information. In this way, the coarser grid of the LES results in a grid-filtered version of the true velocity field. At the center of the domain, away from the rippled bed, this coarser grid is sufficient to resolve all scales of the flow. But at the interface of the rippled bed, the grid is not able to resolve the smallest scale interactions. This, at the sub-grid scale (SGS), is where the LES model's effects will be seen. As shown in Figure 1.5, a sufficiently resolved LES grid can capture the mesoscale features of the flow and provide an accurate description of the physics, while reducing computational cost.

2.1.3 Filtered Incompressible Navier-Stokes Equations

The incompressible Navier-Stokes equations are made up of the continuity equation and the conservation of momentum equation, respectively,

$$\frac{\partial u_i}{\partial x_i} = 0 \quad (2.7)$$

$$\frac{\partial u_i}{\partial t} + \frac{\partial u_i u_j}{\partial x_i} = -\frac{1}{\rho} \frac{\partial p}{\partial x_i} + \nu \frac{\partial^2 u_i}{\partial x_i \partial x_i}. \quad (2.8)$$

Since filtering and differentiation commute, filtering the continuity equation yields

$$\overline{\frac{\partial u_i}{\partial x_i}} = \overline{\frac{\partial \bar{u}_i}{\partial x_i}} = 0, \quad (2.9)$$

Where the overbar ($\bar{\cdot}$) denotes a filtered variable. The filtered momentum equation becomes

$$\overline{\frac{\partial u_i}{\partial t}} + \overline{\frac{\partial u_i u_j}{\partial x_i}} = -\overline{\frac{1}{\rho} \frac{\partial p}{\partial x_i}} + \overline{\nu \frac{\partial^2 u_i}{\partial x_i \partial x_i}}. \quad (2.10)$$

Again, since filtering and differentiation commute,

$$\overline{\frac{\partial \bar{u}_i}{\partial t}} + \overline{\frac{\partial \bar{u}_i \bar{u}_j}{\partial x_i}} = -\overline{\frac{1}{\rho} \frac{\partial \bar{p}}{\partial x_i}} + \overline{\nu \frac{\partial^2 \bar{u}_i}{\partial x_i \partial x_i}}. \quad (2.11)$$

However, since the actual unfiltered velocity field is not known, the non-linear advective term, $\frac{\partial \bar{u}_i \bar{u}_j}{\partial x_i}$, can not be calculated. However, $\frac{\partial \bar{u}_i \bar{u}_j}{\partial x_i}$, can be calculated, so it is added to both sides of the equation, and the equation is reorganized:

$$\overline{\frac{\partial \bar{u}_i}{\partial t}} + \overline{\frac{\partial \bar{u}_i \bar{u}_j}{\partial x_i}} = -\overline{\frac{1}{\rho} \frac{\partial \bar{p}}{\partial x_i}} + \overline{\nu \frac{\partial^2 \bar{u}_i}{\partial x_i \partial x_i}} - \left(\overline{\frac{\partial \bar{u}_i \bar{u}_j}{\partial x_i}} - \frac{\partial \bar{u}_i \bar{u}_j}{\partial x_i} \right). \quad (2.12)$$

Assigning $\tau_{ij} = \bar{u}_i \bar{u}_j - \bar{u}_i \bar{u}_j$, the LES filtered momentum equation is written

$$\overline{\frac{\partial \bar{u}_i}{\partial t}} + \overline{\frac{\partial \bar{u}_i \bar{u}_j}{\partial x_i}} = -\overline{\frac{1}{\rho} \frac{\partial \bar{p}}{\partial x_i}} + \overline{\nu \frac{\partial^2 \bar{u}_i}{\partial x_i \partial x_i}} - \frac{\partial \tau_{ij}}{\partial x_i}. \quad (2.13)$$

2.1.4 Smagorinsky Model

In the Smagorinsky model (1963), the unresolved stress, τ_{ij} , is modeled with an eddy viscosity, ν_t , whose only purpose is to dissipate energy at a *rate* that is physically correct.

$$\tau_{ij} = \bar{u}_i \bar{u}_j - \bar{u}_i \bar{u}_j = 2\nu_t \bar{S}_{ij}, \quad (2.14)$$

where, $\bar{S}_{ij} = \frac{1}{2} \left(\frac{\partial \bar{u}_i}{\partial x_j} + \frac{\partial \bar{u}_j}{\partial x_i} \right)$ is the rate of strain tensor of the grid-filtered velocity field. The eddy viscosity is defined as

$$\nu_t = C \Delta^2 |\bar{S}|, \quad (2.15)$$

where,

$$|\bar{S}| = \sqrt{2\bar{S}_{ij}\bar{S}_{ij}}. \quad (2.16)$$

So, the unresolved stress becomes

$$\tau_{ij} = 2C \alpha_{ij}, \quad (2.17)$$

and,

$$\alpha_{ij} = \Delta^2 |\bar{S}| \bar{S}_{ij}. \quad (2.18)$$

Where Δ is the grid size. At this point, the Smagorinsky constant C is just that - a constant. This constant can be tuned and adjusted in an ad hoc fashion for different flow configurations. However, as will be shown in the next section, this “constant” can be dynamically modeled to self-adjust.

2.1.5 Germano's Dynamic Smagorinsky Model

The crux of dynamically modeling the Smagorinsky constant is the Germano Identity (1991), which states that the SGS model's contribution to the conservation of momentum equation must be the same as that of the resolved turbulent stress tensor within a band filter.

To explain the Germano identity, start with the term that cannot be resolved using the grid-filtered velocity field, the non-linear advective term, $f(u) = u_i u_j$. The grid-filtered term is then equal to the sum of filtered and modeled components

$$\overline{f(u)} = f(\bar{u}) + m(\bar{u}). \quad (2.19)$$

Where $f(\bar{u}) = \bar{u}_i \bar{u}_j$, and, per Equation 2.17, $m(\bar{u}) = \tau_{ij} = 2C\alpha_{ij}$ is the SGS model at the grid-filter scale.

Now, a new filter is introduced. The test filter, denoted by $\hat{\cdot}$, is a filter larger than the grid filter, usually by a factor of 2 (the test filter $\hat{\Delta} \simeq 2\Delta$). The goal is to gain an understanding of how the functions f and m vary with the size of the filter. So, if we now reconsider Equation 2.19, but for a grid-filtered, then test-filtered, velocity field, we have

$$\widehat{f(u)} = f(\hat{u}) + m(\hat{u}). \quad (2.20)$$

If Equation 2.19 is test-filtered and Equation 2.20 is subtracted from it, the result is

$$\widehat{f(\bar{u})} - f(\hat{u}) = m(\hat{u}) - \widehat{m(\bar{u})}. \quad (2.21)$$

This equation represents the band-pass filtered information of the resolved field, on the left hand side, and the band-pass filtered information of SGS model on the right hand side. The band-pass filter has clipped all information smaller than the grid-filter and larger than test-filter, leaving just a *band* of information.

The $m(\hat{u})$ term is addressed in a similar way to $m(\bar{u}) = \tau_{ij} = 2C\alpha_{ij}$, in Equation 2.17. The test-filtered versions are:

$$T_{ij} = 2C\beta_{ij}, \quad (2.22)$$

and,

$$\beta_{ij} = \hat{\Delta}^2 |\hat{S}| \hat{S}_{ij}. \quad (2.23)$$

So, $m(\hat{u}) = T_{ij} = 2C\beta_{ij}$. Equation 2.21 becomes

$$\widehat{\bar{u}_i \bar{u}_j} - \hat{u}_i \hat{u}_j = T_{ij} - \widehat{\tau_{ij}}, \quad (2.24)$$

or, replacing the resolved stress on the left hand side with $L_{ij} = -(\widehat{\bar{u}_i \bar{u}_j} - \hat{u}_i \hat{u}_j)$,

$$-L_{ij} = T_{ij} - \widehat{\tau_{ij}}, \quad (2.25)$$

Equations 2.24 and 2.25 are both versions of the Germano Identity.

Plugging Equations 2.17 and 2.22 into the Germano Identity results in

$$-L_{ij} = 2C\beta_{ij} - \widehat{2C\alpha_{ij}}. \quad (2.26)$$

Although it has been shown that C can vary greatly in a small area and should not be factored out from the filter in the second term on the right hand side (since it is not constant), we do so here anyway, with the understanding that the issue will be addressed in the next section by averaging in time. So, Equation 2.26 becomes,

$$-L_{ij} = 2C\beta_{ij} - \widehat{2C\alpha_{ij}} = 2C(\beta_{ij} - \widehat{\alpha_{ij}}). \quad (2.27)$$

Recalling, the definitions of α_{ij} and β_{ij} ,

$$-L_{ij} = 2C(\hat{\Delta}^2 |\hat{S}| \hat{S}_{ij} - \widehat{\Delta^2 |\bar{S}| \bar{S}_{ij}}) = 2C\Delta^2 \left[\left(\frac{\hat{\Delta}}{\Delta} \right)^2 |\hat{S}| \hat{S}_{ij} - \widehat{|\bar{S}| \bar{S}_{ij}} \right], \quad (2.28)$$

$$L_{ij} = 2C\Delta^2 \left[\widehat{|\bar{S}| \bar{S}_{ij}} - \left(\frac{\hat{\Delta}}{\Delta} \right)^2 |\hat{S}| \hat{S}_{ij} \right], \quad (2.29)$$

$$L_{ij} = 2C\Delta^2 M_{ij}, \quad (2.30)$$

where $M_{ij} = \widehat{|\bar{S}|S_{ij}} - \left(\frac{\hat{\Delta}}{\Delta}\right)^2 \widehat{|\bar{S}|S_{ij}}$.

The Germano Identity requires that the left hand side and right hand side are equal. But since this is only statistically true due to the nature of modeling SGS information, the difference between the two must be minimized in order to determine the optimal value of $C\Delta^2$. So, per the work of Lilly (1992), the difference, or error, is defined as

$$e_{ij} = L_{ij} - 2C\Delta^2 M_{ij}. \quad (2.31)$$

The least-square error method requires that $\frac{dE^2}{dC} = 0$, where

$$E^2 = e_{ij}e_{ij} = (L_{ij} - 2C\Delta^2 M_{ij})^2 = L_{ij}L_{ij} - 4C\Delta^2 L_{ij}M_{ij} + 4C^2\Delta^4 M_{ij}M_{ij}. \quad (2.32)$$

Taking the derivative with respect to C ,

$$\frac{d}{dC}(E^2) = 0 = 0 - 4\Delta^2 L_{ij}M_{ij} + 8C\Delta^4 M_{ij}M_{ij}. \quad (2.33)$$

Or,

$$C\Delta^2 = \frac{1}{2} \frac{L_{ij}M_{ij}}{M_{ij}M_{ij}}. \quad (2.34)$$

Because the numerator can be negative, and $C\Delta^2$ tends to have large variations in small regions of the flow (which indicates that removing C from the test-filter in Equation 2.27 was unwarranted), some form of averaging is required to address this numerical instability. If there are any homogeneous directions in the flow (i.e. the spanwise direction in a channel flow), the numerator and denominator are averaged over those homogeneous directions. Thus,

$$C\Delta^2 = \frac{1}{2} \frac{\langle L_{ij}M_{ij} \rangle}{\langle M_{ij}M_{ij} \rangle}, \quad (2.35)$$

where, $\langle \cdot \rangle$ is a averaging operator over all points in the homogeneous direction(s). However, in more complex flow where there are no homogeneous directions, a different approach must be taken.

2.1.6 Lagrangian Averaging

Meneveau et al. (1996) proposed an approach for non-homogeneous flows where by the terms in Equation 2.35 are averaged not in space, but in time. Spatial averaging requires either a homogeneous direction, or well-chosen local volume averages to address the numerical instability of Equation 2.35. In complex flows, this is not possible. Meneveau's proposal is to "follow" a parcel of fluid in a Lagrangian framework through time and use its history to inform the current value of $C\Delta^2$.

First, for an arbitrary function f , Lagrangian averaging is defined as follows,

$$\langle f \rangle \simeq \mathcal{I}_f = \int_{-\infty}^t f(t') W(t - t') dt', \quad (2.36)$$

where $W(t)$ is an exponential weighting function meant to give greater influence to current information. This integral is carried out over previous positions of the fluid parcel in question, up to the parcel's current position - in other words, the parcel's path line. So, Equation 2.35 then becomes

$$C\Delta^2 = \frac{1}{2} \frac{\langle L_{ij}M_{ij} \rangle}{\langle M_{ij}M_{ij} \rangle} = \frac{1}{2} \frac{\mathcal{I}_{LM}^n}{\mathcal{I}_{MM}^n}. \quad (2.37)$$

Where the Lagrangian average of the LM and MM terms are, respectively,

$$\mathcal{I}_{LM} = \int_{-\infty}^t L_{ij}(t') M_{ij}(t') W(t - t') dt', \quad (2.38)$$

$$\mathcal{I}_{MM} = \int_{-\infty}^t M_{ij}(t') M_{ij}(t') W(t - t') dt'. \quad (2.39)$$

To allow for a simple approximation of these integrals, the weighting function must be cleverly chosen,

$$W(t) = \frac{1}{T} e^{-\frac{t}{T}}, \quad (2.40)$$

where the time constant is defined as

$$T = 1.5\Delta(\mathcal{I}_{LM}^n \mathcal{I}_{MM}^n)^{-\frac{1}{8}}. \quad (2.41)$$

The above integrals can then be discretized and approximated as

$$\mathcal{I}_{LM}^n(\mathbf{x}) = H\{\varepsilon L_{ij}^n(\mathbf{x})M_{ij}^n(\mathbf{x}) + (1 - \varepsilon)\mathcal{I}_{LM}^{n-1}(\mathbf{x} - \mathbf{u}^n\Delta t)\}, \quad (2.42)$$

$$\mathcal{I}_{MM}^n(\mathbf{x}) = \varepsilon M_{ij}^n(\mathbf{x})M_{ij}^n(\mathbf{x}) + (1 - \varepsilon)\mathcal{I}_{MM}^{n-1}(\mathbf{x} - \mathbf{u}^n\Delta t), \quad (2.43)$$

where the values of \mathcal{I}_{LM}^{n-1} and \mathcal{I}_{MM}^{n-1} , at the location $(\mathbf{x} - \mathbf{u}^n\Delta t)$ and timestep $n - 1$, are calculated using linear interpolation. And, for a timestep Δt ,

$$\varepsilon = \frac{\Delta t/T}{1 + \Delta t/T}. \quad (2.44)$$

The ramp function is designed so as to eliminate negative values of $\mathcal{I}_{LM}^n(\mathbf{x})$,

$$H\{x\} = \begin{cases} x & \text{if } x \geq 0, \\ 0 & \text{if } x < 0. \end{cases} \quad (2.45)$$

Then, $C\Delta^2$ can be calculated in Equation 2.37 by using the discretized integrals of Equations 2.43. And finally, the eddy viscosity, ν_t , can be determined in Equation 2.15 in order to calculate the unresolved stress, τ_{ij} , of Equation 2.14 and close the LES momentum Equation 2.13.

2.1.7 Solid Phase

The location of an individual particle is defined by

$$\frac{d\mathbf{x}_p}{dt} = \mathbf{u}_p. \quad (2.46)$$

According to Newton's second law of motion, particles are governed by

$$m_p \frac{d}{dt}(\mathbf{u}_p) = \mathbf{f}_{inter} + \mathbf{F}_{col} + \mathbf{F}_{adh} + m_p\mathbf{g}, \quad (2.47)$$

where m_p is the mass of the particle, \mathbf{u}_p is the velocity of the particle, \mathbf{f}_{inter} is the exchange of momentum with the fluid for the single particle, \mathbf{F}_{col} is the force imparted by collisions with other particles or a wall,

and \mathbf{F}_{adh} is the adhesion force between appropriately close particles. Since the particles are assumed to be perfect spheres, the particle mass is a function of particle density, ρ_p , and particle diameter, d ,

$$m_p = \frac{\rho_p \pi d^3}{6}. \quad (2.48)$$

For a given cell volume, the sum of all of the single particle momentum exchanges, \mathbf{f}_{inter} , gives the full momentum exchange term in Equation 2.2

$$\mathbf{F}_{inter} = \sum_i^{N_p} \mathbf{f}_{inter}^i. \quad (2.49)$$

The collision term, \mathbf{F}_{col} , represents the sum of the all collision forces acting on a given particle. This term will be discussed in further detail in Section 2.1.9.

The angular momentum of a particle, ω_p , is assumed to be generated by collisions, and is described by

$$I_p \frac{d\omega_p}{dt} = \sum_j \frac{d}{2} \mathbf{n} \times \mathbf{f}_{col}^{t,a \rightarrow b}, \quad (2.50)$$

where I_p is the moment of inertia ($I_p = \frac{m_p d_p^2}{10}$ for a sphere), and $\mathbf{f}_{col}^{t,a \rightarrow b}$ is the tangential component of the collision force generated by the collision of particle a with particle b .

2.1.8 Momentum exchange

The momentum exchange between the fluid and a single particle occurs at the surface, S_p , of the particle. Therefore, the interaction force can be calculated by taking the integral of the stress tensor over the surface of the particle. The stress tensor at a specific point is denoted $\boldsymbol{\tau}'$, and the momentum exchange term is written as

$$\mathbf{f}_{inter} = \oint_{S_p} \boldsymbol{\tau}' \cdot \mathbf{n} dS \quad (2.51)$$

where \mathbf{n} is unit vector normal to particle surface S_p . Since $\boldsymbol{\tau}'$ is not known, but the averaged $\boldsymbol{\tau}$ for the cell volume, V , is known, it is assumed that $\boldsymbol{\tau}' = \boldsymbol{\tau} + \mathbf{f}_{drag}$. The drag force, \mathbf{f}_{drag} , represents the difference between the average stress tensor value and the value at a specific point. \mathbf{f}_{drag} represents the effect of the

particle on the fluid in V .

$$\mathbf{f}_{inter} = \oint_{S_p} \tau \cdot \mathbf{n} dS + \mathbf{f}_{drag} \quad (2.52)$$

Applying the Gauss theorem,

$$\mathbf{f}_{inter} = \int_{V_p} \nabla \cdot \boldsymbol{\tau} dV + \mathbf{f}_{drag} \quad (2.53)$$

The final assumption is that locally averaged stress tensor value will not vary significantly over the scale of a particle diameter, therefore, $\int_{V_p} \nabla \cdot \boldsymbol{\tau} dV \rightarrow V_p \nabla \cdot \boldsymbol{\tau}$. Thus,

$$\mathbf{f}_{inter} = V_p \nabla \cdot \boldsymbol{\tau} + \mathbf{f}_{drag} \quad (2.54)$$

The drag force is formulated as follows

$$\mathbf{f}_{drag} = \frac{18m_p\mu\psi_f}{\rho_p d_p^2} (\mathbf{u}_f - \mathbf{u}_p) F(\psi_f, Re_p) \quad (2.55)$$

Where the function F is that of Tenneti et al. (2011) formulation for a dimensionless drag coefficient, which relies solely on the volume fraction of the fluid and the Reynolds number of the particle, $Re_p = \frac{\rho_f d_p |\mathbf{u}_f - \mathbf{u}_p|}{\mu}$:

$$F(\psi_f, Re_p) = \frac{1 + 0.15Re_p^{0.687}}{\psi_f^2} + \psi_f F_1(\psi_f) + \psi_f F_2(\psi_f, Re_p). \quad (2.56)$$

Where the drag on a single particle, of Schiller and Naumann (1933), is the numerator in the first term.

$$F_1(\psi_f) = \frac{5.81(1 - \psi_f)}{\psi_f^3} + \frac{0.48(1 - \psi_f)^3}{\psi_f^2}, \quad (2.57)$$

and

$$F_2(\psi_f, Re_p) = (1 - \psi_f)^3 Re_p (0.95 + \frac{0.61(1 - \psi_f)^3}{\psi_f^2}). \quad (2.58)$$

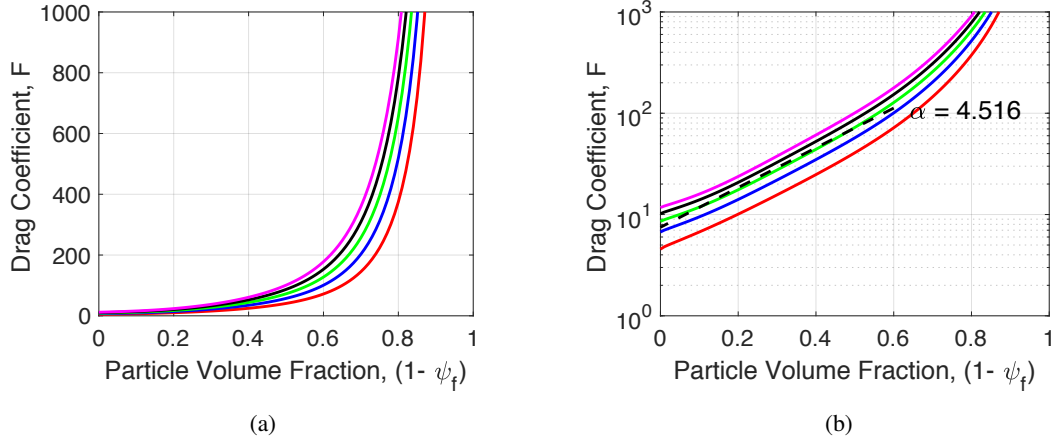


Figure 2.1: (a) Tenneti's drag coefficient for a range of Re_p . (b) Semilog plot of the drag coefficient. $Re_p = 100$ (red), $Re_p = 200$ (blue), $Re_p = 300$ (green), $Re_p = 400$ (black), $Re_p = 500$ (magenta), and power law fit of $Re_p = 100$ (dashed black). In this work, $Re_{p,max} \simeq 300$, and $\psi_p \leq 0.7$. For these conditions, the relationship between the ψ_p and F follows a power law fit, with $\alpha = 4.516$.

Therefore, in the limit of $\psi_f \rightarrow 1$, Equation 2.56 reduces to

$$F(1, Re_p) = 1 + 0.15 Re_p^{0.687}, \quad (2.59)$$

Which is the drag on an isolated particle as described by Schiller and Naumann (1933). Although Stokes Law would indicate a value of $F(1, Re_p) = \frac{C_d Re_p}{24}$, Equation 2.59 compares favorably to other well-known and accepted drag force correlations. The dimensionless drag force coefficient is shown in figure 2.1. This formulation is valid for $Re_p < 1000$. The asymptotic limit of the maximum Re_p in this work is roughly 300.

2.1.9 Collision Model

The soft-sphere model of Cundall and Strack (1979) is used to determine the particle-particle collision forces. The normal component of a collision is described by a spring-dashpot model. For any two particles a and b , d_{ab} is the distance between the centers, and r_i is the radius of any particle i . A collision spring force is generated if $d_{ab} < (r_a + r_b + \lambda_{col})$, otherwise, the collision force is zero, as shown in Figure 2.2. The λ_{col} buffer region increases the stability of the algorithm because particle overlap is not required for collision. Therefore, on average, colliding particles do not overlap. Thus the normal component of collision force

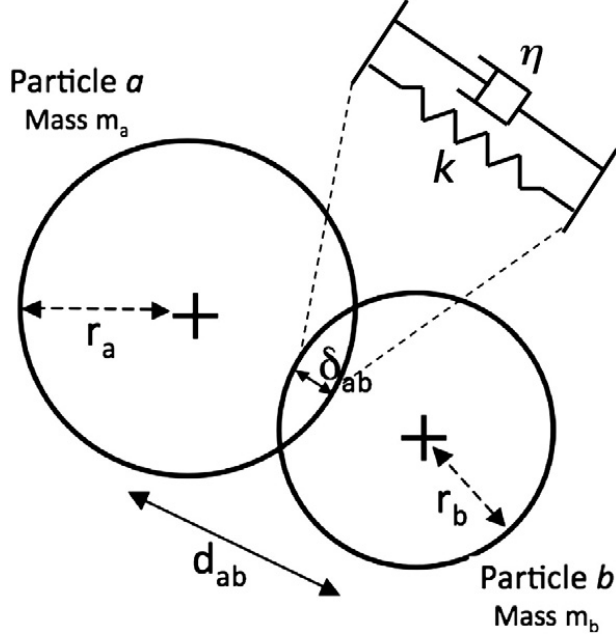


Figure 2.2: Soft-sphere model collision between two different sized particles. Once the particles overlap an amount δ , or are within the buffer region λ_{col} of each other, a spring force is generated between them.

generated by particle a acting on particle b is

$$\mathbf{f}_{col}^{n,a \rightarrow b} = k\delta\mathbf{n}_{ab} - \eta\mathbf{u}_{n,ab}, \quad (2.60)$$

where k is the spring constant, η is the dashpot damping coefficient, δ is the particle overlap, \mathbf{n}_{ab} is the unit normal vector between the centers of particles a and b , and $\mathbf{u}_{n,ab}$ is the normal relative velocity between particles a and b defined as

$$\mathbf{u}_{n,ab} = ((\mathbf{u}_a - \mathbf{u}_b) \cdot \mathbf{n}_{ab})\mathbf{n}_{ab}. \quad (2.61)$$

The damping coefficient is written

$$\eta = -2\ln e \frac{\sqrt{m_{ab}k}}{\sqrt{\pi^2 + (\ln e)^2}}, \quad \text{with} \quad m_{ab} = \frac{m_a m_b}{m_a + m_b}, \quad (2.62)$$

where the restitution coefficient is $0 < e < 1$ and the mass of any particle i is m_i .

As a result of inter-particle friction, particles can obtain angular velocities due to tangential collisions. The tangential force generated when particle a acts on particle b is

$$\mathbf{f}_{col}^{t,a \rightarrow b} = \begin{cases} -k_t \delta_t - \eta_t \mathbf{u}_{t,ab}, & \text{if } |\mathbf{f}_{col}^{t,a \rightarrow b}| \leq \mu_f |\mathbf{f}_{col}^{n,a \rightarrow b}| \\ -\mu_f |\mathbf{f}_{col}^{n,a \rightarrow b}| \mathbf{t}_{ab}, & \text{if } |\mathbf{f}_{col}^{t,a \rightarrow b}| > \mu_f |\mathbf{f}_{col}^{n,a \rightarrow b}|, \end{cases} \quad (2.63)$$

where k_t is the tangential spring stiffness, δ_t is the tangential displacement, η_t tangential damping coefficient, μ_f is the friction coefficient, and $\mathbf{u}_{t,ab}$ is the relative tangential velocity defined as

$$\mathbf{u}_{t,ab} = \mathbf{u}_{ab} - \mathbf{u}_{n,ab}. \quad (2.64)$$

The tangential unit vector is then

$$\mathbf{t}_{ab} = \frac{\mathbf{u}_{t,ab}}{|\mathbf{u}_{t,ab}|}, \quad (2.65)$$

and the tangential component of the collision force is defined as

$$\mathbf{f}_{col}^{t,a \rightarrow b} = -\mu_f |\mathbf{f}_{col}^{n,a \rightarrow b}| \mathbf{t}_{ab}. \quad (2.66)$$

The total collision force on a particle i is the sum of the collision forces from all particles j ,

$$\mathbf{F}_{col}^i = \sum_j \left(\mathbf{f}_{col}^{n,i \rightarrow j} + \mathbf{f}_{col}^{t,i \rightarrow j} \right). \quad (2.67)$$

Particle-wall collisions are determined by treating the wall as a particle, with a radius of zero and infinite mass.

2.1.10 Adhesion Model

Usually, numerical simulations that incorporate static particle beds are left to settle under gravity into quasi-random patterns, absent flow, until an equilibrium state is achieved. Since the ripples in the experimental work are found to be steady-state in the shorter time scales that are numerically feasible, the simulation was developed with the bed prescribed a sinusoidal ripple morphology meant to mimic the morphology of

experimental work. In order to maintain the stability of this rippled bed, an adhesive, or attractive, force, equal in magnitude but opposite if direction to the collision force, is defined in a thin shell of width λ_{adh} , per the work of Levine and Polimeno (2007). Since the collision force is activated also in a thin shell, the adhesive force is operated in a thin shell beyond that of the collision force.

$$\mathbf{f}_{adh}^{t,a \rightarrow b} = \begin{cases} -\mathbf{f}_{col}^{t,a \rightarrow b}, & (r_a + r_b + \lambda_{col}) < d_{ab} < (r_a + r_b + \lambda_{col} + \lambda_{adh}) \\ 0, & d_{ab} > (r_a + r_b + \lambda_{col} + \lambda_{adh}). \end{cases} \quad (2.68)$$

2.1.11 Fluid and Solid Coupling

Since the fluid properties are stored on the Eulerian grid and the particles can move anywhere within the Lagrangian framework, properties must be interpolated between the grid and any point occupied by a particle. Fluid properties are mapped to particle positions using a trilinear interpolation scheme. Alternatively, particle properties are mapped to the grid using a conservative mollification approach. The Gaussian mollification kernel function is defined as

$$g_{\mathcal{M}}(r) = \frac{1}{\sigma\sqrt{2\pi}} e^{-\frac{r^2}{2\sigma^2}} \quad (2.69)$$

where r is the distance from the particle location to the Eulerian grid point to which the particle value is being extrapolated, and σ is the kernel width defined as $\sigma = \Delta x / (2\sqrt{2\ln 2})$ so that the effect of a given particle is experienced by the nearest 27 cells. The

The extrapolated interaction force at each surrounding grid point, i , is

$$\mathbf{f}'_{inter,i} = \gamma_i \mathbf{f}_{inter}, \quad (2.70)$$

where γ normalizes the particle force for all applicable grid points to which it is extrapolated, ensuring that the particle force is conserved when it is applied to the Eulerian grid. It is defined by

$$\gamma_i = \frac{\int_{V_i} g_{\mathcal{M}}(r) dr}{\sum_j \int_{V_j} g_{\mathcal{M}}(r) dr}. \quad (2.71)$$

2.1.12 Operating parameters

The DPM places its own set of restraints on the system. In addition to the $CFL_f = \frac{4u_f \Delta t}{\Delta x^2}$ condition associated with the fluid, a CFL_p number is also associated with the particle model, defined as

$$CFL_p = \frac{\Delta t_p |u_p|}{d} \leq 0.1, \quad (2.72)$$

where Δt_p is the particle timestep and u_p is the particle velocity. Alone, this restriction limits the particle overlap to 10% of the particle diameter in order to eliminate large overlaps and the large, unphysical, collision forces that would result.

Although the flow field of the vortex dipole is symmetric and centered on the Eulerian grid, it will be shown that the scour topography does exhibit asymmetrical characteristics. Due to the nature of the DPM, the particles, which make up the bed, are not necessarily centered on the grid. Therefore when the vortex dipole impacts the bed, one vortex may be inflicting the maximum shear stress directly onto a single particle, while the shear stress of the other vortex is spread between two particles. Because of the coupling between the flow and the particles, and the drag force associated with this impact, the overall effect will not be symmetric. And, once the symmetry is lost, the rest of the simulation, and subsequent impacts will not be able to recapture it.

Additionally, since particle-particle interactions of the DPM utilized in this work are based on a spring-dashpot approach, where the collisions, or even slight particle overlaps due to round-off errors, are corrected by a spring force, the “settled” particle bed is not actually static. To minimize this effect, the spring constant k is adjusted for each Shields number (and, thus, particle density) configuration, in order to achieve particle-particle oscillations that are significantly smaller than the forces inflicted by the vortex dipole. The DPM is extremely sensitive to the spring constant parameter. If k is too small, the particles will effectively collapse onto each other. Taking into account the weight of the particles in the bed, the spring constant is thus subject to the following constraint

$$k \gg h_{bed} \frac{m_p g}{d^2} \quad (2.73)$$

where h_{bed} is the height of the particle bed. Alternatively, if k is too large, a static particle bed, under no external forcing, will eventually experience eruptions due to the cumulative effect of the large spring constant. Therefore, a unique spring constant is required for each Shields number (and corresponding particle density). The spring constant is a function of the particle collision time, τ_{col} ,

$$k = \frac{m_{ab}}{\tau_{col}^2} [\pi^2 + \ln^2 e] \quad (2.74)$$

so, each simulation configuration requires a unique τ_{col} value. These values were determined empirically using simulations consisting of a tightly particle bed subject to only a gravitational force. A range of k values are tested and the RMS of the particle velocities are calculated, with the minimum RMS corresponding to the appropriate k value for the tested particle density.

2.2 Simulation Configuration & Methodology

The parameters of the numerical simulation are configured based on the work by Frank and Foster et al. (2015) (2015), which is similar to their other work. The experiment was conducted in the small-oscillatory flow tunnel at the Sediment Dynamics Laboratory of the Naval Research Laboratory, Stennis Space Center, MS, shown in Figure 2.3, per (2014). The square cross-sectioned, water-filled, closed channel is bound on the top and sides by no-slip walls, and the bottom is made up of a sand bed. The average diameter of the sand is 0.7 mm, with an average density of 2635 kg/m^3 . Initially, the sand bed is roughly flat. The fluid is then forced to an oscillatory flow by a sinusoidal piston, with a prescribed period of 2.4 seconds. The maximum freestream velocity, Figure 2.4 achieved by the flow is roughly 0.23 m/s. Eventually, a quasi steady-state condition is reached. At this point, ripples, of a roughly sinusoidal wavelength of 100 mm, and amplitude of roughly 20 mm, have formed in the bed, and their migration and wavelength evolution are on a timescale much larger than the period of oscillation. Data were collected for 11 complete oscillation periods. Using Particle Image Velocimetry (PIV), the three components of the velocity field are measured in a two-dimensional plane parallel to the streamwise and wall-normal directions, centered on a single ripple. In addition, the surface of the ripple is tracked using high speed cameras. So, although the evolution of the ripple is tracked, information about individual grains is not available, and any entrained particles are not resolved.

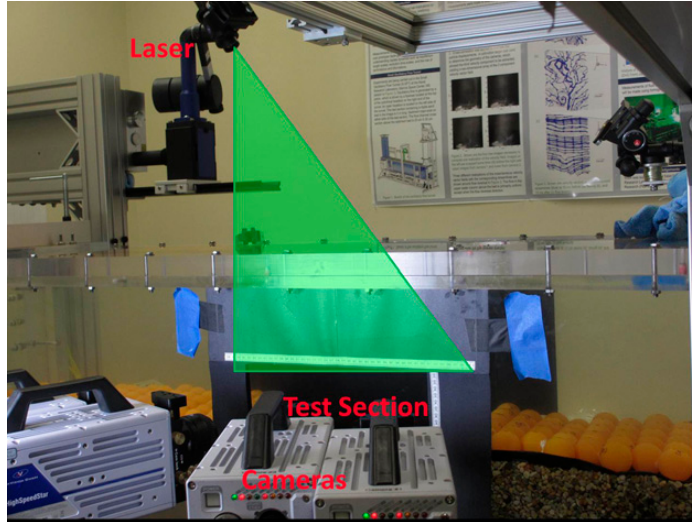


Figure 2.3: Experimental setup in the small-oscillatory flow tunnel at the Naval Research Laboratory. The test section is monitored by the laser and high-speed cameras of the PIV system. Photo courtesy of the Naval Research Laboratory and Frank et al.

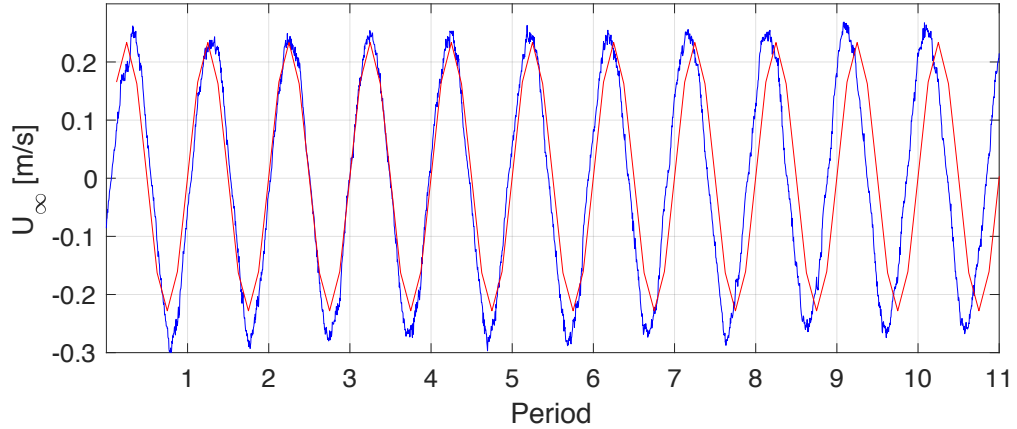


Figure 2.4: Time evolution of the freestream streamwise velocity. The experimental values are denoted by the blue line, the numerical results are represented by the red line. There is some variation in the symmetry and magnitude of the experimental velocity.

In order to mimic the experimental configuration as closely as possible, while maintaining computational feasibility, a Large-Eddy Simulation (LES) approach was chosen so that a courser grid could be utilized. The experimental tunnel is modeled as a channel flow between two parallel plates, which is periodic in both the streamwise and spanwise directions. The half-height of the channel, h , is used to describe the extants of

the domain. As shown in Figure 2.5, the domain measures $6h$, $2h$, and h , in the streamwise, wall-normal, and spanwise directions, respectively. The grid is comprised of 256 by 128 by 64 nodes, in the streamwise, wall-normal, and spanwise directions, respectively. The streamwise and spanwise grids are uniform, and the wall-normal grid is stretched to be refined at the walls and in the rippled particle bed. In wall units, here denoted by a plus sign superscript, the grid is $x^+ = z^+ = 18$ and $y^+ = 10$, where x is the streamwise direction, z is the spanwise direction, and y is wall-normal. Although ideally y^+ should be on the order of a single wall unit, the literature has shown that LES using this larger grid spacing is sufficient to capture the mesoscale features of the flow. This grid configuration allows for particle diameters of 1 mm. The wall at the bottom of the domain has a no-slip boundary condition and is covered in a sinusoidally rippled layer of particles. Gravity, 9.81 m/s^2 , acts in the negative y direction.

Per Hino et. al (1983), the Stokes length Reynolds number, based on the Stokes thickness, is given by

$$Re_s = \frac{U_0 l_s}{\nu}, \quad (2.75)$$

where U_0 is the oscillating mean velocity component and the Stokes thickness is given by $l_s = \sqrt{\frac{2\nu}{\omega}}$. For smooth walls, Hino et. al found that the flow was stable and laminar for $Re_s < 400$, transitioning to turbulence for $400 < Re_s < 800$, and fully turbulent for $Re_s > 800$. In this work, $Re_s = 200$, which would put it squarely in the laminar regime. However, the interaction of the flow with the rippled morphology of the mobile particle bed generates coherent turbulent structures in the flow.

It should be noted that the numerical code used in this work has been shown to replicate ripple formation in unidirectional pipe flow, per Arolla and Desjardins (2015). However, since the timescale required to form the ripples in the experiment presented here is beyond current computational capability, the particle bed is prescribed an initial sinusoidal ripple shape with a wavelength and amplitude matching the experimental configuration. The result is 1,540,800 total particles, which are packed in body centered cubic (BCC) configuration, as shown in Figure 2.6. In order to maintain a similar Shields parameter, $\Theta = \frac{\tau_{bed}}{(\rho_p - \rho_f)gd_p}$, the particle diameter, d_p is 1 mm and the particle density, ρ_p , is 2500 kg/m^3 . The Shields parameter is a dimensionless number reflecting the relative effects of the erosive forces (shear stress) to the restorative forces (gravity). A high Shields parameter reflects highly erosive flow conditions, whereas a low value indicates a stable condition for the bed.

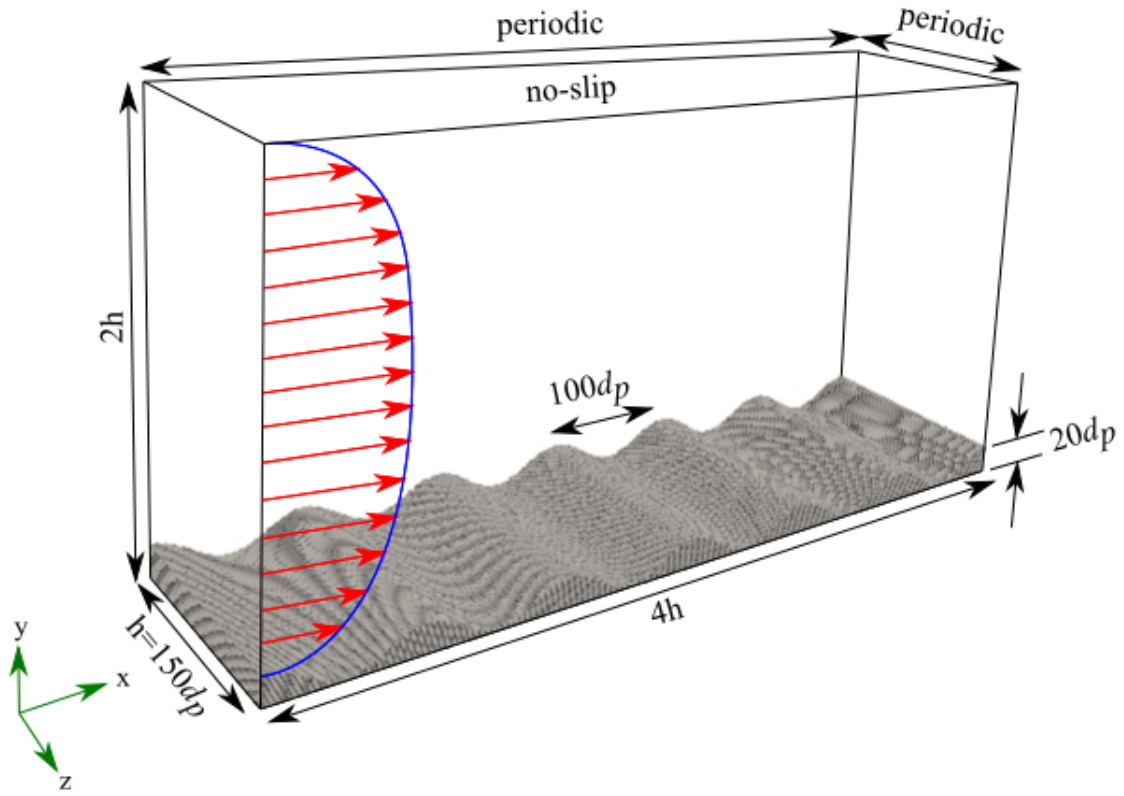


Figure 2.5: Initial configuration of the simulation. The flow is driven by a sinusoidal pressure gradient in the streamwise direction. The morphology of the particle bed is initially sinusoidal.

Despite the tightly packed spacing of the particle bed, the spring-dashpot particle model will force the bed to compress under the effect of gravity. In order to make sure that this process is isolated from any erosive behavior caused by the oscillatory flow, the bed is allowed to settle under the effect of gravity alone. Therefore, the full simulation domain is initialized with a zero velocity field, and no pressure gradient forcing. The particles then settle into an equilibrium state with the effect of gravity and the bottom wall. Since the bed is initialized in a close-packed structure, the settling process only compressed the particles, but does not cause reshuffling. The final, settled, particle bed is stable and roughly sinusoidal. Once the bed has been stabilized under gravity, the oscillating pressure gradient is implemented, driving the flow and distorting the bed. The shear stress at the rippled bed interface is monitored until it converges, which takes 3 full periods, at which point it is assumed that a quasi-steady state has been achieved.

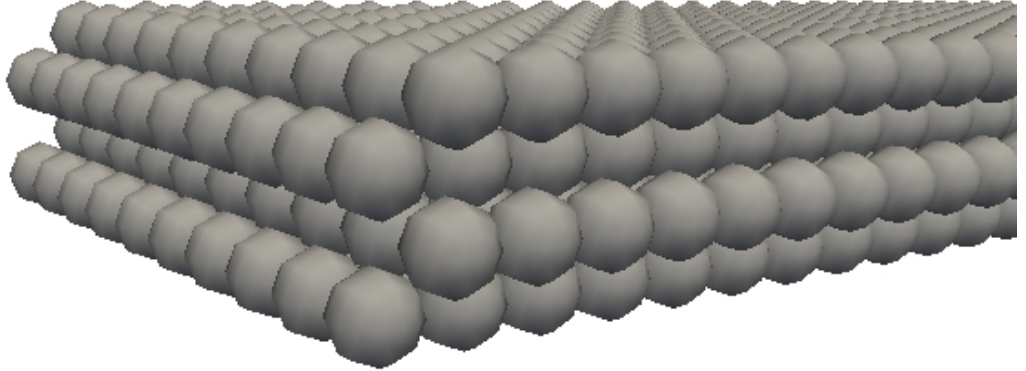


Figure 2.6: Packing configuration of the particle bed. The flat stretch of bed shown here is meant only to illuminate the BCC packing structure of the bed, and is not used in the simulation.

2.3 Results

2.3.1 Data Analysis

Although the experimental data are two-dimensional, and are limited to a single ripple, the numerical work is fully three-dimensional and spans six ripples. Therefore, in order to better compare the datasets, the numerical data are averaged three ways to produce two-dimensional data over a single canonical ripple. Per the work of Scotti and Piomelli (2001), the first type of averaging is done spatially over planes of homogeneity (x-z planes), to generate two-dimensional data. The second is an ensemble approach, which spatially averages all six ripples down to a single ripple. The third is a temporal phase average. The following operator combines the spatial plane averaging and the ensemble spatial averaging, reducing the data to two-dimensions and

a single ripple,

$$\underline{f}(x, y, t) = \sum_{r=1}^6 \frac{1}{TrL_{\lambda_r}L_z} \int_0^T \int_0^{L_{\lambda_r}} \int_0^{L_z} f(x, y, z, t) dx dz dt. \quad (2.76)$$

T is the time over which the function is integrated, λ_r is wavelength of each of the ripples, and L_z is the spanwise width of the domain. The temporal phase averaging, which highlights the influence of the variable pressure gradient, is identified as

$$\langle f \rangle(x, y, t) = \frac{1}{TL_{\lambda_r}L_z} \sum_{n=1}^N \int_0^{L_{\lambda_r}} \int_0^{L_z} f(x, y, z, t + nT) dx dz. \quad (2.77)$$

As noted, the experimental data was collected for eleven periods, therefore the analysis of the experimental data is also phase averaged. Thus, both the numerical and experimental datasets are two-dimensional and span only a single ripple. Since all analysis will use these forms of the data, going forward, the underline and angle brackets will be omitted for simplicity, and the few cases which do not use these averaged datasets will be clearly identified.

2.3.2 Flow Evolution, Vorticity, Velocity Streamlines

Per Bagnold (1946), the ripples in this work are classified as “vortex ripples”, as they have achieved sufficient amplitude to shed vortices under oscillatory flow. To aid in describing the processes at work, the numerical vorticity velocity vector field are used, as shown in Figures 2.7 and 2.8. Although it is commonly used as a method of vortex identification, the Q-criterion of Chong and Perry (1990), is not used here on the experimental data (but will be used to identify three-dimensional vortical structures in the numerical data). Vorticity, which does not discern between shear and vortical components, does a better job in this case of identifying the mechanisms of the flow. Comparing the vorticities of the numerical and experimental data immediately highlights the similarities of the two flows. The vorticity is defined as the curl of the velocity field and describes the local spinning motion of the fluid,

$$\boldsymbol{\omega} = \nabla \times \mathbf{u}_f \quad (2.78)$$

Since the experimental data and the averaged numerical data are two-dimensional, the vorticity becomes

$$\boldsymbol{\omega} = \nabla \times \mathbf{u}_f = \left(\frac{\partial u_j}{\partial x} - \frac{\partial u_i}{\partial y} \right) \mathbf{e}_z, \quad (2.79)$$

where \mathbf{e}_z is the unit vector in the spanwise direction.

At the beginning of the period, phase time 0, a detached vortex can be seen to the left of the ripple, as it was shed from the ripple as the accelerated from right to left (as will be described in the discussion of phase times $5\pi/4$, $3\pi/2$, and $7\pi/4$, below). Although the free stream velocity at this phase is roughly zero, there are clearly non-zero velocities at the bed interface. As the flow accelerates from left to right, this vortex is seen to decay and get swept away at phase time $\pi/4$. A shear layer has also formed on the upstream, or stoss, face and crest of the ripple. At phase time $\pi/2$, the free stream velocity has reached its maximum and the shear layer has continued to grow while the original vortex has been broken up by the free stream. At phase time $3\pi/4$, the flow is still from left to right, but is decelerating. Clearly, the shear layer has developed into a vortex as it is shed on the downstream, or lee, side of the ripple crest. When the free stream velocity has decelerated back to zero at phase time π , the vortex has detached completely from the ripple crest. Expectedly, the second half of the oscillation period mirrors the same processes at the first half, but in the opposite direction.

Figures 2.9 and 2.10 show the vorticities of the experimental flow in the same way that Figures 2.7 and 2.8 did for the numerical data. Although the numerical vorticity is much clearer in showing the shear layer and resulting vortices shed from the ripple crests, at least in part due to the spatial averaging, the experimental data does show good quantitative agreement. In Figure 2.9, the shear layer formed on stoss side of the ripple can be seen most clearly at phase time $\pi/2$ and $3\pi/2$ (when the flow has reversed), as observed in the numerical data. At phase time $3\pi/4$, a section of vorticity is shedding off the lee side of the ripple. Although the source of this high concentration is unclear from the vorticity plot alone, the overlayed velocity vector field shown in Figure 2.10, shows that this high level of vorticity is indeed a vortex. The numerical velocity vector field of Figure 2.8 shows similar trends. This is also made clear at phase time $7\pi/4$, in the opposite direction.

Constant velocity streamlines help to further illuminate the processes of the flow. Figures 2.11 and 2.12 show the velocity vector fields and velocity streamlines for both the numerical and experimental flows, re-

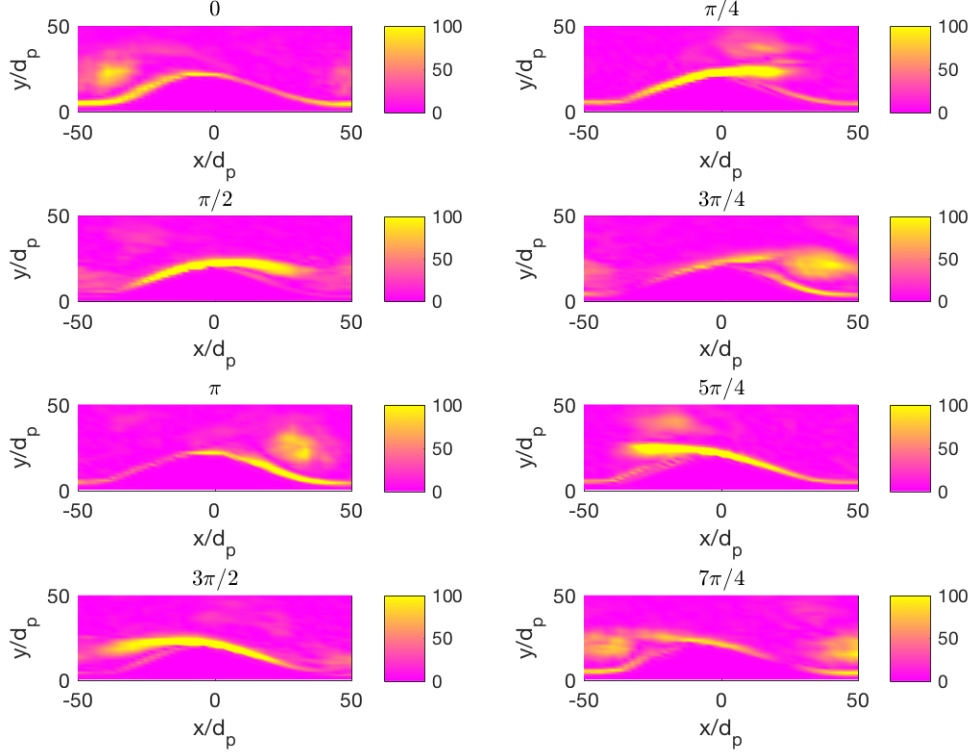


Figure 2.7: Numerical 2D spanwise-averaged vorticity, shown at phase angles $\frac{n\pi}{4}$, for $n = 0, 1, \dots, 6, 7$. The data is normalized by the particle diameter in both directions. The formation of shear layers at the ripple crest is even more evident than in the experimental data. The formation of the vortices off the ripple crest can be seen clearly, and in addition, as the flow changes directions, the old vortices are shed into the free stream, as at phase angle $5\pi/4$.

spectively. In both cases, a vortex is clearly identified at phase time 0. The numerical vortex, having been shed when the flow was oriented right to left, is centered roughly $40d_p$ to the left of the ripple crest and $30d_p$ in the wall-normal direction. The experimental vortex is centered roughly $35d_p$ to the left of the ripple crest and $35d_p$ in the wall-normal direction. At phase times $\pi/4$, $\pi/2$, and $3\pi/4$, the separated flow indicates a shear layer becoming a vortex. At phase time $7\pi/4$, this vortex, albeit in the opposite direction, is clearly identifiable as forming in the wake of the separated flow. The numerical data shows this particularly well at phase time $3\pi/2$, per Figure 2.11.

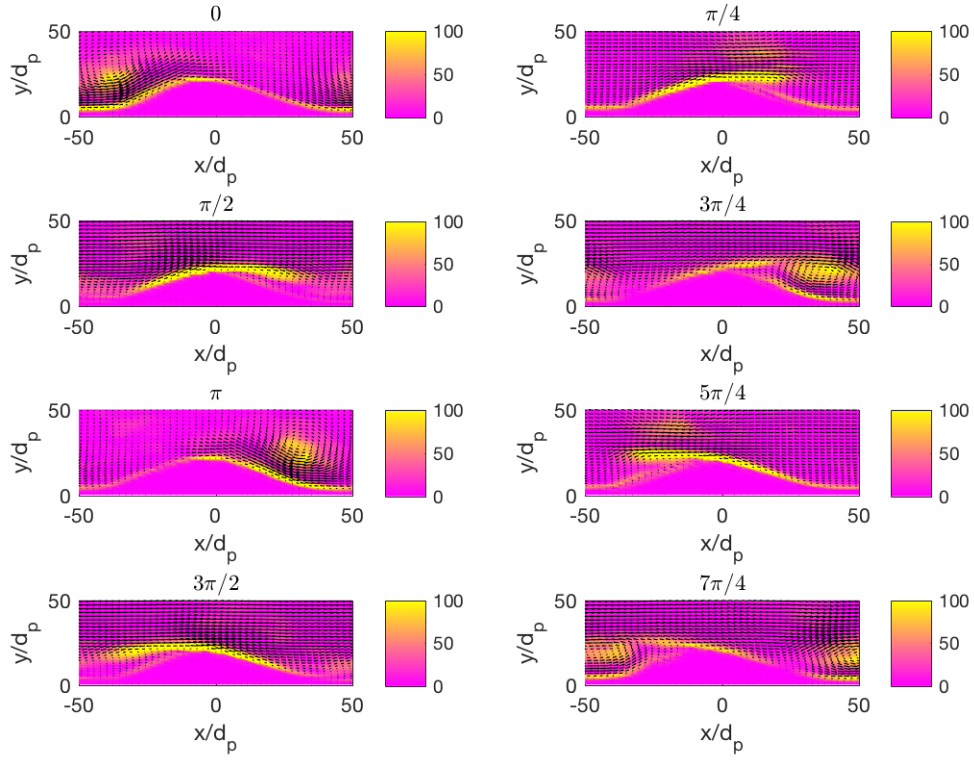


Figure 2.8: Numerical velocity field overlayed on vorticity, shown at phase angles $\frac{n\pi}{4}$, for $n = 0, 1, \dots, 6, 7$. The data is normalized by the particle diameter in both directions. The velocity field helps to identify the shed vortices.

Overall, the numerical results show very good qualitative agreement with the experimental work. The LES is able to capture the formation of the shear layer on the upstream side of the ripple, which develops into a vortex on the downstream side, and is shed into the valley between ripples.

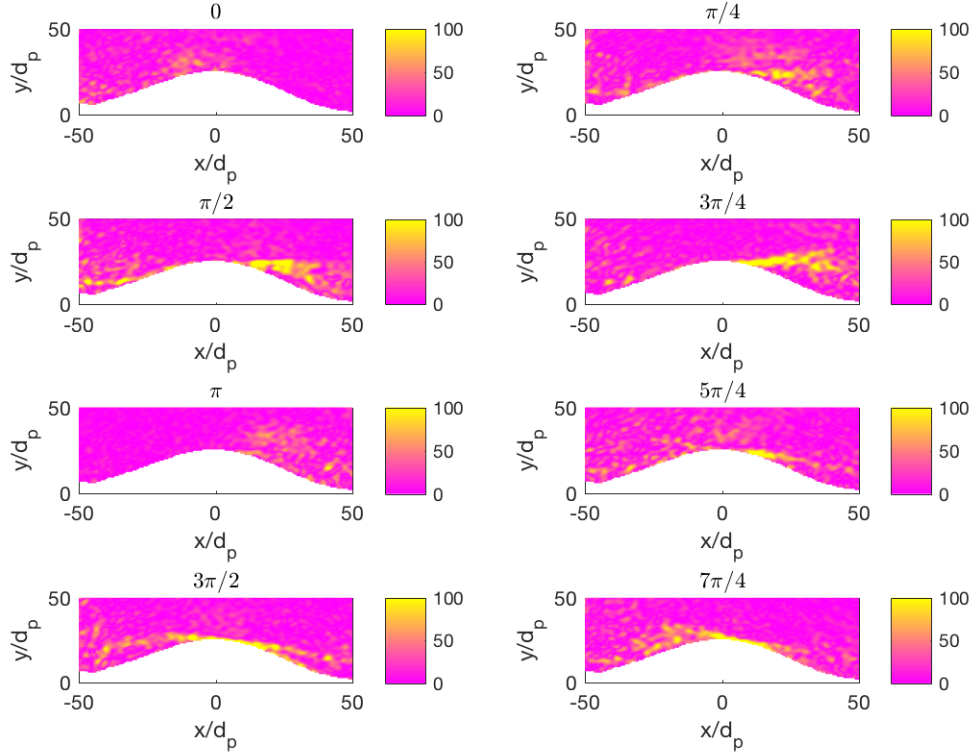


Figure 2.9: Experimental vorticity, shown at phase angles $\frac{n\pi}{4}$, for $n = 0, 1, \dots, 6, 7$. The data is normalized by the particle diameter in both directions. The formation of shear layers at the ripple crest is seen at phase angles in which the pressure gradient is producing higher free stream velocities. The resulting vortex shedding, can be seen most clearly at phase angles $\pi/2, 3\pi/4, 3\pi/2$, and $7\pi/4$.

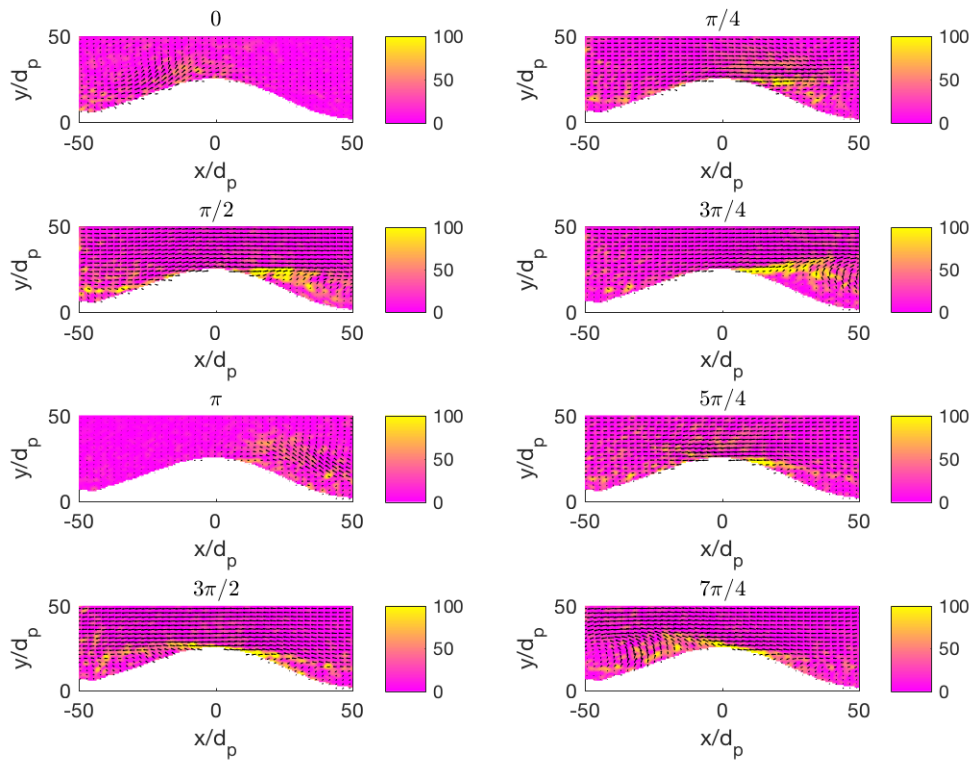


Figure 2.10: Experimental velocity field overlayed on vorticity, shown at phase angles $\frac{n\pi}{4}$, for $n = 0, 1, \dots, 6, 7$. The data is normalized by the particle diameter in both directions. The velocity field helps to identify the shed vortices at phase angles $3\pi/4$ and $7\pi/4$.

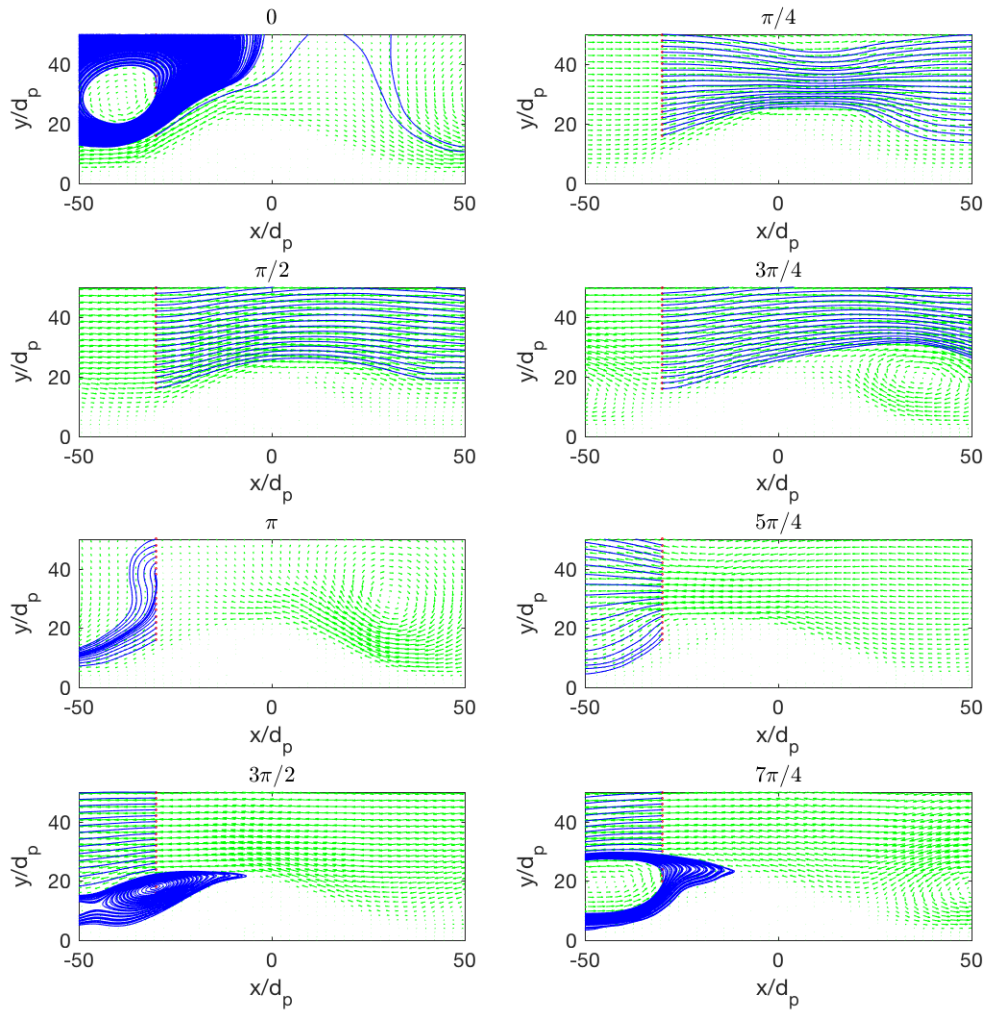


Figure 2.11: Numerical velocity streamlines overlayed on the 2D spanwise-averaged velocity field, shown at phase angles $\frac{n\pi}{4}$, for $n = 0, 1, \dots, 6, 7$. Only a single ripple is shown, and the data is normalized by the particle diameter in both directions.

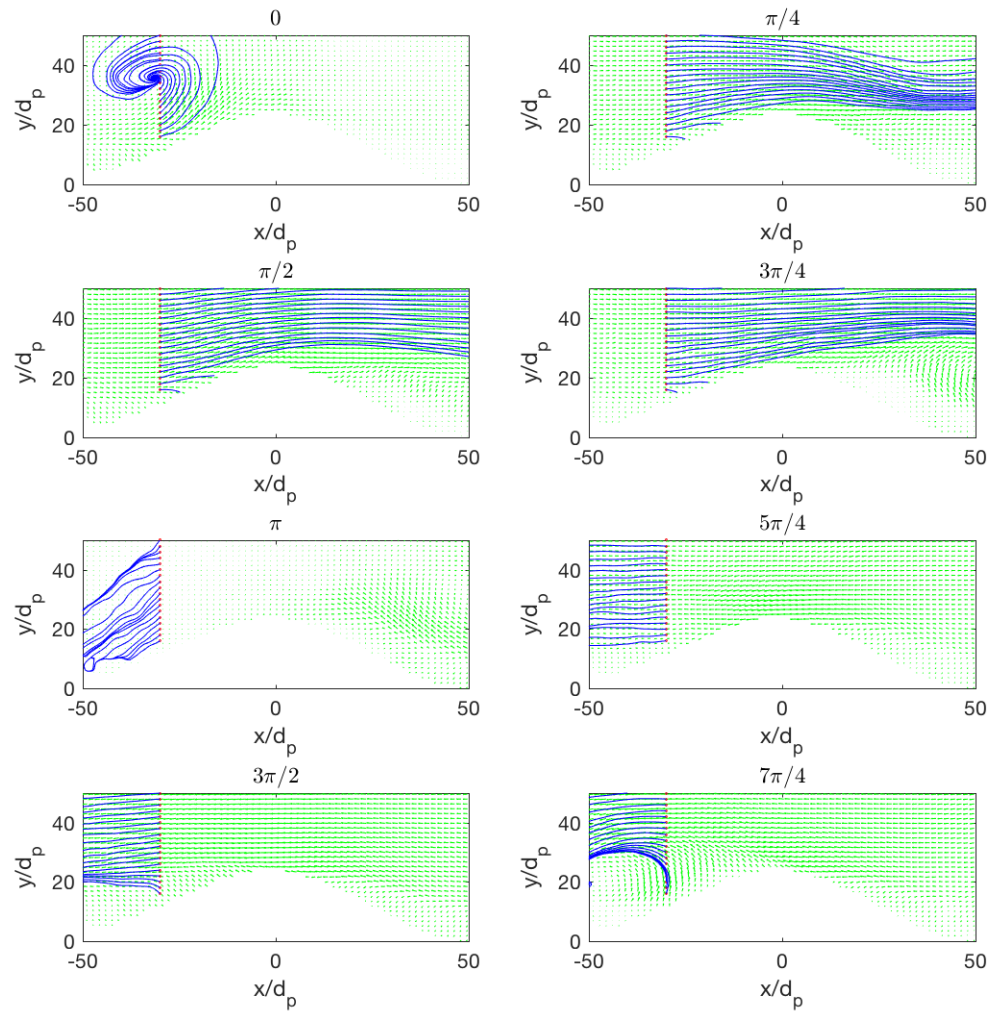


Figure 2.12: Experimental velocity streamlines overlayed on the velocity field, shown at phase angles $\frac{n\pi}{4}$, for $n = 0, 1, \dots, 6, 7$. The data is normalized by the particle diameter in both directions.

2.3.3 Wall-Normal Flow Statistics

Two approaches are used to compare the wall-normal flow statistics of the experimental and numerical data. The first consists of wall-normal statistics located at the ripple crest, ripple trough, and half way up the left-hand side ripple face. The second compares wall-normal statistics that are spatially averaged over the entirety of the ripple, which results in a single wall-normal profile for any given statistic. This approach analyzes the effective roughness of the wall on a macroscopic scale. It should be noted that because the numerical simulation solves the volume-filtered Navier-Stokes equations everywhere in the domain, \mathbf{u}_f data is available everywhere, including “within” the ripple. Therefore all the numerical wall-normal statistical profiles span all the way down to the bottom wall. The experimental data does not include fluid velocity data within the ripple, where it is assumed to be zero. So where applicable, the experimental wall-normal statistical profiles are shown only where data was recorded. In the cases where this is true, the profiles may not extend all the way to the bottom wall.

Figures 2.13, 2.14, and 2.15 compare the wall-normal streamwise velocity profiles at the ripple crest, trough and face, respectively. The streamwise velocities are normalized by the maximum free stream velocity, U_∞ , and the wall-normal location is normalized by h . On the whole, the numerical model does a very good job of predicting the velocity profile at the crest and face. However, at the ripple trough, the numerical model seems to overpredict the magnitude of the inflection point velocity. Of course, the ripple shape in the experiment is not completely sinusoidal, as in the numerical work, and the troughs are where the morphologies differ the most (as will be discussed in following sections). Therefore, it is not surprising to see discrepancies in the profiles, particularly at the ripple trough.

Spatially averaging the streamwise velocity profiles over the entire wavelength of the ripple treats the ripple effectively as surface roughness. Figure 2.16 shows that trends of the experimental work are captured by the numerical model, albeit with a consistent slight over-prediction of the magnitude of the streamwise velocity.

The comparison of the wall-normal streamwise velocity profiles have given a clear indication that the experimental phases-averaged velocities are well predicted by the spatially and phase-averaged numerical results. In order to examine the deviations from these averaged velocities, a couple different quantities are examined. The turbulent kinetic energy (TKE) is a measure of the intensity of a turbulent flow. Using the

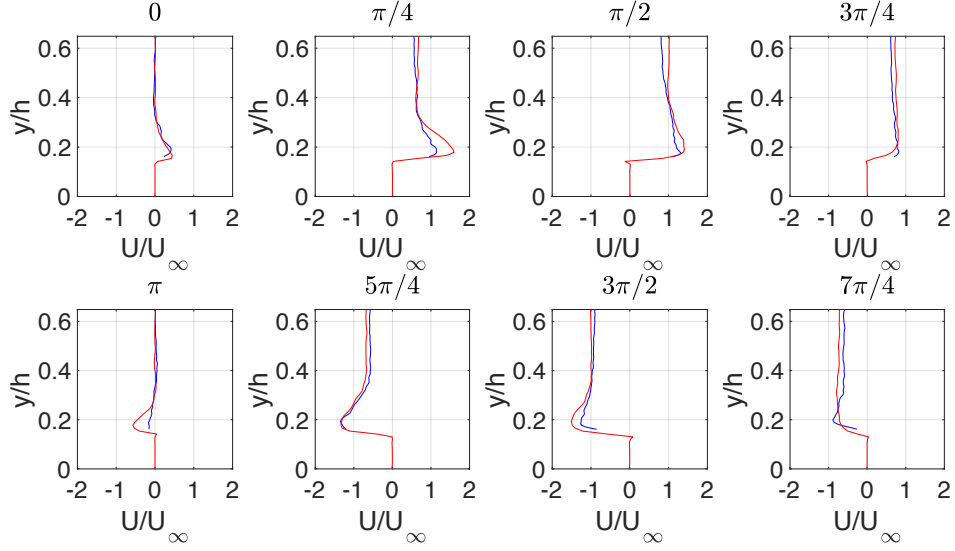


Figure 2.13: Streamwise velocity profiles in the wall-normal direction, at the ripple crest, shown at phase angles $\frac{n\pi}{4}$, for $n = 0, 1, \dots, 6, 7$. The velocity is normalized by the maximum achieved freestream streamwise velocity, U_∞ . The wall-normal position is normalized by the half-height of the channel, h . The experimental results are denoted by a blue line, and the numerical results by a red line. In some cases, the range of the PIV data was limited, therefore, the entire profile was not available.

notation described in Section 2.3.1, the experimental data is phase-averaged, which means that at any point in the flow, the instantaneous velocity can be broken into a mean component, $\underline{\mathbf{u}_f}(x, y, t_{phase})$, and a fluctuation, $\mathbf{u}'_f(x, y, t)$, where

$$\mathbf{u}_f(x, y, t) = \langle \mathbf{u}_f \rangle(x, y, t_{phase}) + \mathbf{u}'_f(x, y, t). \quad (2.80)$$

Analogously, the numerical data is phase-averaged and averaged in space,

$$\mathbf{u}_f(x, y, z, t) = \langle \underline{\mathbf{u}_f} \rangle(x, y, t_{phase}) + \mathbf{u}'_f(x, y, t). \quad (2.81)$$

In both cases, the three components of velocity at any given point in time and space have a mean value and a fluctuation. These fluctuations reflect the intensity of the turbulence at that point. In order to quantify the

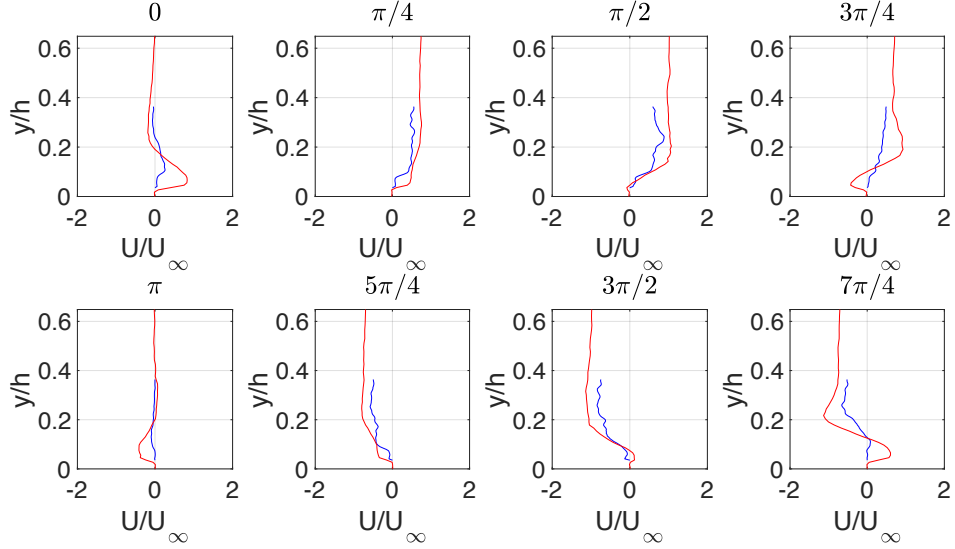


Figure 2.14: Streamwise velocity profiles in the wall-normal direction, at the ripple trough, shown at phase angles $\frac{n\pi}{4}$, for $n = 0, 1, \dots, 6, 7$. The velocity is normalized by the maximum achieved freestream streamwise velocity, U_∞ . The wall-normal position is normalized by the half-height of the channel, h . The experimental results are denoted by a blue line, and the numerical results by a red line. In some cases, the range of the PIV data was limited, therefore, the entire profile was not available.

intensity, the TKE is defined as half the RMS of the velocity fluctuations:

$$TKE(x, y, t) = \frac{1}{2} \sqrt{\frac{u'^2_f(x, y, t) + v'^2_f(x, y, t) + w'^2_f(x, y, t)}{3}}, \quad (2.82)$$

where u' , v' , and w' are the streamwise, wall-normal, and spanwise velocity components of $\mathbf{u}'_f(x, y, t)$, respectively. As was done with the velocity profiles, spatially averaging the TKE profiles over the entire wavelength of the ripple treats the ripple effectively as surface roughness. Figure 2.17 shows that trends of the experimental work are captured by the numerical model, albeit with a consistent slight over-prediction of the magnitude of the streamwise velocity. Not only are the magnitudes of the TKE profiles consistent, but the shape of the curves show good agreement between the experimental and numerical work. Again, like the velocity profiles, the numerical model very slightly over predicts TKE in most phases and locations.

The other quantity used to examine the deviations from these averaged velocities is the Reynolds shear stress. The Reynolds shear stress, $\langle u'_i u'_j \rangle$, is a function of the fluctuations in the streamwise and wall-normal directions. Its importance lies in the fact than RANS models must model this term accurately to correctly

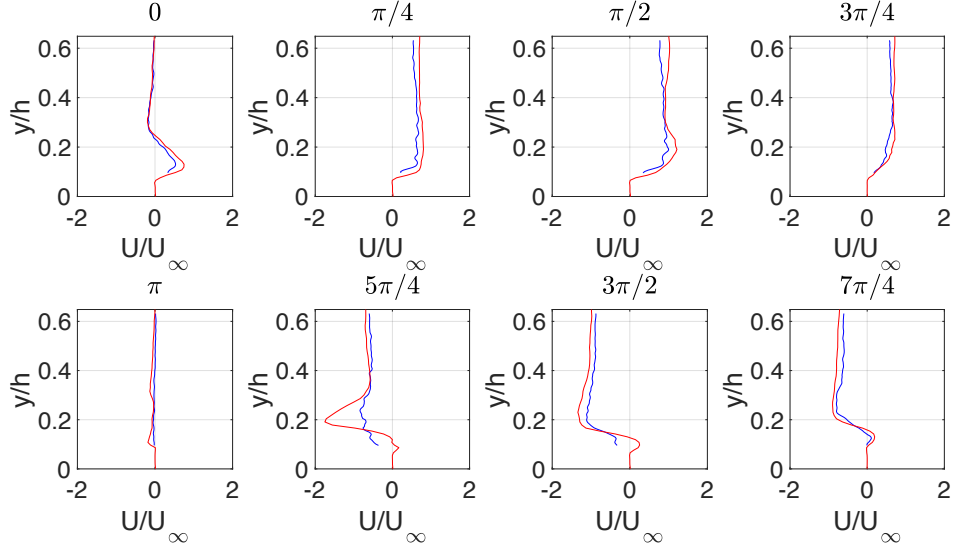


Figure 2.15: Streamwise velocity profiles in the wall-normal direction, at the ripple face, shown at phase angles $\frac{n\pi}{4}$, for $n = 0, 1, \dots, 6, 7$. The velocity is normalized by the maximum achieved freestream streamwise velocity, U_∞ . The wall-normal position is normalized by the half-height of the channel, h . The experimental results are denoted by a blue line, and the numerical results by a red line. In some cases, the range of the PIV data was limited, therefore, the entire profile was not available.

predict the physics of the flow (see Appendix B for full details on the assumptions and approximations in Reynolds Averaging the Navier-Stokes equations). The Reynolds shear stress is normalized by the square of the maximum achieved freestream streamwise velocity, U_∞ . Figure 2.18 averages the Reynolds stress profiles over the entirety of the ripple wavelength. The trends in the profiles are well predicted by the numerical model, with some deviation in the location of maximum values.

The LES does an excellent job of predicting the wall-normal profiles of the streamwise velocity and the TKE. In addition, the LES does an adequate job of predicting the qualitative behavior of the Reynolds stress, although there is some discrepancy in magnitude.

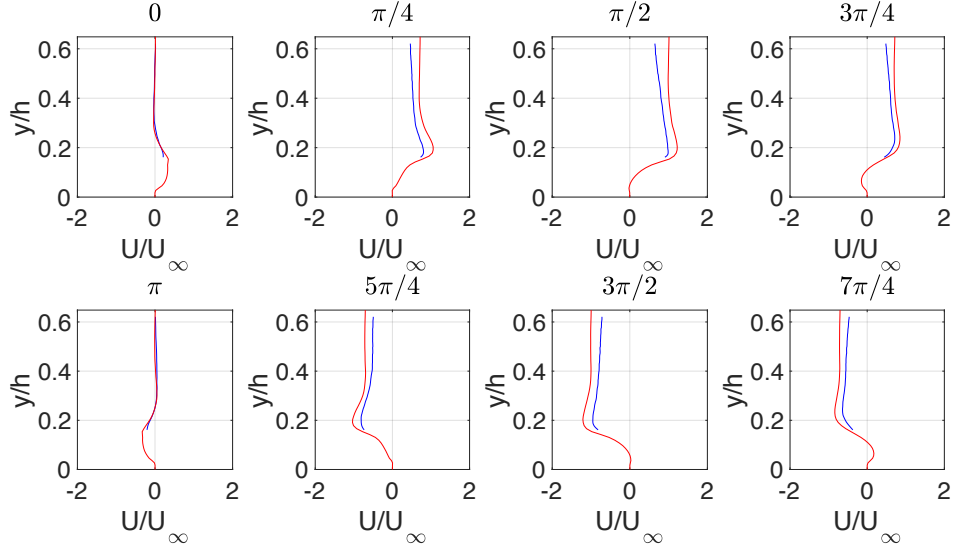


Figure 2.16: Streamwise velocity profiles in the wall-normal direction, averaged over the entire wavelength of the ripple, shown at phase angles $\frac{n\pi}{4}$, for $n = 0, 1, \dots, 6, 7$. The velocity is normalized by the maximum achieved freestream streamwise velocity, U_∞ . The wall-normal position is normalized by the half-height of the channel, h . The experimental results are denoted by a blue line, and the numerical results by a red line. In some cases, the range of the PIV data was limited, therefore, the entire profile was not available.

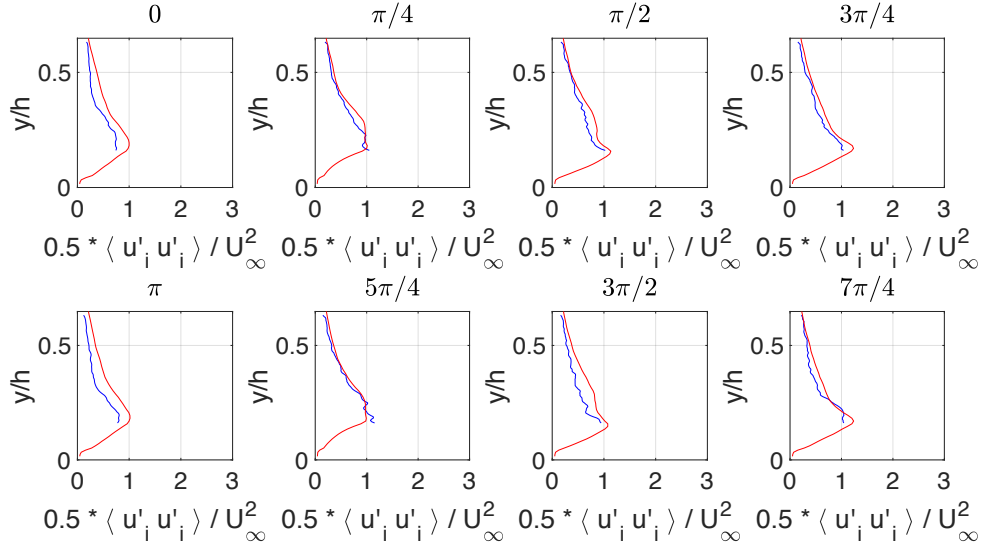


Figure 2.17: Turbulent kinetic energy (TKE) wall-normal profiles, averaged over the entire wavelength of the ripple, shown at phase angles $\frac{n\pi}{4}$, for $n = 0, 1, \dots, 6, 7$. The TKE is normalized by the square of the maximum achieved freestream streamwise velocity, U_∞ . The wall-normal position is normalized by the half-height of the channel, h . The experimental results are denoted by a red line, and the numerical results by a blue line. In some cases, the range of the PIV data was limited, therefore, the entire profile was not available.

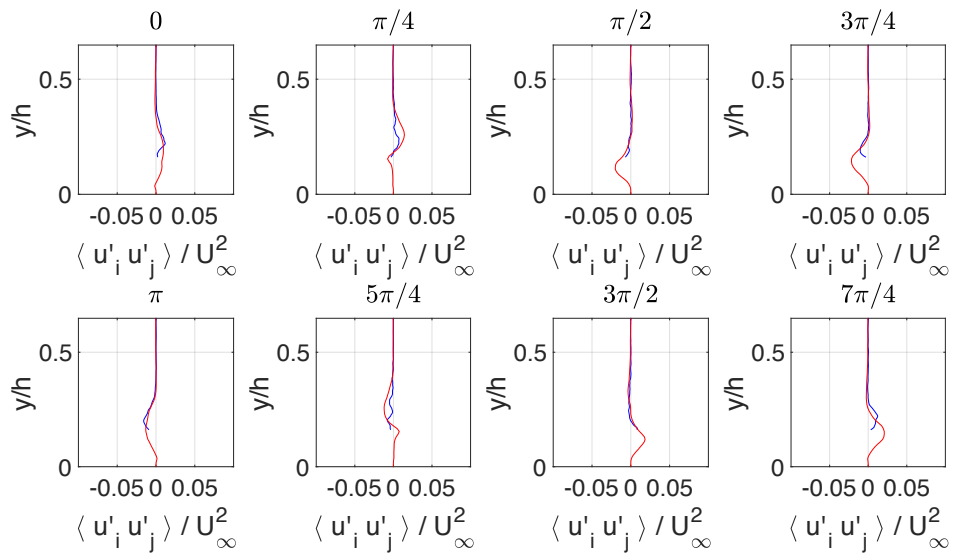


Figure 2.18: Reynolds stress wall-normal profiles, averaged over the entire wavelength of the ripple, shown at phase angles $\frac{n\pi}{4}$, for $n = 0, 1, \dots, 6, 7$. The Reynold stress is normalized by the square of the maximum achieved freestream streamwise velocity, U_∞ . The wall-normal position is normalized by the half-height of the channel, h . The experimental results are denoted by a blue line, and the numerical results by a red line. In some cases, the range of the PIV data was limited, therefore, the entire profile was not available.

2.3.4 Bed Shear Stress

The shear stress at the bed interface is crucial to understanding the coupling between the bed morphology and the flow dynamics. The bed shear stress is defined as

$$\tau_b = \mu \frac{\partial u}{\partial y} \Big|_{y=interface}, \quad (2.83)$$

and the shear stress at the top wall is

$$\tau_t = \mu \frac{\partial u}{\partial y} \Big|_{y=2h}. \quad (2.84)$$

Of course, correctly identifying the bed interface significantly affects the τ_b calculations. As is described in detail in Section 2.3.6, in this work, the bed interface is defined according to the solid volume fraction. At any given location, if the solid volume fraction is above the threshold value, then that location is defined as being a part of the bed. Otherwise, when the solid volume fraction is less than the threshold value, that location is defined as being in the flow, above the bed.

Traditionally, a no-slip condition is assumed to exist at the interface between the solid and fluid phases. This is accurate in the case of a standard wall interface, but the assumption breaks down when the solid phase can move. In classical models, which treat the solid phase as a continuum, such as defining the interface with the Exner equation, a no-slip condition is assumed at the bed-fluid interface. Per the plots of bed shear stress calculated by Blondeaux (1991) in Figure 2.19, in the case of no-slip interface condition, a negative shear bed shear stress will always result in momentum transfer from right to left, and a positive bed shear stress will always result in momentum transfer from left to right. Therefore, the negative values of shear bed stress on the right hand side of the ripple face, and the positive values on the left hand side, would combine to pull the solid phase from the ripple troughs to the peaks, and maintain the integrity of the ripple shape. Alternatively, if the bed shear stresses were observed to be positive on the right hand side, and negative on the left hand side, the dynamics of the fluid would act to flatten the ripple. So, with a no-slip condition at the interface, the evolution of the bed shear stress as described by Blondeaux does square with intuition.

However, when the bed is composed of individual particles, as in nature, the individual particles that define the bed-fluid interface are not immobile, and a no-slip boundary condition does not apply to the inter-

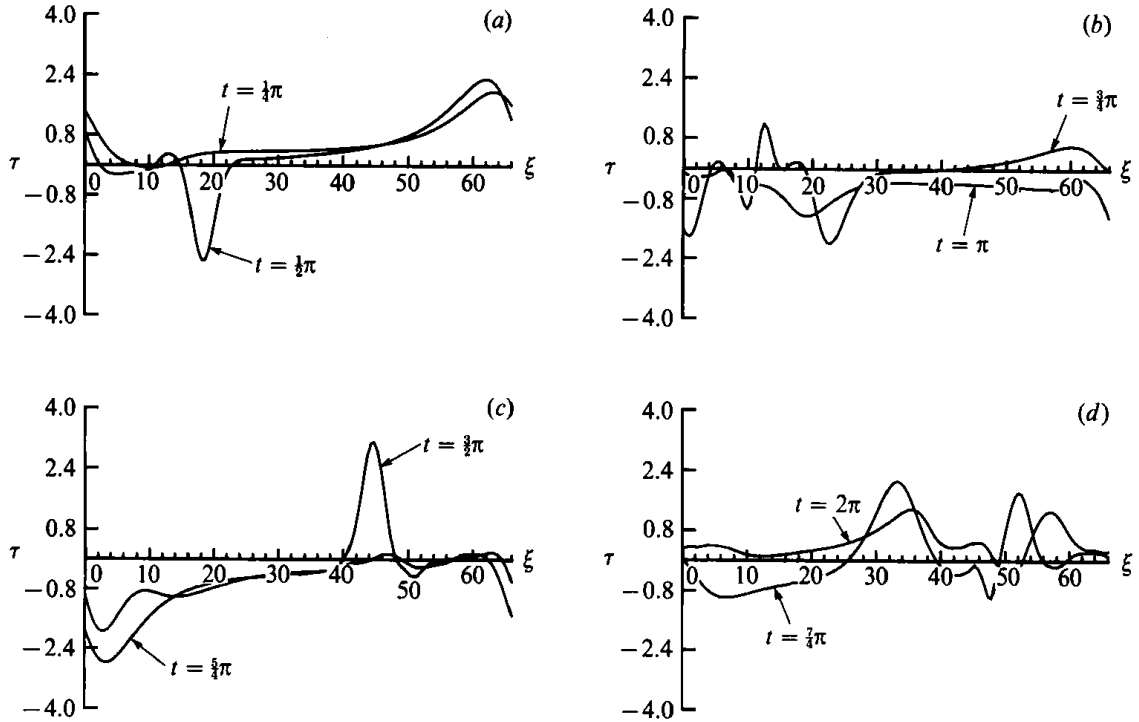


Figure 2.19: Bed shear stress over an immobile rippled bed, per Blondeaux (1991). The ripple peak are at the extants of the plot, and the ripple trough is centered. A no-slip condition is assumed at the bed-fluid interface. As the flow moves from left to right, a strong negative peak is observed on the downstream ripple face. Therefore, the fluid would compel the solid phase to move from the trough to the peak, thus maintaining or increasing the ripple peak. The opposite is observed when the flow reverses.

face as a whole. Naturally, a no-slip boundary condition does exist at the surface of each individual particle, but not necessarily to the bed-fluid interface itself. This speaks to the vagaries of the definition a bed-fluid interface. If a thin layer of mobile particles at the surface of the bed are sliding over an immobile section of the bed, the definition of the bed-fluid interface is subject to interpretation. As shown in Figure 2.20, if the bed-fluid interface is not a rigid no-slip surface, a vortex that impacts the interface may in fact penetrate the interface, resulting in greater velocity magnitudes at (or below) the interface itself than in the directly adjacent fluid.

This phenomena is simplified in Figure 2.21. The right hand side face of the ripple is approximated by a linear interface. The interface-normal direction is denoted y and the fluid velocity u is defined as parallel to the interface. The dashed line indicates the interface as determined by the solid volume fraction. The solid line delineates the immobile particles from the mobile particles. If the solid line is taken as the interface,

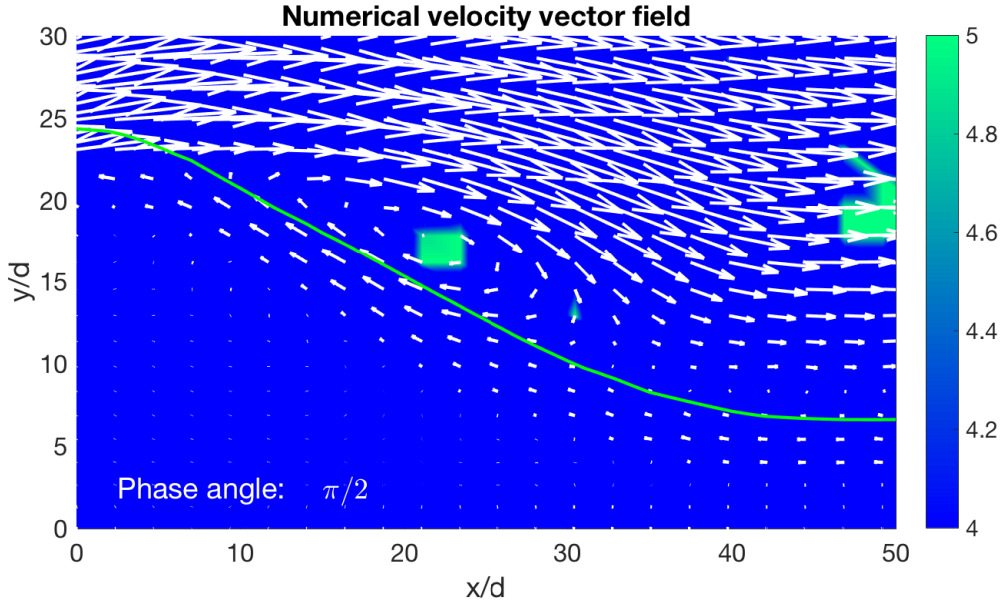


Figure 2.20: Bed-fluid interface and velocity field superimposed over the Q-criterion field. Only the right hand side of the a single ripple is shown. It becomes clear that there is still fluid velocity “within” the ripple as a vortex interacts with the ripple.

the classical no-slip boundary condition assumption is valid. To illustrate, the bed shear stress between points 2 and 1, $\tau_{2 \rightarrow 1}$, would be negative because the fluid velocity at point 2 is negative and zero at point 1. However, the bed shear stress between points 3 and 2, $\tau_{3 \rightarrow 2}$, would be positive, despite the fact that velocities at both points are negative. This occurs because the velocity at point 3 is smaller in magnitude than at point 2. So despite describing the same physical process, the bed shear stresses are opposite in sign depending on the definition of the bed-fluid interface. Naturally, this appears to merely be an inconsistency in the definition of the bed-fluid interface. As will be shown in Section 2.3.6, this work utilizes the methodology of Kidanemariam and Uhlmann (2014) to define the interface by solid volume fraction. This approach was adopted because it matched the qualitative behavior of the system. When the interface was defined according to the “immobile” bed, as shown in Figure 2.21, far too many particles were defined as being in the fluid, when they were essentially immobile at the bed interface. This discrepancy is due to the fact that as the fluid imparts momentum to a packet of particles at the interface, they may move momentarily as a unit, but ultimately return to their original positions. Therefore, it becomes clear than the definition of a fluid-bed

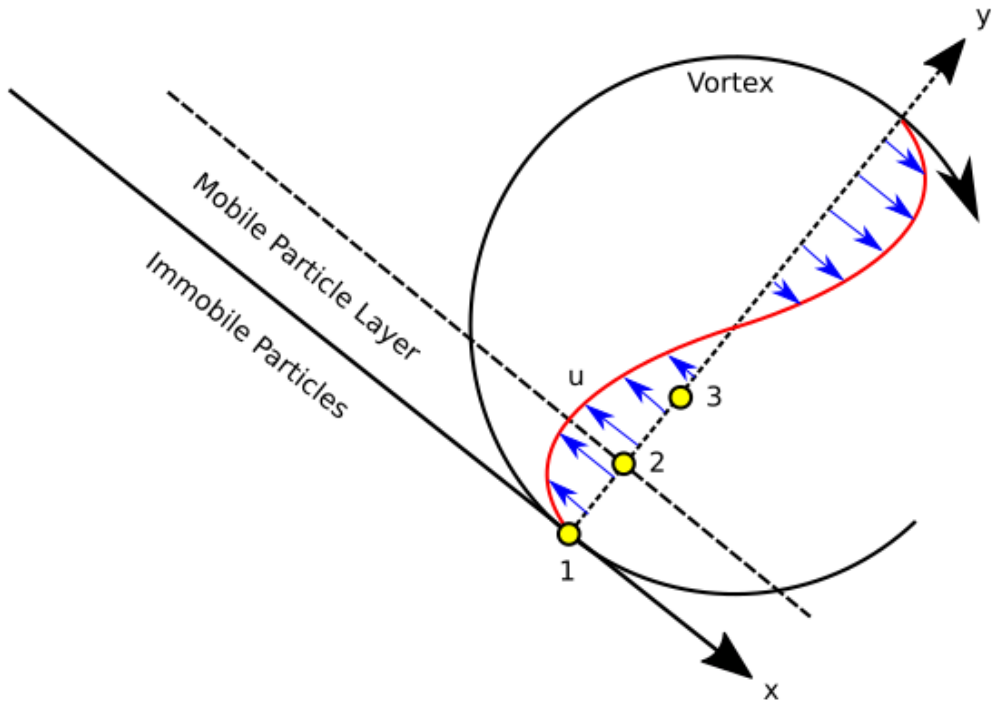


Figure 2.21: Simplified view of a vortex impacting the right hand side of a ripple. The vortex has been shed as the fluid moves from left to right, and then reverses directions. Depending on how the bed-fluid interface is defined, the sign of the calculated bed shear stress may be affected. For simplicity, x is interface-parallel, the y -direction is defined as the wall-normal, and the fluid velocity u is defined as parallel to the bed-fluid interfaces, in the negative x -direction.

interface as a continuum with a no-slip boundary condition gravely underestimates the importance of the individual particle behavior, and misses the physics driving the interaction between the ripple and the fluid.

Figure 2.22 shows the averaged ripple shear stresses. The experimental data shows a maximum to the right of the bed shear stress as phase times $3\pi/2$ and $7\pi/4$, which is expected, as the flow is moving from right to left and generating a shear layer on the stoss side of the ripple face. However, in the first half of the oscillation period, the experimental data does not display distinct bed shear stress maximums. The numerical data does a good job of predicting the magnitude of the bed shear stress, but seems to deviate from the experimental data in identifying peaks in the bed shear stress. The LES data show maximum bed shear stresses on the lee side of the ripple peaks. Figure 2.23 compares the evolution of the numerical bed shear stress at different locations on the ripple peak. As originally noted by Benjamin (1959) and Kennedy (1963), the phase lag between the bed shear stress and freestream velocity is clearly identified. The maximum bed shear stress at

the ripple crest occurs at phase times $3\pi/4$ and $7\pi/4$, whereas the freestream velocity maximums occur at $\pi/2$ and $3\pi/2$. So in this work, the lag between the bed shear stress and freestream velocity is roughly $\pi/4$.

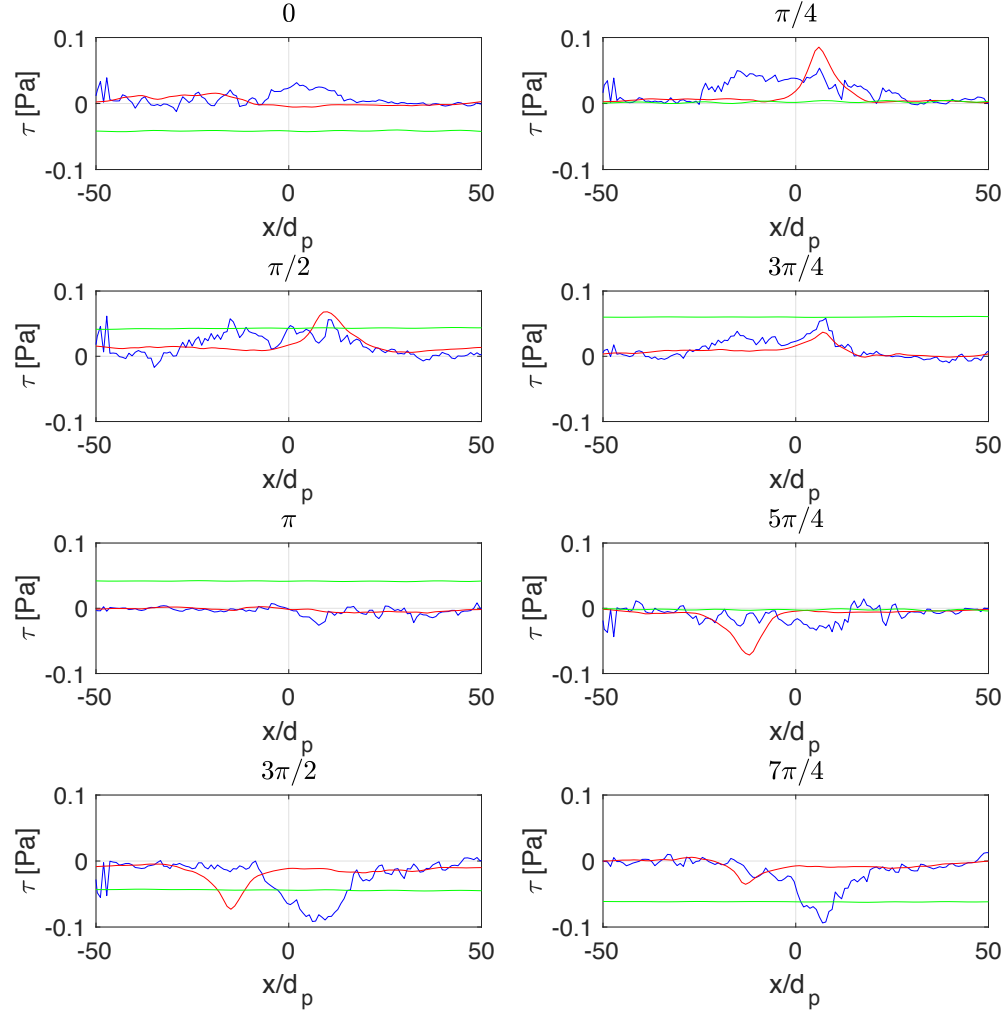


Figure 2.22: Experimental bed shear stress (blue line), numerical bed shear stress (red line), and numerical top wall shear stress (green line), over a single ripple. The first half of the oscillation presents much closer qualitative bed shear stresses. There is phase lag, of approximately $\pi/4$, between top wall shear stress and the pressure gradient forcing, as the top wall shear stress does not go to zero until phase angles $\pi/4$ and $5\pi/4$.

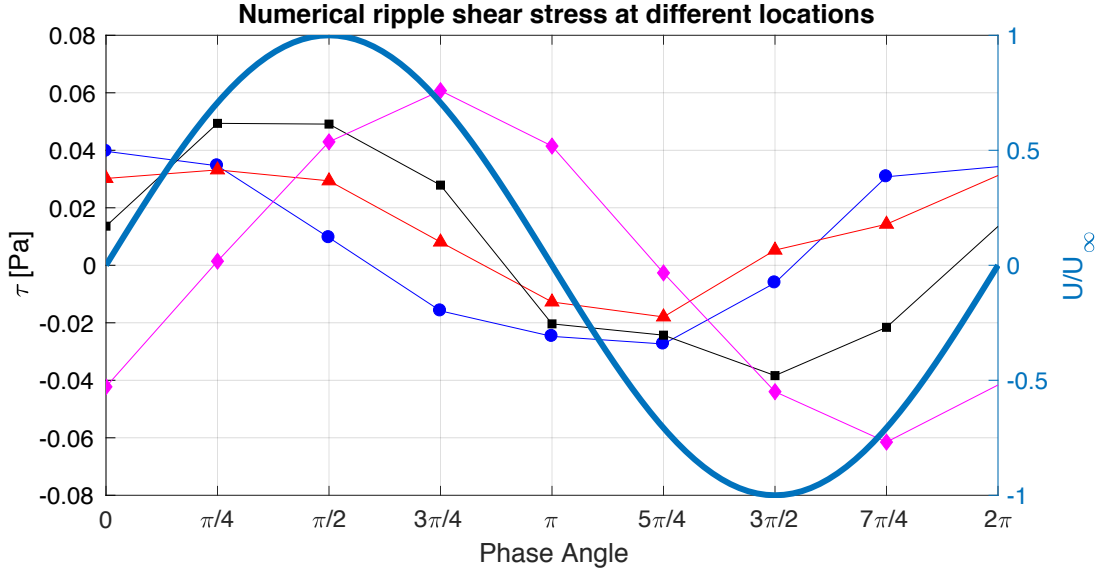


Figure 2.23: Numerical free stream velocity (thick blue line) and the evolution of bed shear stress at different locations on the ripple. The top wall is denoted by magenta line and diamond marker, the ripple crest is denoted by the black line with square marker, the ripple trough is denoted by the blue line with circle marker, and the ripple face is denoted by the red line with triangle marker. A phase lag of $\pi/4$ is observed between the bed shear stress at the top wall and the free stream velocity. By contrast, the further down the ripple, the greater the phase lead between the bed shear stress and the freestream velocity.

2.3.5 Q-Criterion & Vortex Identification

Although vorticity quantifies the swirling effects of the flow, it cannot discern between shear and vortices. Per the work of Chong et al. (1990), the flow of a continuum can be completely categorized by the invariants of the rate of deformation tensor. In identifying vortical structures in a flow, this tensor is the velocity gradient tensor, $\nabla \mathbf{u}_f$. To determine the invariants, the velocity gradient tensor is first broken into symmetric and antisymmetric components, which represent the rate-of-strain and rotation tensors, respectively. The rate of strain tensor is $S_{ij} = \frac{1}{2} \left(\frac{\partial u_i}{\partial x_j} + \frac{\partial u_j}{\partial x_i} \right)$, and the rotation tensor is $\Omega_{ij} = \frac{1}{2} \left(\frac{\partial u_i}{\partial x_j} - \frac{\partial u_j}{\partial x_i} \right)$. The eigenvalues, λ , and eigenvector, \mathbf{e} , of $\nabla \mathbf{u}_f$ are determined as follows:

$$[\nabla \mathbf{u}_f - \lambda \mathbf{I}] \mathbf{e}, \quad (2.85)$$

where \mathbf{I} is the identity matrix. Then the determinant of $[\nabla \mathbf{u}_f - \lambda \mathbf{I}]$ is set to zero and the characteristic equation identified:

$$|\nabla \mathbf{u}_f - \lambda \mathbf{I}| = 0, \quad (2.86)$$

$$\lambda^3 + P\lambda^2 + Q\lambda + R = 0. \quad (2.87)$$

P , Q , and R are the invariants of the velocity gradient tensor, and fully define its features. The first invariant is the sum of the rank one determinants on the diagonal,

$$P = -\text{trace}[\nabla \mathbf{u}_f] = -\left(\frac{\partial u}{\partial x} + \frac{\partial v}{\partial y} + \frac{\partial w}{\partial z}\right) = -S_{ii}. \quad (2.88)$$

The second invariant is the sum of the rank two determinants along the diagonal,

$$Q = \begin{vmatrix} \frac{\partial u}{\partial x} & \frac{\partial u}{\partial y} \\ \frac{\partial v}{\partial x} & \frac{\partial v}{\partial y} \end{vmatrix} + \begin{vmatrix} \frac{\partial u}{\partial x} & \frac{\partial u}{\partial z} \\ \frac{\partial w}{\partial x} & \frac{\partial w}{\partial z} \end{vmatrix} + \begin{vmatrix} \frac{\partial v}{\partial y} & \frac{\partial v}{\partial z} \\ \frac{\partial w}{\partial y} & \frac{\partial w}{\partial z} \end{vmatrix} = \frac{1}{2}(P^2 - \text{trace}[\nabla \mathbf{u}_f^2]) = \frac{1}{2}(P^2 - S_{ij}S_{ji} - \Omega_{ij}\Omega_{ji}). \quad (2.89)$$

The third invariant the is the rank three determinant,

$$R = \begin{vmatrix} \frac{\partial u}{\partial x} & \frac{\partial u}{\partial y} & \frac{\partial u}{\partial z} \\ \frac{\partial v}{\partial x} & \frac{\partial v}{\partial y} & \frac{\partial v}{\partial z} \\ \frac{\partial w}{\partial x} & \frac{\partial w}{\partial y} & \frac{\partial w}{\partial z} \end{vmatrix} = -\det[\nabla \mathbf{u}_f] \quad (2.90)$$

$$= \frac{1}{3}(-P^3 + 3PQ - \text{trace}[\nabla \mathbf{u}_f^3]) \quad (2.91)$$

$$= \frac{1}{3}(-P^3 + 3PQ - S_{ij}S_{jk}S_{ki} - 3\Omega_{ij}\Omega_{jk}\Omega_{ki}). \quad (2.92)$$

The characteristic equation can have distinct real roots, repeating real roots, or one real and one pair of complex conjugate roots. Chong et al. (1990) suggest the following definition of a vortex, “a vortex core is a region of space where the vorticity is sufficiently strong to cause the rate-of-strain tensor to be dominated by the rotation tensor, i.e., the rate-of-deformation tensor has complex eigenvalues.” Adding, “Since this definition depends only on the properties of the deformation tensor, it is independent of the frame of reference

of the observer.” In taking this approach, the second invariant Q contains squared measures of both the rate of strain and rotation tensors, $Q = \frac{1}{2}(P^2 - S_{ij}S_{ji} - \Omega_{ij}\Omega_{ji})$. Therefore, when $Q > 0$, the flow is dominated by rotation at that location, and when $Q < 0$, the flow is dominated by shear. Figures 2.24, 2.25, 2.26, 2.27, and 2.28 show iso-contours of the second invariant Q over the first half of an oscillation period. At phase time 0, distorted and detached spanwise vortices are seen on the lefthand side of the ripple faces, as they have just been shed from flow moving from right to left. At phase time $\pi/4$, the flow accelerates from left to right, and these spanwise vortices are broken up and ejected away from the bed. By phase time $\pi/2$, the freestream velocity has reached its maximum and the near bed unsteady flow is dominated by streamwise structures in the shear layer, mostly forming on the stoss side of the ripples. As the flow decelerates at phase time $3\pi/4$, the streamwise structures are converted into spanwise vortical structures which begin to form on the lee side of the ripples. By the time the freestream velocity is back to zero at phase time π , these distorted spanwise vortices have detached from the ripples and can be seen on the righthand side of the crest ripples, mirroring the detached vortices at phase time 0.

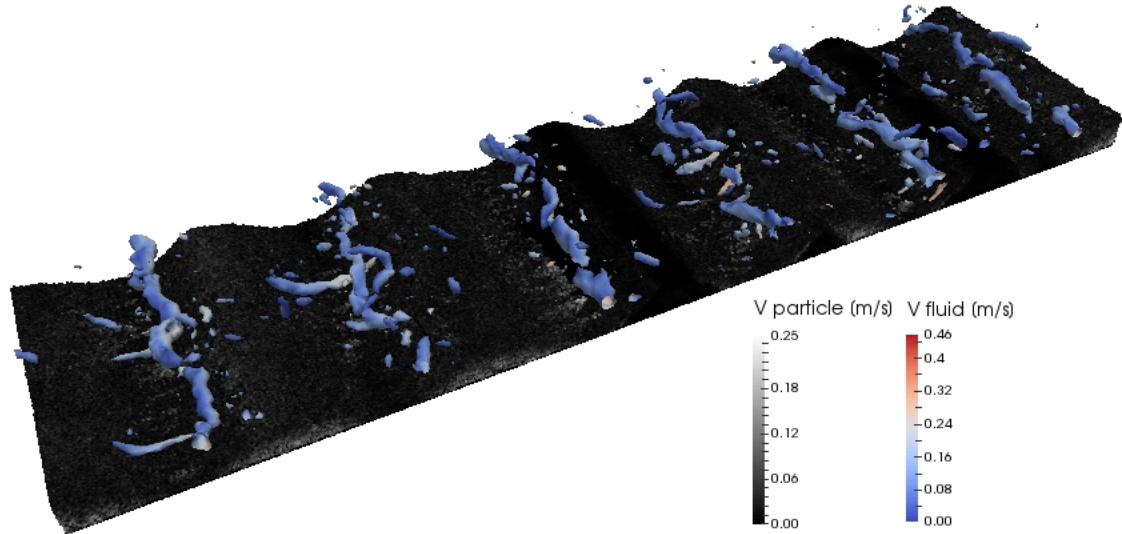


Figure 2.24: Numerical Q-criterion isocontours at phase time 0. Free stream velocity is zero.

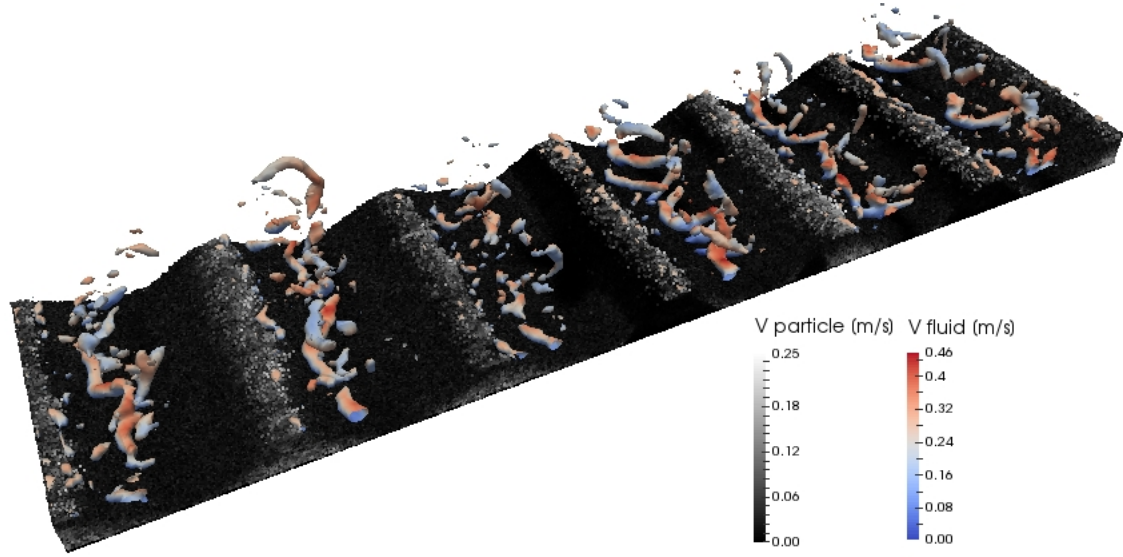


Figure 2.25: Numerical Q-criterion isocontours at phase time $\pi/4$. The fluid is accelerating from left to right.

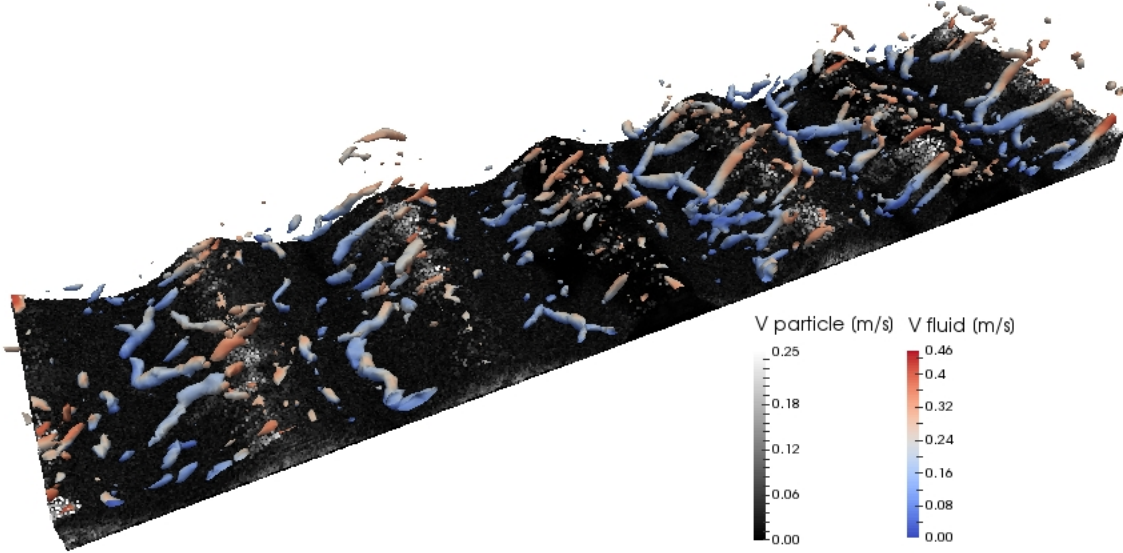


Figure 2.26: Numerical Q-criterion isocontours at phase time $\pi/2$. The fluid has achieved maximum free stream velocity, from left to right.

2.3.6 Fluid-Bed Interface

Determining the location of the fluid-bed interface is of utmost importance, not only in tracking the evolution of the bed morphology, but also in accurately calculating the bed shear stress, as in Section 2.3.4. In the ex-

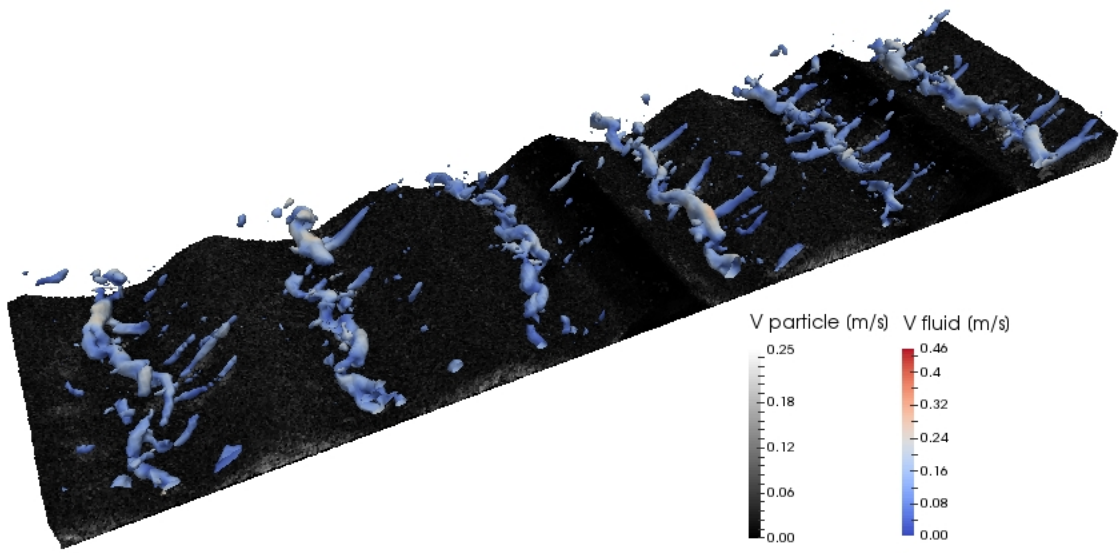


Figure 2.27: Numerical Q-criterion isocontours at phase time $3\pi/4$. The fluid is decelerating, but is still moving from left to right.

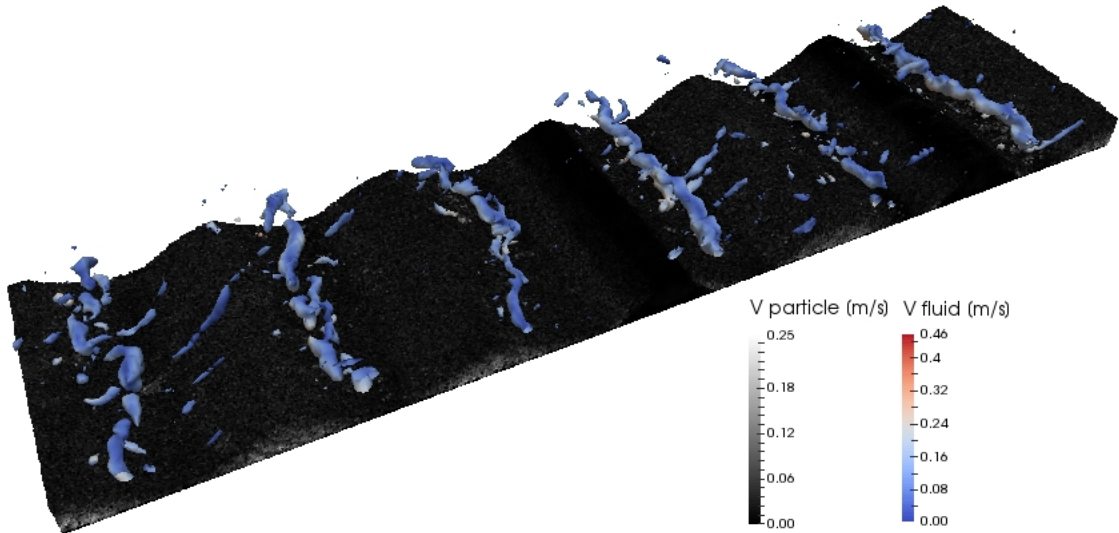


Figure 2.28: Numerical Q-criterion isocontours at phase time π . The freestream velocity has decelerated to zero, and is about to begin accelerating from right to left.

perimental data, this is easily done because the PIV data is zero in the bed and non-zero in the flow. However, in the numerical work, the interface is not so discrete. A couple different methods were tested, including di-

viding the domain into square bins of size d_p , then comparing all particles in each bin to determine where the bed ended, and where the fluid started. This meant defining a threshold, above which it was assumed all particles were not a part of the bed, but rather were entrained. However, this method proved unable to consistently provide an accurate interface location, as the definition of the threshold was problematic. Relying solely on particle velocity and/or angular velocity also proved unreliable, as a particle could momentarily be stationary, but still be entrained, or above the threshold, but still moving slowly. The best results were found using the approach of Kidanemariam and Uhlmann (2014). They defined a spanwise averaged two-dimensional solid volume fraction function, equivalent to $\langle(1 - \psi_f)\rangle$, defined now as $\langle\psi_p\rangle$. The authors defined the threshold at $\langle\psi_p\rangle_{threshold} = 0.1$, such that the two-dimensional interface is

$$h_b(x, t) = y, \quad \text{where } \langle\psi_p\rangle = \langle\psi_p\rangle_{threshold}. \quad (2.93)$$

Figure 2.29 shows the $\langle(1 - \psi_f)\rangle$ field and the fluid-bed interface at phase time $\pi/4$. Other methods that were abandoned would routinely report interfaces closer to $\langle\psi_p\rangle_{threshold} = 0.2$. As such, more particles were considered to above the fluid-bed interface, leading to spurious erosion statistics.

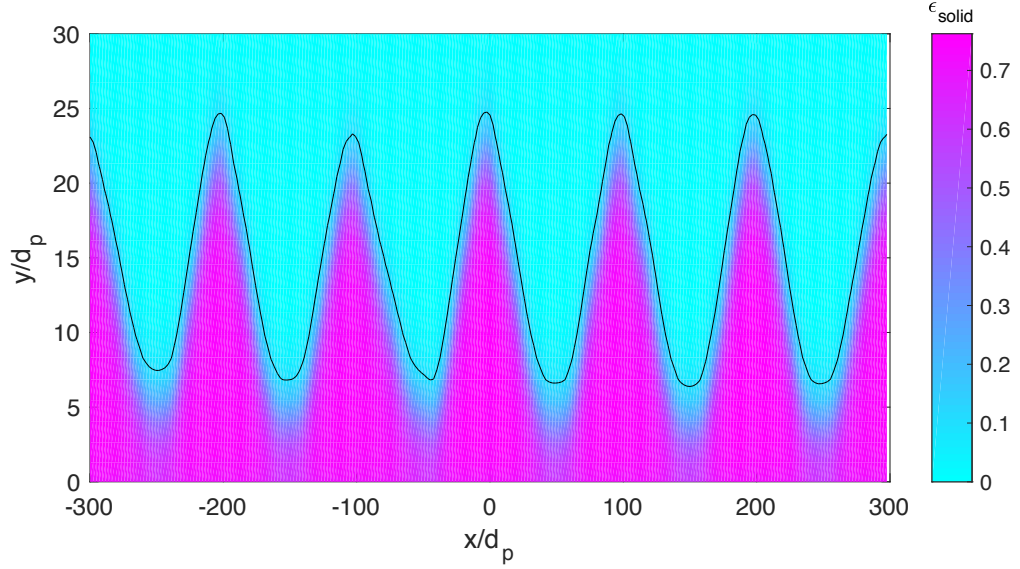


Figure 2.29: Numerical bed interface, as determined by assuming the bed has a solid volume fraction $\langle\psi_p\rangle = \langle\psi_p\rangle_{threshold}$. The data has been normalized by the particle diameter.

2.3.7 Ripple Shape Comparison

As discussed in Section 2.3.1, the numerical data has been spatially, ensemble, and phase-averaged to produce a two-dimensional data for a single canonical ripple. This applies to the fluid and solid phases of the LES. In the experimental work, the two-dimensional fluid data is phase-averaged over 11 periods. By contrast, the evolution of the fluid-bed interface was recorded for a single flow oscillation, so it is not averaged in any way. Therefore, the instantaneous experimental fluid-bed interface data, in conjunction with the fact that the initial numerical ripple shape is modeled as symmetric, when the experimental ripple is not, provide opportunity for discrepancy between the two data sets. Despite these potential issues, the numerical model does a good job predicting the evolution of the ripple shape. It should be noted that overall shape and wavelength of the ripples do not change on a macroscopic scale, thus they are quasi steady-state. The bulk of the ripple evolution is confined to the peaks. In Figure 2.30, the ripple shapes are shown over an entire flow oscillation period. At phase time 0, the ripples are skewed to the left of “center” of the ripple, defined at $x = 0$, with a sharper face angle on the left side than on the right. Once the flow is accelerated from left to right, the peak becomes more symmetric and more centered, as the particles at the peak are affected by the shear layer generated on the stoss side of the ripple. By phase times $\pi/2$ and $3\pi/4$, the peak has shifted to the right of center and now the sharper face angle is to the right of center, mirroring the morphology of phase time 0. At phase time π , the flow has decelerated back to a freestream velocity of zero, and the ripple shapes are retained. As the flow reverses, the same processes of the first half of the oscillation period are mirrored, until the initial ripple shape is recovered at phase time $7\pi/4$. Qualitatively, the numerical model is able to capture this phenomena.

In order to quantify the ability of the LES to predict the characteristics of the ripples, the locations of the ripple peak (maximum height) is compared in Figure 2.31. The phase time pairs that should mirror each other, because they are separated by half an oscillation period, mostly showed good agreement between the two data sets. At phase time 0, the both peaks are skewed to the left of center by nearly the same amount and have almost the same wall-normal location. At phase time $\pi/4$, the peak have both increased and shifted right, though the LES overpredicts by $3d_p$. By phase time $\pi/2$, the peaks have settled and are further shifted to the right. Until phase time $5\pi/4$, when the flow is accelerating in the opposite direction, the ripple peaks remain basically unchanged, moving by less than $0.25d_p$. As the flow reverses, again, the processes of the

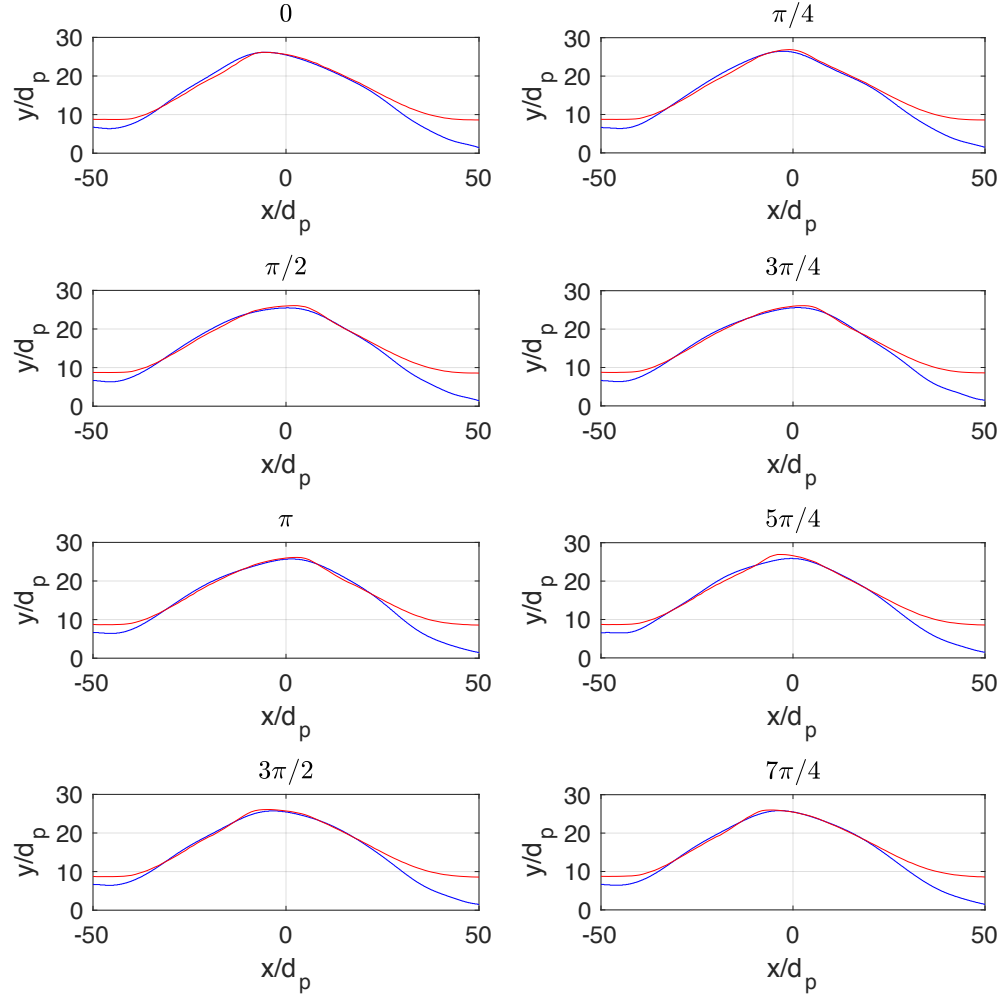


Figure 2.30: Experimental and numerical ripple comparison. The numerical ripple is space and phase-time averaged. The data has been normalized by the particle diameter. The blue line denotes experimental data, the red line denotes numerical data.

first half of the oscillation period are reversed. At its worst, the LES overpredicts the wall-normal location by only a single d_p (at phase time $5\pi/4$).

To quantify how well the LES predicts the actual shapes of the ripple peaks, the radius of curvature of the ripple at its peak is calculated. In order to do that, the least-square fitting of circles to the ripple peaks.

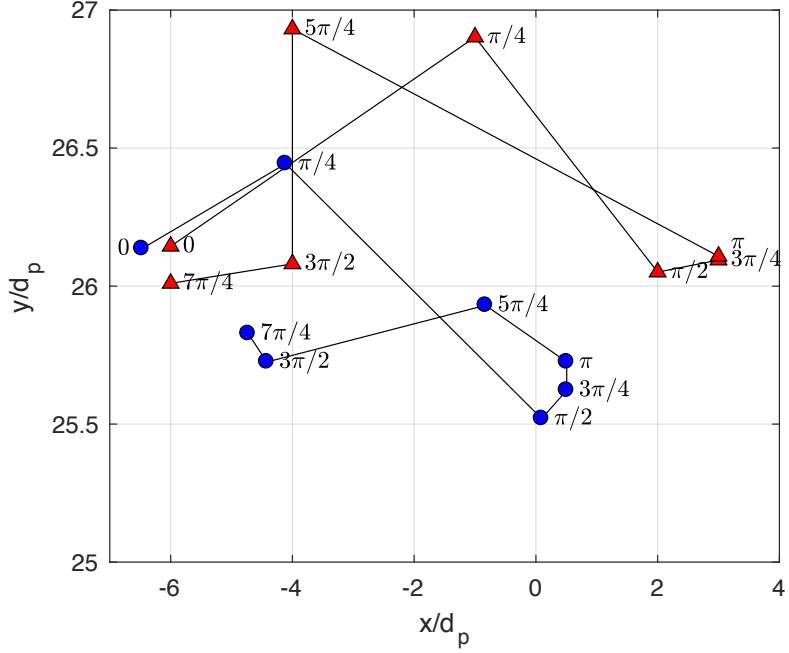


Figure 2.31: The locations of the ripple peaks are compared. The biggest discrepancy is seen at phase time $5\pi/4$, where the locations differ by roughly $3d_p$. The data has been normalized by the particle diameter. Blue circles denote the experimental data, and red triangles denote the numerical data.

In this case, three points were chosen to be fit. The center point is the ripple peak. One point to each side of the center point is chosen $5d_p$ distance away. Figure 2.32 show these best-fit circles over an oscillation period. Figure 2.33 plots the evolution of the radii of the best-fit circles over the oscillation period. The first half of the oscillation period, from phase time 0 until phase time π , show good agreement in the trends of the radii. However, the second half of the oscillation period does not mirror the first half, for either the experimental work or the LES. In the case of the experimental work, the ripples are not perfectly symmetric, so this result is not surprising. As far as the LES asymmetry is concerned, it most likely is attributable to the fact that system is not truly symmetric. Although the initial settle particle bed is symmetric, the system take three full oscillation periods before the bed shear stress converges. This builds some asymmetry into the bed morphology, and correspondingly, the flow as well.

Quantitatively, the DPM does a good job of predicting the overall shape and height of the experimentally measured ripple. Qualitatively, it is also able to capture the back-and-forth behavior of the ripple peak, as it is evolves under the force of the fluid.

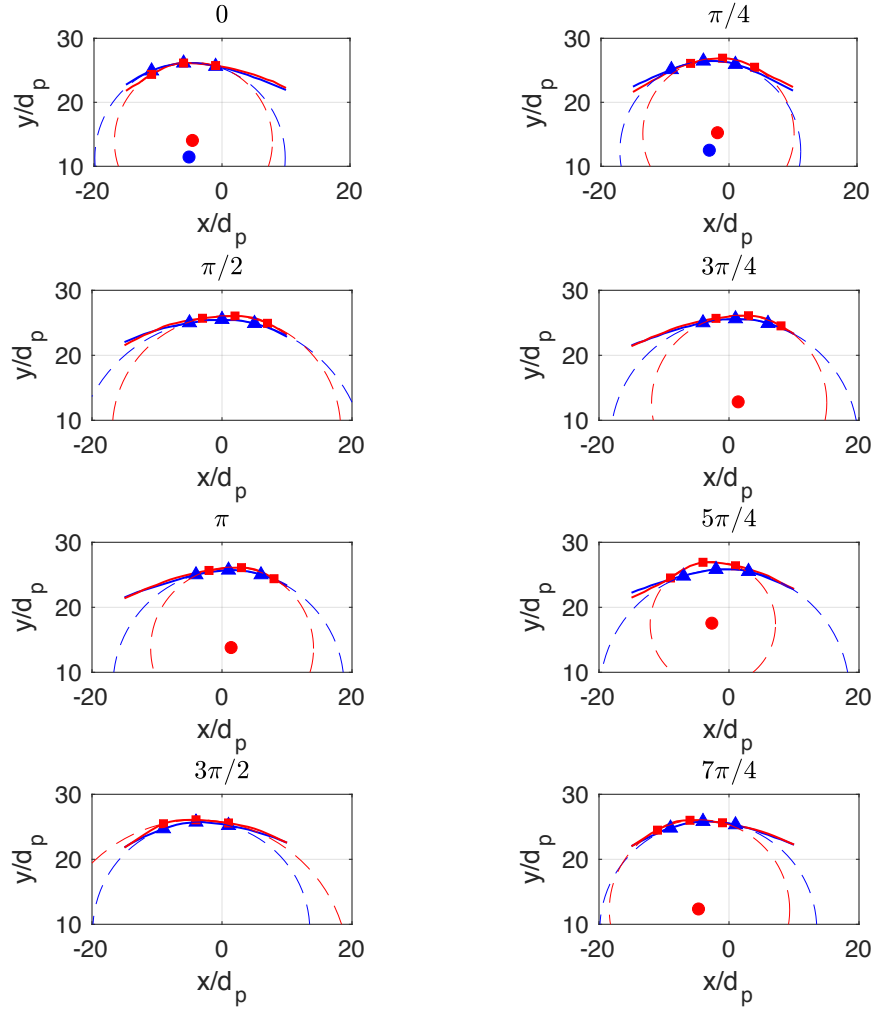


Figure 2.32: Best-fit circles are used to determine the radius of curvature of ripples at their peaks, shown at phase angles $\frac{n\pi}{4}$, for $n = 0, 1, \dots, 6, 7..$ The data has been normalized by the particle diameter. The blue line denotes experimental data, the red line denotes numerical data.

2.3.8 Characterization of Ripple Erosion

Using the definition of the fluid-bed interface from Section 2.3.6, all particles that are above the interface are defined as eroded. The eroded particles that are within a single d_p of the interface are classified as reptating, or sliding and/or rolling, at the surface. The eroded particles that are greater than one d_p distance from the

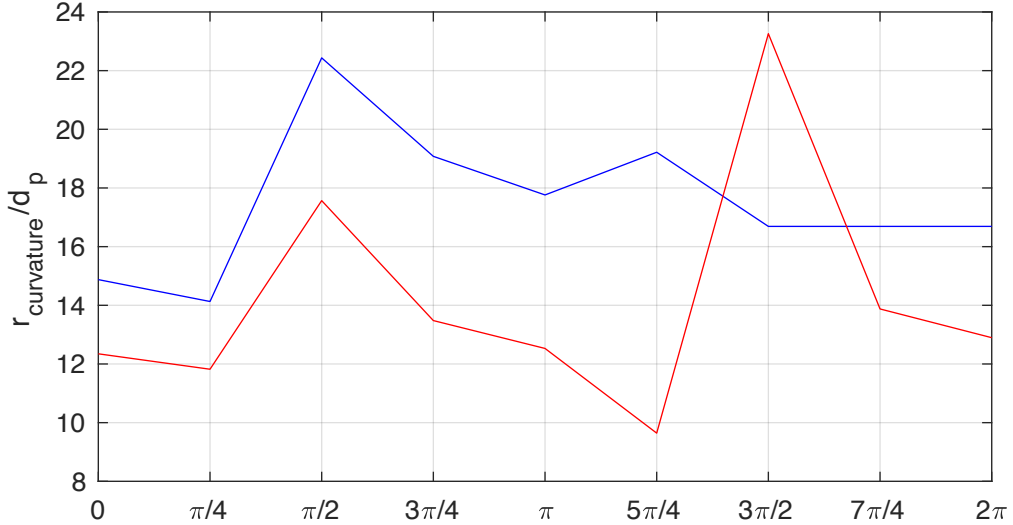


Figure 2.33: The evolution of the best-fit circles, used to determine the radius of curvature of ripples at their peaks, are shown over a whole period. The data has been normalized by the particle diameter. The blue line denotes experimental data, the red line denotes numerical data. The first half period shows good qualitative agreement between the radii of curvature. However, the second half does not.

interface are defined as saltating, or lifted from, and redeposited to, the bed on a short timescale. Figure 2.34 shows the interface and both reptating and saltating particles at phase time $\pi/4$, which is the time at which the fluid undergoes maximum acceleration from left to right. The shear layer imparts momentum to the particles at the top of the ripple crests and they undergo saltation from the peak to the lee side of the peak. The reverse process is observed at phase $5\pi/4$. Just as the ripple interface evolves essentially at the peak, the eroded particles are also located at the peak. The eroded particle velocities, plotted at their streamwise locations, are shown in Figure 2.35. Here, the difficulty in characterizing the erosion of the particle bed is observed. There is no obvious difference between the velocities of particles undergoing reptation and those undergoing saltation. And in fact, the distributions of the particle velocities, shown in Figure 2.36, are quite similar. When the fluid is experiencing the maximum acceleration, at phase times $\pi/4$ and $5\pi/4$, both classifications of eroded particles show similarly shaped distributions. However, the reptating particles distribution seems to be centered around $U_p/U_\infty \simeq 0.5 - 0.8$, while the saltating distribution is centered around $U_p/U_\infty \simeq 0.7 - 1.0$. The distribution centers at other phase times are also slightly higher for the saltation process.

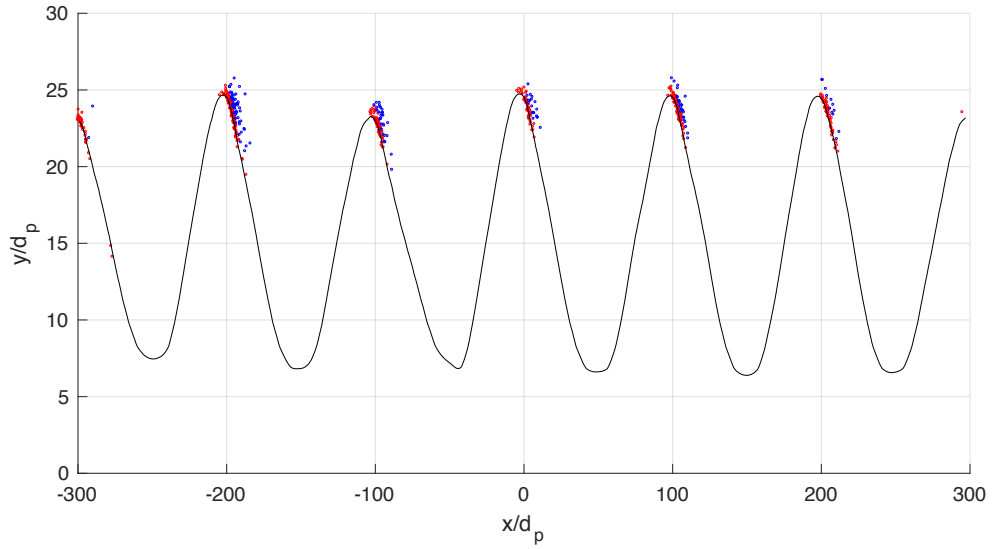


Figure 2.34: Numerical bed interface and the particles that have been eroded by the flow, at phase angle $\pi/4$. Reptating, or sliding and/or rolling, particles are red. Particles that are saltating, or momentarily entrained before returning to the bed, are blue. The data has been normalized by the particle diameter.

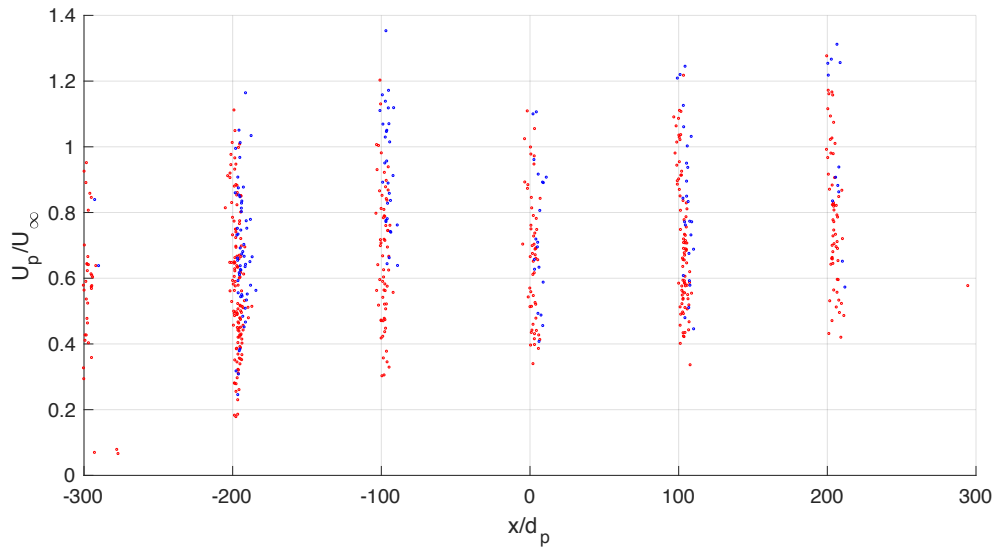


Figure 2.35: Saltating and reptating particle velocities, at phase angle $\pi/4$. The particle velocities are normalized by the maximum freestream velocity, and the particle positions are normalized by the particle diameter. Red denotes reptation, and blue denotes saltation.

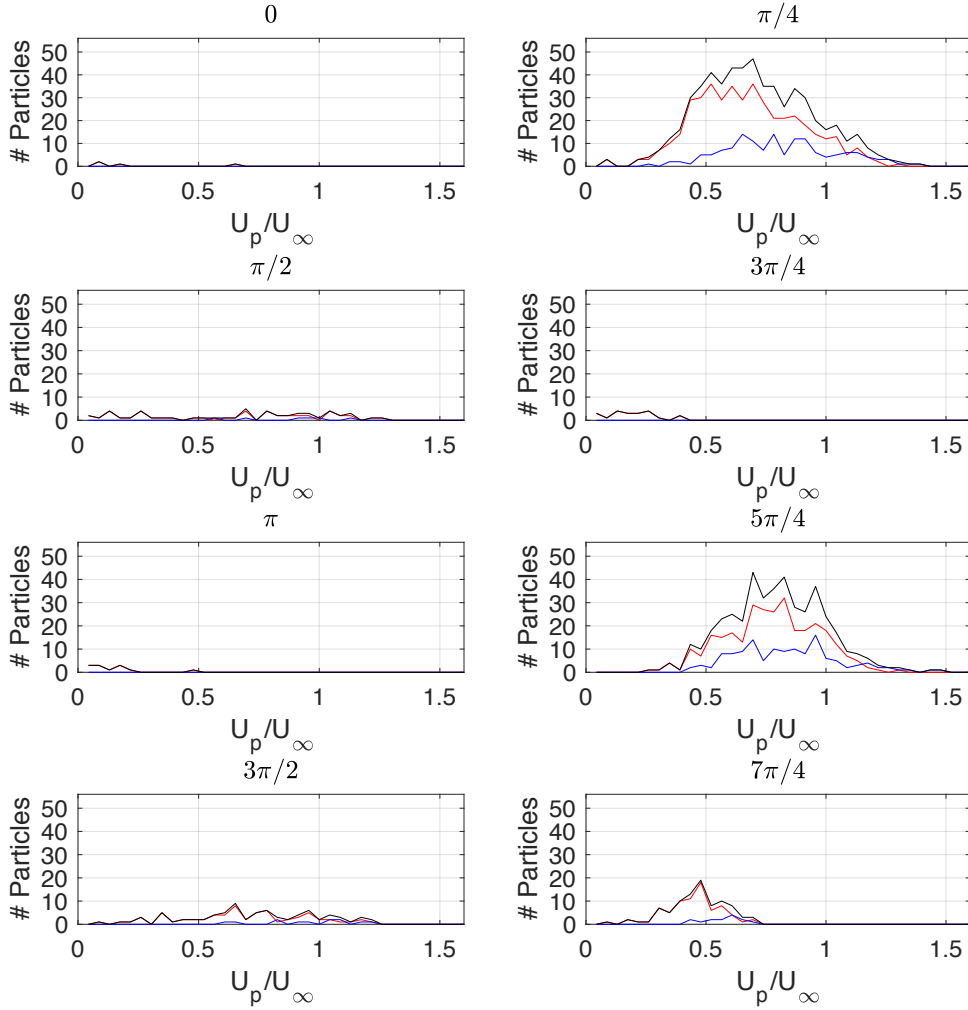


Figure 2.36: Velocity distributions, shown at phase angles $\frac{n\pi}{4}$, for $n = 0, 1, \dots, 6, 7$. The red line denotes reptating particles, the blue line denotes saltating particles, and the black line denotes all eroded particles (reptating plus saltating particles). The particle velocities are normalized by the maximum freestream velocity.

The angular velocities of the eroded particles are plotted at their streamwise locations in Figure 2.37. As Figure 2.38 show, there is no discernable difference. At phase times $\pi/4$ and $5\pi/4$, when the fluid is experiencing the maximum acceleration, the distributions are extremely similar, with medians around $\omega_{median} \simeq 60 rad/s$, with maximums around $\omega_{median} \simeq 100 rad/s$.

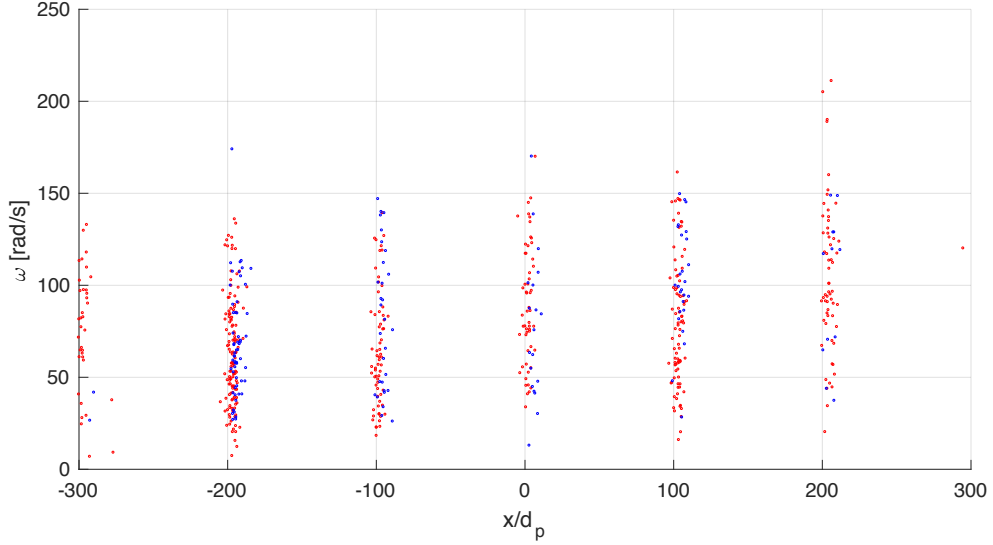


Figure 2.37: Saltating and reptating particle angular velocities, at phase angle $\pi/4$. The particle positions are normalized by the particle diameter. Red denotes reptation, and blue denotes saltation.

The Shields parameter, Θ of the eroded particles are shown in Figure 2.39. As defined in Section 2.2, the Shields parameter is the ratio of disturbing fluid force to the restorative gravitational force. So high values of Θ are indicative of erosive processes, and low values of Θ indicate stability. For both reptation and saltation, there is a distinct asymmetry in the phases $\pi/4$ and $5\pi/4$, at which the bulk of the erosion occurs. This is likely due to the asymmetry of the ripples themselves. Since the peaks are slightly skewed to the left of center, the faces at the peaks display slightly sharper crests than when skewed to right. Therefore, a higher percentage of eroded particles display higher Θ values when moving from left to right, than right to left. Thus, the distribution peaks at phase time $5\pi/4$ are lower than at phase time $\pi/4$.

2.3.9 Potential Sources of Error

Limitations in both the numerical model and the experimental data collection contribute to discrepancies between the two results. In building the numerical model, both the core methodology and simulation configuration make assumptions that potentially result in deviation from the experimental findings. By definition, the LES-DPM approach used in this work is not of the absolute highest fidelity, as the LES flow solver explicitly models the smallest unresolved features of the flow. Additionally, the DPM does not fully resolve

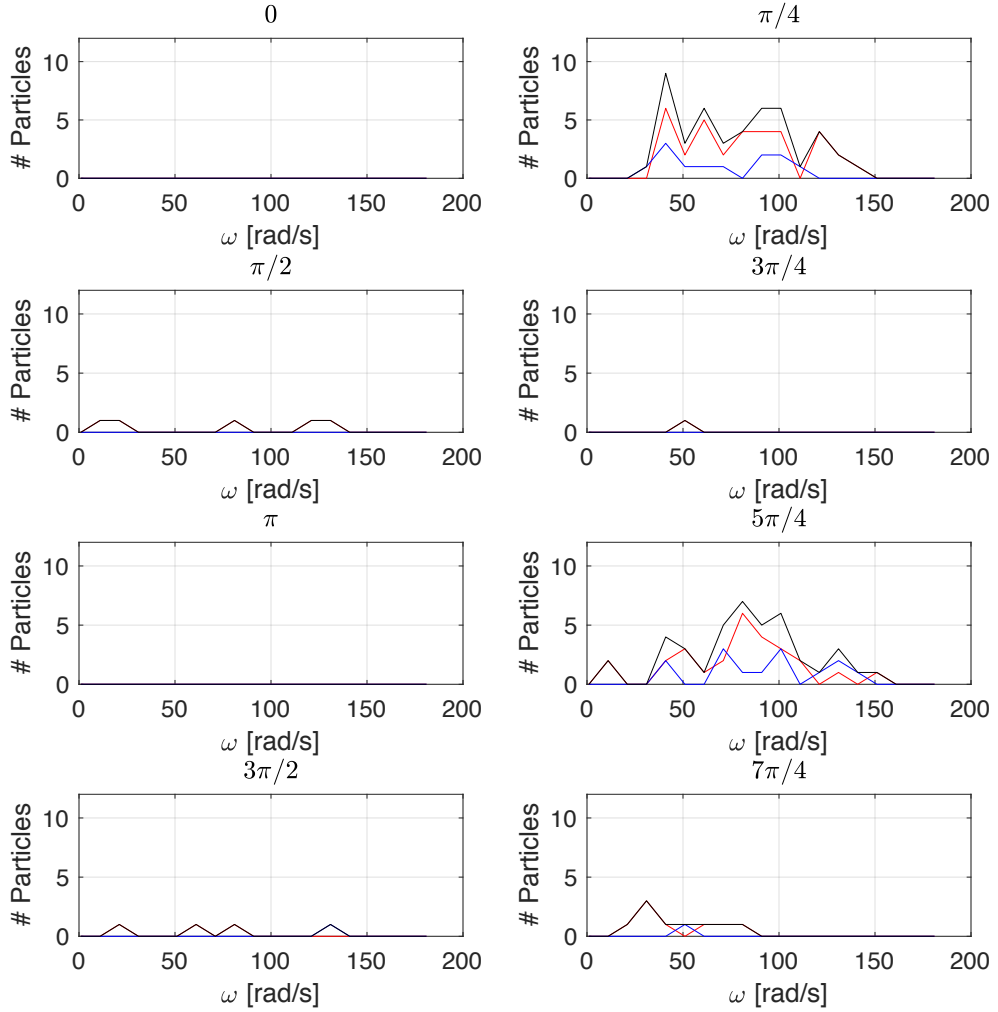


Figure 2.38: Particle angular velocity distributions, shown at phase angles $\frac{n\pi}{4}$, for $n = 0, 1, \dots, 6, 7$. The red line denotes reptating particles, the blue line denotes saltating particles, and the black line denotes all eroded particles (reptating plus saltating particles).

particles with a no-slip boundary condition at each individual particle, but, rather, by volume-averaging the Navier-Stokes equations to account for the effect of the particles. Therefore, although both the flow solver and solid phase solver do a good job of predicting the mesoscale features of the system, higher fidelity meth-

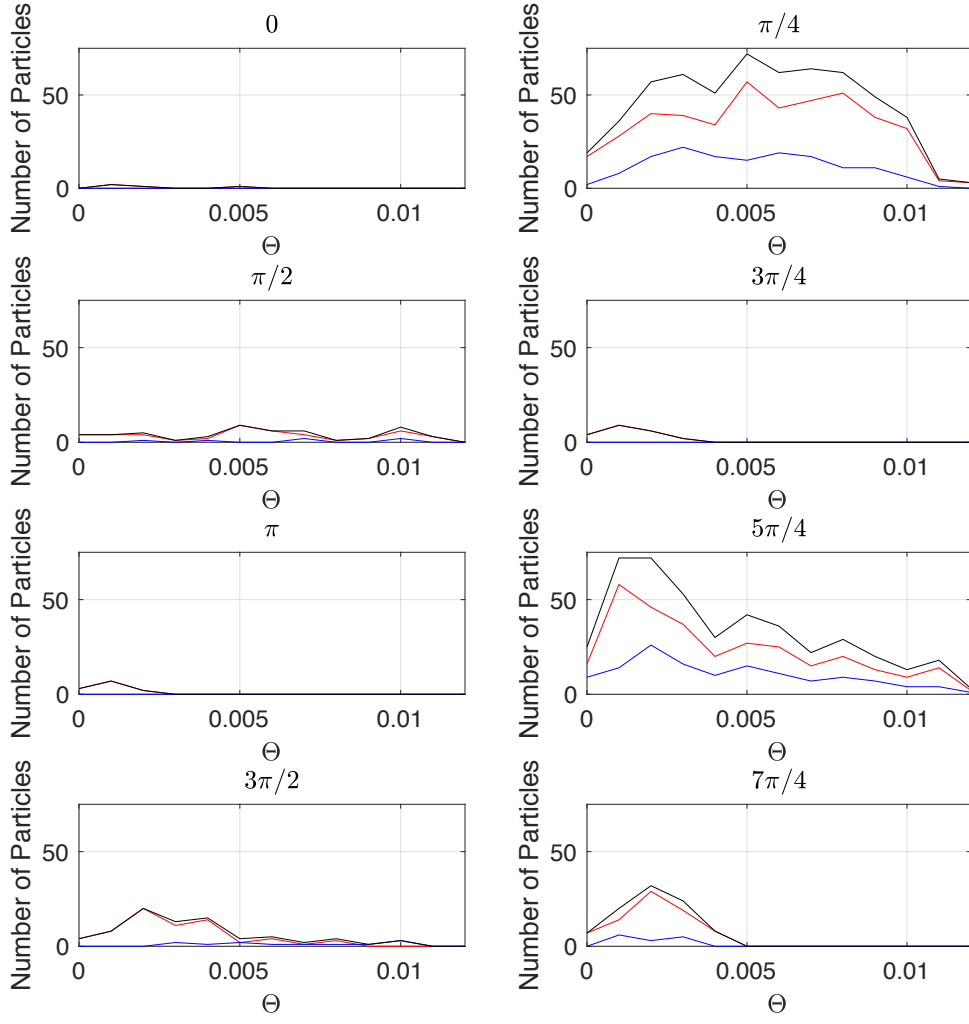


Figure 2.39: Shields parameter distributions, shown at phase angles $\frac{n\pi}{4}$, for $n = 0, 1, \dots, 6, 7$. The red line denotes reptating particles, the blue line denotes saltating particles, and the black line is the all eroded particles (reptating plus saltating particles).

ods would potentially provide more accurate results. Unfortunately, at the moment, such computationally expensive methods are not feasible for this particular flow configuration.

Due to the complex morphology of the experimental ripple shape, only an approximation was used in the numerical work. The two troughs of the experimental ripple are of different depths and the peak itself

is not perfectly symmetric. However, the overall shape of the ripple, in particular the top half and crest, are well approximated by a sinusoidal curve. And, although the initial settled particle bed is truly symmetric, the system takes three full oscillation periods before the bed shear stress converges. Of course, the flow must start in one direction, and because of this, some asymmetry is built into the bed morphology, and correspondingly, the flow as well. So the numerical bed, while not fully replicating the experimental ripple shape, does have some minor asymmetry due to the convergence of the system. Despite these discrepancies, the numerical model does a good job predicting the qualitative evolution of the ripple peak orientation and predicting the quantitative ripple height evolution. Nonetheless, without exactly replicating the experimental ripple shape, there will always be discrepancies between the experiment and the numerical simulation that is modeling it.

As with any experimental work, there are limitations in the collection of data. The experiment conducted at the Sediment Dynamics Laboratory of the Naval Research Laboratory, in Stennis Space Center, MS, is fantastic because it starts from a initially flat bed of sand, and the ripples are formed naturally, which was not computationally feasible with the numerical model. Due to the shear size of PIV data, the experiment was allowed to run until quasi steady-state ripples had formed, then data was collected for eleven cycles. By definition, PIV flow data is two-dimensional. Therefore, the data provides insight into the nature of the flow, but cannot provide an instantaneous three-dimensional perspective. In the same way the flow data is two-dimensional, the bed-fluid interface is also two-dimensional, but was recorded instantaneously for a single flow oscillation. So, it is conceivable that there are fluctuations of the ripple shape were not captured.

So although the limitations of the numerical model and limitations of the experimental data collection could combine to produce divergent results, in fact, the model does a good job of predicting the flow and ripple characteristics of the experimental data.

2.4 Conclusion

This work investigates the evolution of a sinusoidally rippled particle bed under the effect of an oscillatory flow. A Large-Eddy Simulation (LES) was conducted to mimic the conditions of an experiment conducted in the small-oscillatory flow tunnel at the Sediment Dynamics Laboratory of the Naval Research Laboratory, Stennis Space Center, MS. The simulation uses the Discrete Particle Method (DPM), which is an Euler-Lagrange approach, where particles and fluid are four-way coupled.

In the experimental work, a closed channel of water, over an initially flat sand bed, is driven to oscillatory flow. Eventually, the system reaches a quasi-equilibrium in which spanwise oriented ripples have formed in the sand bed. The ripples are roughly sinusoidal in shape, with a wavelength roughly five times the amplitude. Stereographic PIV data captured fluid velocity in a two-dimensional plane around a single ripple for eleven oscillation periods. The LES was configured to reproduce the configuration of this steady-state in the oscillatory flow channel by prescribing a sinusoidal ripple morphology and driving the flow by a cosinusoidal pressure gradient. The three-dimensional domain contains six ripples and the fluid was initially at rest. The flow is then driven by the cosinusoidal pressure gradient and the system requires three full periods for the bed shear stress to converge. In both the experimental work and the LES, as the flow accelerates, a shear layer forms at the stoss side of the ripple. As the flow achieves its maximum freestream velocity and begins to decelerate, the shear layer forms a spanwise vortex which detaches from the ripple peak on the lee side. When the flow has decelerated back to zero in the freestream, the halfway point of the oscillation period, this vortex is detached between ripples. As the flow is accelerated in the opposite direction, this detached vortex is shed into the freestream as another shear layer is formed at the ripple peak, and the whole process is mirrored in the second half of the oscillation period.

This work shows the viability of the LES-DPM methodology to predict the phenomena of ripple evolution in quasi-steady-state oscillatory flow conditions. Based on wall-normal profiles of velocity and the turbulent kinetic energy budget, along with velocity streamlines and vorticity, the LES proves capable of capturing the mesoscale features of the experimental flow. Additionally, the DPM is able to predict the evolution of the experimental ripple morphology and provide insight into the erosive processes at the individual particle scale.

The DPM has been shown to be a valid tool to investigate the interaction between flow dynamics and particles, and has provided some potential insights regarding the understanding of bed shear stress over mobile beds, and the interaction between vortices shed from the ripples. These will be the subject of future work.

Chapter 3

Ongoing Work & Plan for Publications

3.0.1 Viability of LES-DPM for this Flow Configuration

This work shows the viability of the LES-DPM methodology to predict the phenomena of ripple evolution in quasi-steady-state oscillatory flow conditions. Based on wall-normal profiles of velocity and the turbulent kinetic energy budget, along with velocity streamlines and vorticity, the LES proves capable of capturing the mesoscale features of the experimental flow. Additionally, the DPM is able to predict the evolution of the experimental ripple morphology and provide insight into the erosive processes at the individual particle scale. This material is the subject of a paper which will be submitted to an appropriate peer-reviewed journal at the beginning of 2018.

3.0.2 Ongoing Work: Bed Shear Stress

As described in Section 2.3.4, the classical approach to defining bed shear stress is based on the assumption that bed-fluid interface is a rigid, no-slip boundary. In fact, when individual particles are resolved and tracked in a Lagrangian framework, this is not the case. As the flow imparts momentum to the particles at the surface of the bed, the particles can become entrained in the fluid for short (saltation), or long (fluidization), periods of time. At lower fluid velocities, the particles may slide or creep (reptation), over the surrounding particles. However, it is also observed that at specific fluid velocities, the particles may move (usually in packets, or as a small group) slightly, but ultimately do not move from their original locations. In these cases, the definition

of the bed-fluid interface is nebulous and subject to interpretation. Merely defining the bed to be made up of those particles which have zero velocity does not result in accurate descriptions of the interface. Instead, the interface is defined to include those particles that may move or sway in place, but do not ultimately change position. In doing so, there may actually be velocities of particles and fluid within the bed itself. In order to flesh out this idea, a short note-style paper focusing on this idea will be submitted to an appropriate journal.

3.0.3 Ongoing Work: Helical Vortex Pairing

The LES-DPM simulations in this work revealed an unusual phenomenon in which vortex pairs become intertwined in a helical fashion. This helical pairing instability was first observed experimentally by Nygaard and Glezer (1990) in a shear layer, and later confirmed by Comte et al. (1992) in a Direct Numerical Simulation. As expected, quasi two-dimensional Kelvin-Helmholtz spanwise sheets develop at the shear layer interface, and roll-up into vortical structures. Due to unstable oblique modes, these rolled-up sheets combine at only certain locations in the spanwise direction. The result is the three-dimensional lattice of intertwined vortices shown in Figure 3.1.

This phenomenon is not known to have been previously observed in an oscillatory flow. However, since this work presents an oscillatory flow over a rippled bed, the flow dynamics are significantly different. As the flow reverses directions and begins to accelerate, a shear layer is formed at the upstream side and crest of the ripple. This shear layer develops into a vortex which is shed on the downstream side of the ripple. As this mechanism repeats itself in the opposite direction, the original shed vortex interacts with the newly developing shear layer, and creates a pairing. This pairing displays the spanwise instabilities and helical structure observed by Nygaard and Glezer (1990) and Comte et al. (1992). Figures 3.2, 3.3, and 3.4 show this helical pairing stability.

The goal of the work presented in this section is to show that the helical pairing instability is not isolated to shear layers, but can also be observed in an oscillatory flow over a rippled bed. As of this writing, the author is not aware of the observation of this phenomenon in any flow configuration other than a shear layer. Therefore, a short note-type paper will be formulated to demonstrate this observation.

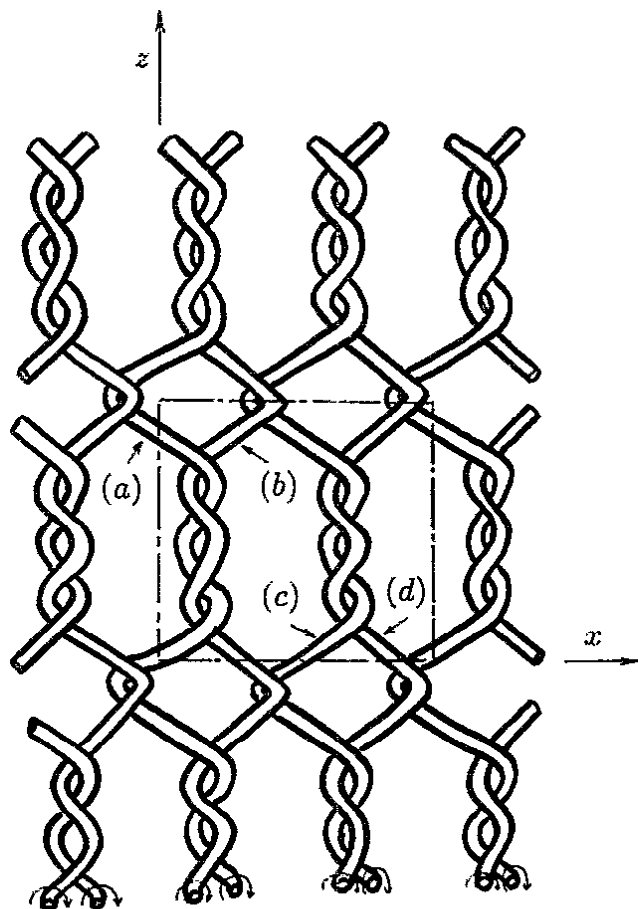


Figure 3.1: Schematic of intertwining vortices in a shear layer, per the work of Comte et al. (1992).

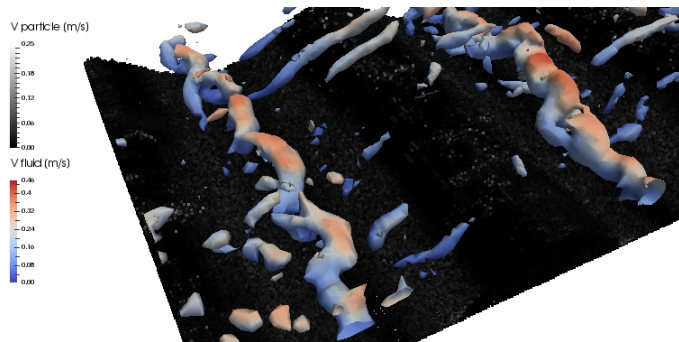


Figure 3.2: Helical pairing of vortices at phase time $\frac{8\pi}{12}$. One vortex is shed from the ripple, and as the flow reverses, the newly formed shear layer develops into a second vortex, which interacts with the existing vortex and the two become entwined.

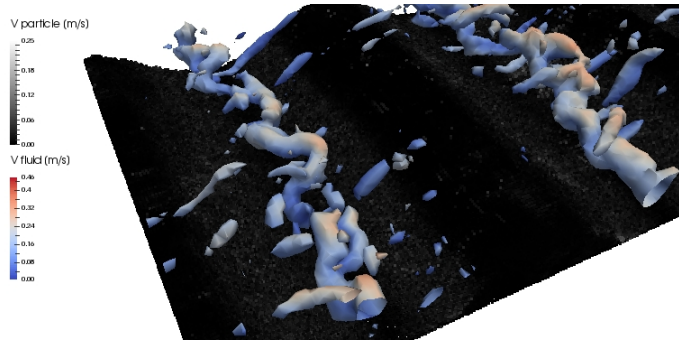


Figure 3.3: Helical pairing of vortices at phase time $\frac{9\pi}{12}$. One vortex is shed from the ripple, and as the flow reverses, the newly formed shear layer develops into a second vortex, which interacts with the existing vortex and the two become entwined.

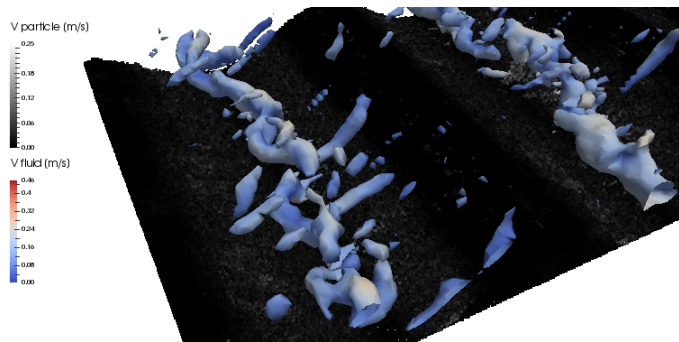


Figure 3.4: Helical pairing of vortices at phase time $\frac{10\pi}{12}$. One vortex is shed from the ripple, and as the flow reverses, the newly formed shear layer develops into a second vortex, which interacts with the existing vortex and the two become entwined.

3.0.4 Ongoing Work: Integral Method Analysis

In collaboration with a group at the University of New Hampshire, an Integral Method Analysis is being used to determine the physical contributions of wall shear stress in the flow presented in this work. This approach is valid for two-dimensional, wall-bounded, incompressible flow. Following the work of Fukagata et al. (2002), Mehdi et al. (2011) (2014), and Ebadi et al. (2015), the RANS momentum equation is triple integrated in the wall-normal direction, to eventually yield an equation for the wall shear stress,

$$\tau_w = \underbrace{\frac{2\mu}{y_t^2} \int_0^{y_t} U dy}_I - \underbrace{\frac{2\rho}{y_t^2} \int_0^{y_t} (y_t - y) \bar{u'}v' dy}_II - \underbrace{\frac{\rho}{y_t^2} \int_0^{y_t} (y_t - y)^2 \frac{\partial}{\partial y} \left[\nu \frac{\partial U}{\partial y} - \bar{u'}v' \right] dy}_III. \quad (3.1)$$

This equation yields direct connections between the fluxes at the wall and the dynamics of the flow. The first term, I , is the laminar contribution from the mean flow. The second term, II , is the turbulent contribution. And, the third term, III , is the inhomogeneous/transient contribution. The details of the derivation can be found in the Appendix B.1.

Since the Integral Method Analysis breaks down the wall shear stress into components that represent different physical aspects of the flow, it allows for better analysis by identifying the physics at play. Because the particles are resolved by volume-filtering the Navier-Stokes equations in the LES-DPM, the fluid velocity at the fluid-bed interface is available and should provide the insight required to demonstrate the viability of the Integral Method for non-smooth walls.

In addition to the application of the Integral Method Analysis to the oscillatory flow presented in this work, it will also be applied to a second unidirectional flow. The domain and the rippled particle bed remain the same as in this work, but rather a oscillatory pressure gradient to drive the flow, a constant unidirectional pressure gradient is used to maintain a constant Re_b flow over the ripples. Meagan Wengrove is the principal investigator of this Integral Method Analysis, and her plan is to submit the work to a relevant peer-reviewed journal in the Spring of 2018.

3.0.5 Plan for Publications

In order to solidfy this work in the literature, three first-author papers will be submitted by the Spring of 2018. The subjects, and scope, are as follows:

- 1) The material presented in the body of this dissertation, and summarized in Section 3.0.1, will be the subject of a standard length paper, which will be submitted to an appropriate fluid or geological hydraulics specific journal;
- 2) The ongoing work, in Section 3.0.2 regarding the ambiguity of bed-fluid interfaces and the effect on bed shear stress calculations will be the subject of a short note-style paper. This will also be submitted to an appropriate fluid or geological hydraulics specific journal; and,
- 3) The ongoing work, in Section 3.0.3, regarding the helical pairing instability observed in the shed vortices of the flow will be submitted to a fluid/turbulence related journal.

Finally, a fourth paper will be co-authored, with collaborator Meagan Wengrove of UNH as first-author:

- 4) This paper will focus on the Integral Method Analysis presented in Section 3.0.4.

3.0.6 Future Work

There are many future studies possible with the application of the LES-DPM, as presented in this work. The most obvious would be a study of the development of particle bed ripples by oscillatory flow. Arolla et al. (2015) have already demonstrated the capability of this code, NGA, to develop ripples by a unidirectional pipe flow over a bed. Secondly, the NGA code is also capable of Direct Numerical Simulations (DNS), where, with an appropriately refined grid, all scales of the flow can be directly calculated. To conduct the same study presented in this work, but with a much refined grid, as a DNS, would provide a direct comparison of the LES capability. Of course, as with all DNS, computational cost is the primary concern. In the LES presented here, the wall-normal grid is refined to roughly $\Delta y_{min} \simeq 10$ wall units. In order to properly configure a DNS for this simulation configuration, roughly thirty to forty times as many wall-normal grid points would be needed, which would require the 128 points of the LES to become over 700 points in the DNS, with at least 600 points needed in the particle bed alone.

Bibliography

- Akhavan, R., R. Kamm, and A. Shapiro (1991). An investigation of transition to turbulence in bounded oscillatory stokes flows part 2. numerical simulations. *Journal of fluid mechanics* 225, 423–444.
- Arolla, S. K. and O. Desjardins (2015). Transport modeling of sedimenting particles in a turbulent pipe flow using euler–lagrange large eddy simulation. *International Journal of Multiphase Flow* 75, 1–11.
- Bagnold, R. A. and G. Taylor (1946). Motion of waves in shallow water. interaction between waves and sand bottoms. In *Proceedings of the Royal Society of London A: Mathematical, Physical and Engineering Sciences*, Volume 187, pp. 1–18. The Royal Society.
- Benjamin, T. B. (1959). Shearing flow over a wavy boundary. *Journal of Fluid Mechanics* 6(2), 161–205.
- Best, J. (2005). The fluid dynamics of river dunes: A review and some future research directions. *Journal of Geophysical Research: Earth Surface* 110(F4).
- Blondeaux, P. (1990). Sand ripples under sea waves part 1. ripple formation. *Journal of Fluid Mechanics* 218, 1–17.
- Blondeaux, P. and G. Vittori (1991). Vorticity dynamics in an oscillatory flow over a rippled bed. *Journal of Fluid Mechanics* 226, 257–289.
- Briaud, J.-L., F. C. Ting, H. Chen, R. Gudavalli, S. Perugu, and G. Wei (1999). Sricos: Prediction of scour rate in cohesive soils at bridge piers. *Journal of Geotechnical and Geoenvironmental Engineering* 125(4), 237–246.
- Brørs, B. (1999). Numerical modeling of flow and scour at pipelines. *Journal of Hydraulic Engineering* 125(5), 511–523.
- Capecelatro, J. and O. Desjardins (2013a). An euler–lagrange strategy for simulating particle-laden flows. *Journal of Computational Physics* 238, 1–31.
- Capecelatro, J. and O. Desjardins (2013b). An euler–lagrange strategy for simulating particle-laden flows. *Journal of Computational Physics* 238, 1–31.
- Capecelatro, J. and O. Desjardins (2013c). Eulerian–lagrangian modeling of turbulent liquid–solid slurries in horizontal pipes. *International journal of multiphase flow* 55, 64–79.
- Charru, F., B. Andreotti, and P. Claudin (2013). Sand ripples and dunes. *Annual Review of Fluid Mechanics* 45, 469–493.
- CHARRU, F. and E. Hinch (2006a). Ripple formation on a particle bed sheared by a viscous liquid. part 1. steady flow. *Journal of Fluid Mechanics* 550, 111–121.
- CHARRU, F. and E. Hinch (2006b). Ripple formation on a particle bed sheared by a viscous liquid. part 2. oscillating flow. *Journal of Fluid Mechanics* 550, 123–137.
- Chen, D., C. Chen, F.-E. Tang, P. Stansby, and M. Li (2007). Boundary layer structure of oscillatory open-channel shallow flows over smooth and rough beds. *Experiments in Fluids* 42(5), 719–736.
- Chiew, Y.-M. (1990). Mechanics of local scour around submarine pipelines. *Journal of Hydraulic Engineering* 116(4), 515–529.
- Chong, M. S., A. E. Perry, and B. J. Cantwell (1990). A general classification of three-dimensional flow fields. *Physics of Fluids A: Fluid Dynamics* 2(5), 765–777.
- Chou, Y.-J. and O. B. Fringer (2010). A model for the simulation of coupled flow-bed form evolution in turbulent flows. *Journal of Geophysical Research: Oceans (1978–2012)* 115(C10).
- Church, M. (2006). Bed material transport and the morphology of alluvial river channels. *Annu. Rev. Earth Planet. Sci.* 34, 325–354.

- Coleman, S. and V. Nikora (2009). Bed and flow dynamics leading to sediment-wave initiation. *Water Resources Research* 45(4).
- Coleman, S. E., J. J. Fedele, and M. H. Garcia (2003). Closed-conduit bed-form initiation and development. *Journal of Hydraulic Engineering* 129(12), 956–965.
- Comte, P., M. Lesieur, and E. Lamballais (1992). Large-and small-scale stirring of vorticity and a passive scalar in a 3-d temporal mixing layer. *Physics of Fluids A: Fluid Dynamics* 4(12), 2761–2778.
- Corvaro, S., M. Miozzi, M. Postacchini, A. Mancinelli, and M. Brocchini (2014). Fluid-particle interaction and generation of coherent structures over permeable beds: an experimental analysis. *Advances in Water Resources* 72, 97–109.
- Cundall, P. A. and O. D. Strack (1979). A discrete numerical model for granular assemblies. *Geotechnique* 29(1), 47–65.
- Deen, N., M. Van Sint Annaland, M. Van der Hoef, and J. Kuipers (2007). Review of discrete particle modeling of fluidized beds. *Chemical Engineering Science* 62(1), 28–44.
- Derkzen, J. J. (2015). Simulations of granular bed erosion due to a mildly turbulent shear flow. *Journal of Hydraulic Research* 53(5), 622–632.
- Desjardins, O., G. Blanquart, G. Balarac, and H. Pitsch (2008). High order conservative finite difference scheme for variable density low mach number turbulent flows. *Journal of Computational Physics* 227(15), 7125–7159.
- Di Liberto, M. and M. Ciofalo (2009). Numerical simulation of reciprocating turbulent flow in a plane channel. *Physics of fluids* 21(9), 095106.
- Ding, L. and Q.-H. Zhang (2011). Lattice boltzmann simulation to characterize roughness effects of oscillatory boundary layer flow over a rough bed. *Coastal Engineering Proceedings* 1(32), 3.
- Dixen, M., F. Hatipoglu, B. M. Sumer, and J. Fredsøe (2008). Wave boundary layer over a stone-covered bed. *Coastal Engineering* 55(1), 1–20.
- Durán, O., B. Andreotti, and P. Claudin (2012). Numerical simulation of turbulent sediment transport, from bed load to saltation. *Physics of Fluids* 24(10), 103306.
- Ebadi, A., F. Mehdi, and C. M. White (2015). An exact integral method to evaluate wall heat flux in spatially developing two-dimensional wall-bounded flows. *International Journal of Heat and Mass Transfer* 84, 856–861.
- Engelund, F. and J. Fredsøe (1982). Sediment ripples and dunes. *Annual Review of Fluid Mechanics* 14(1), 13–37.
- Florez, J. E. C. and E. de Moraes Franklin (2016). The formation and migration of sand ripples in closed conduits: experiments with turbulent water flows. *Experimental Thermal and Fluid Science* 71, 95–102.
- Fornarelli, F. and G. Vittori (2009). Oscillatory boundary layer close to a rough wall. *European Journal of Mechanics-B/Fluids* 28(2), 283–295.
- Frank, D., D. Foster, P. Chou, Y.-M. Kao, I. M. Sou, and J. Calantoni (2014). Development and evaluation of an autonomous sensor for the observation of sediment motion. *Journal of Atmospheric and Oceanic Technology* 31(4), 1012–1019.
- Frank, D., D. Foster, I. M. Sou, and J. Calantoni (2015). Incipient motion of surf zone sediments. *Journal of Geophysical Research: Oceans* 120(8), 5710–5734.
- Frank, D., D. Foster, I. M. Sou, J. Calantoni, and P. Chou (2015). Lagrangian measurements of incipient motion in oscillatory flows. *Journal of Geophysical Research: Oceans* 120(1), 244–256.

- Frank, E. and F. Jørgen (1976). A sediment transport model for straight alluvial channels. *Nordic Hydrology* 7(5), 293–306.
- Fröhlich, J., C. P. Mellen, W. Rodi, L. Temmerman, and M. A. Leschziner (2005). Highly resolved large-eddy simulation of separated flow in a channel with streamwise periodic constrictions. *Journal of Fluid Mechanics* 526, 19–66.
- Fukagata, K., K. Iwamoto, and N. Kasagi (2002). Contribution of reynolds stress distribution to the skin friction in wall-bounded flows. *Physics of Fluids* 14(11), L73–L76.
- Germano, M., U. Piomelli, P. Moin, and W. H. Cabot (1991). A dynamic subgrid-scale eddy viscosity model. *Physics of Fluids A: Fluid Dynamics* 3(7), 1760–1765.
- Ghodke, C. D. and S. V. Apte (2016). Dns study of particle-bed–turbulence interactions in an oscillatory wall-bounded flow. *Journal of Fluid Mechanics* 792, 232–251.
- Grigoriadis, D., E. Balaras, and A. Dimas (2009). Large-eddy simulations of unidirectional water flow over dunes. *Journal of Geophysical Research: Earth Surface* 114(F2).
- Gundogdu, M. Y. and M. O. Carpinlioglu (1999a). Present state of art on pulsatile flow theory: Part 1: Laminar and transitional flow regimes. *JSME International Journal Series B Fluids and Thermal Engineering* 42(3), 384–397.
- Gundogdu, M. Y. and M. O. Carpinlioglu (1999b). Present state of art on pulsatile flow theory: Part 2: Turbulent flow regime. *JSME International Journal Series B Fluids and Thermal Engineering* 42(3), 398–410.
- Hino, M., M. Kashiwayanagi, A. Nakayama, and T. Hara (1983). Experiments on the turbulence statistics and the structure of a reciprocating oscillatory flow. *Journal of Fluid Mechanics* 131, 363–400.
- Hino, M., M. Sawamoto, and S. Takasu (1976). Experiments on transition to turbulence in an oscillatory pipe flow. *Journal of Fluid Mechanics* 75(2), 193–207.
- Hogg, A. J., H. E. Huppert, and W. B. Dade (1997). Erosion by planar turbulent wall jets. *Journal of Fluid Mechanics* 338, 317–340.
- Hsu, C.-T., X. Lu, and M.-K. Kwan (2000). Les and rans studies of oscillating flows over flat plate. *Journal of engineering mechanics* 126(2), 186–193.
- Jensen, B., B. Sumer, and J. Fredsøe (1989). Turbulent oscillatory boundary layers at high reynolds numbers. *Journal of Fluid Mechanics* 206, 265–297.
- Kaneko, A. and H. Honji (1979). Double structures of steady streaming in the oscillatory viscous flow over a wavy wall. *Journal of Fluid Mechanics* 93(4), 727–736.
- Kennedy, J. F. (1963). The mechanics of dunes and antidunes in erodible-bed channels. *Journal of Fluid Mechanics* 16(4), 521–544.
- Khosronejad, A. and F. Sotiropoulos (2014). Numerical simulation of sand waves in a turbulent open channel flow. *Journal of Fluid Mechanics* 753, 150–216.
- Kidanemariam, A. G. and M. Uhlmann (2014). Direct numerical simulation of pattern formation in subaqueous sediment. *Journal of Fluid Mechanics* 750.
- Kidanemariam, A. G. and M. Uhlmann (2017). Formation of sediment patterns in channel flow: minimal unstable systems and their temporal evolution. *Journal of Fluid Mechanics* 818, 716–743.
- Kirca, V. O., B. M. Sumer, M. Steffensen, K. L. Jensen, and D. R. Fuhrman (2016). Longitudinal dispersion of heavy particles in an oscillating tunnel and application to wave boundary layers. *Journal of Ocean Engineering and Marine Energy* 2(1), 59–83.

- Kuru, W., D. Leighton, and M. McCready (1995). Formation of waves on a horizontal erodible bed of particles. *International journal of multiphase flow* 21(6), 1123–1140.
- Landau, L. D. and E. M. Lifshits (1959). *Fluid mechanics, by LD Landau and EM Lifshitz*. Pergamon Press.
- Levine, Y. and A. Polimeno (2007). A dissipative particle dynamics study of the realignment of a nanodroplet of a nematic in a weak external magnetic field. *The European Physical Journal E* 23(1), 13.
- Li, F. and L. Cheng (1999). Numerical model for local scour under offshore pipelines. *Journal of Hydraulic Engineering* 125(4), 400–406.
- Liang, D., L. Cheng, and F. Li (2005). Numerical modeling of flow and scour below a pipeline in currents: Part ii. scour simulation. *Coastal engineering* 52(1), 43–62.
- Lilly, D. K. (1992). A proposed modification of the germano subgrid-scale closure method. *Physics of Fluids A: Fluid Dynamics* 4(3), 633–635.
- Liu, X. and M. H. García (2008). Three-dimensional numerical model with free water surface and mesh deformation for local sediment scour. *Journal of waterway, port, coastal, and ocean engineering* 134(4), 203–217.
- Loudon, C. and A. Tordesillas (1998). The use of the dimensionless womersley number to characterize the unsteady nature of internal flow. *Journal of theoretical biology* 191(1), 63–78.
- Maurin, R., J. Chauchat, B. Chareyre, and P. Frey (2015). A minimal coupled fluid-discrete element model for bedload transport. *Physics of Fluids* 27(11), 113302.
- Mazzuoli, M., A. G. Kidanemariam, P. Blondeaux, G. Vittori, and M. Uhlmann (2016). On the formation of sediment chains in an oscillatory boundary layer. *Journal of Fluid Mechanics* 789, 461–480.
- Mehdi, F., T. G. Johansson, C. M. White, and J. W. Naughton (2014). On determining wall shear stress in spatially developing two-dimensional wall-bounded flows. *Experiments in fluids* 55(1), 1656.
- Mehdi, F. and C. M. White (2011). Integral form of the skin friction coefficient suitable for experimental data. *Experiments in Fluids* 50(1), 43–51.
- Meneveau, C., T. S. Lund, and W. H. Cabot (1996). A lagrangian dynamic subgrid-scale model of turbulence. *Journal of Fluid Mechanics* 319, 353–385.
- Meyer-Peter, E. and R. Müller (1948). Formulas for bed-load transport. In *Proceedings of the 2nd Meeting of the International Association for Hydraulic Structures Research*, pp. 39–64. Stockholm.
- Mutlu Sumer, B. (2007). Mathematical modelling of scour: A review. *Journal of Hydraulic Research* 45(6), 723–735.
- Nakagawa, H. and T. Tsujimoto (1984). Spectral analysis of sand bed instability. *Journal of Hydraulic Engineering* 110(4), 467–483.
- Nik Hassan, N. and R. Narayanan (1985). Local scour downstream of an apron. *Journal of Hydraulic Engineering* 111(11), 1371–1384.
- Nygaard, K. J. and A. Glezer (1990). Core instability of the spanwise vortices in a plane mixing layer. *Physics of Fluids A: Fluid Dynamics* 2(3), 461–464.
- Olsen, N. R. and H. M. Kjellesvig (1998). Three-dimensional numerical flow modeling for estimation of maximum local scour depth. *Journal of Hydraulic Research* 36(4), 579–590.
- Olsen, N. R. and M. C. Melaaen (1993). Three-dimensional calculation of scour around cylinders. *Journal of Hydraulic Engineering* 119(9), 1048–1054.
- Omidyeganeh, M. and U. Piomelli (2011). Large-eddy simulation of two-dimensional dunes in a steady, unidirectional flow. *Journal of Turbulence* (12), N42.

- Paola, C. and V. Voller (2005a). A generalized exner equation for sediment mass balance. *Journal of Geophysical Research: Earth Surface (2003–2012)* 110(F4).
- Paola, C. and V. Voller (2005b). A generalized exner equation for sediment mass balance. *Journal of Geophysical Research: Earth Surface* 110(F4).
- Pepiot, P. and O. Desjardins (2012). Numerical analysis of the dynamics of two-and three-dimensional fluidized bed reactors using an euler-lagrange approach. *Powder Technology* 220, 104–121.
- Pond, I., A. Ebadi, Y. Dubief, and C. M. White (2017). An integral validation technique of rans turbulence models. *Computers & Fluids* 149, 150–159.
- Richards, K. J. (1980). The formation of ripples and dunes on an erodible bed. *Journal of Fluid Mechanics* 99(3), 597–618.
- Roulund, A., B. M. Sumer, J. Fredsøe, and J. Michelsen (2005). Numerical and experimental investigation of flow and scour around a circular pile. *Journal of Fluid Mechanics* 534, 351–401.
- Schiller, L. and A. Naumann (1933). Fundamental calculations in gravitational processing. *Zeitschrift Des Vereines Deutscher Ingenieure* 77, 318–320.
- Schmeeckle, M. W. (2014). Numerical simulation of turbulence and sediment transport of medium sand. *Journal of Geophysical Research: Earth Surface* 119(6), 1240–1262.
- Scotti, A. and U. Piomelli (2001). Numerical simulation of pulsating turbulent channel flow. *Physics of Fluids* 13(5), 1367–1384.
- Sleath, J. (1976). On rolling-grain ripples. *Journal of Hydraulic Research* 14(1), 69–81.
- Sleath, J. (1987). Turbulent oscillatory flow over rough beds. *Journal of Fluid Mechanics* 182, 369–409.
- Sleath, J. F. (1984). Sea bed mechanics.
- Smagorinsky, J. (1963). General circulation experiments with the primitive equations: I. the basic experiment. *Monthly weather review* 91(3), 99–164.
- Spalart, P. R. and B. S. Baldwin (1989). Direct simulation of a turbulent oscillating boundary layer. In *Turbulent shear flows 6*, pp. 417–440. Springer.
- Stoesser, T., C. Braun, M. Garcia-Villalba, and W. Rodi (2008). Turbulence structures in flow over two-dimensional dunes. *Journal of Hydraulic Engineering* 134(1), 42–55.
- Sumer, B. M. and M. Bakioglu (1984). On the formation of ripples on an erodible bed. *Journal of Fluid Mechanics* 144, 177–190.
- Sun, R. and H. Xiao (2016). Cfd–dem simulations of current-induced dune formation and morphological evolution. *Advances in Water Resources* 92, 228–239.
- Tao, J. and X. Yu (2013). A framework for numerical simulation of bridge scour focusing on the improvements of sediment transport models. In *Transportation Research Board 92nd Annual Meeting*, Number 13-2852.
- Tenneti, S., R. Garg, and S. Subramaniam (2011). Drag law for monodisperse gas–solid systems using particle-resolved direct numerical simulation of flow past fixed assemblies of spheres. *International journal of multiphase flow* 37(9), 1072–1092.
- Thomas, D. G. (1964). Periodic phenomena observed with spherical particles in horizontal pipes. *Science* 144(3618), 534–536.
- Van Rijn, L. C. (1984). Sediment transport, part i: bed load transport. *Journal of hydraulic engineering* 110(10), 1431–1456.

- van Rijn, L. C. (1987). *Mathematical modelling of morphological processes in the case of suspended sediment transport*. Ph. D. thesis, Waterloopkundig Lab., Delft Hydraulics Comm-382.
- Vittori, G. and P. Blondeaux (1990). Sand ripples under sea waves part 2. finite-amplitude development. *Journal of Fluid Mechanics* 218, 19–39.
- Vittori, G. and R. Verzicco (1998). Direct simulation of transition in an oscillatory boundary layer. *Journal of Fluid Mechanics* 371, 207–232.
- Yakhot, A., M. Arad, and G. Ben-Dor (1999). Numerical investigation of a laminar pulsating flow in a rectangular duct. *International journal for numerical methods in fluids* 29(8), 935–950.
- Yalin, M. S. (1977). *Mechanics of Sediment Transport: 2d Ed.* Pergamon Press.
- Yue, W., C.-L. Lin, and V. C. Patel (2005). Large eddy simulation of turbulent open-channel flow with free surface simulated by level set method. *Physics of fluids* 17(2), 025108.
- Zamankhan, P. (2009). Analysis of submarine pipeline scour using large-eddy simulation of dense particle-liquid flows. *Journal of offshore mechanics and Arctic engineering* 131(2).
- Zedler, E. A. and R. L. Street (2001). Large-eddy simulation of sediment transport: currents over ripples. *Journal of Hydraulic Engineering* 127(6), 444–452.
- Zhu, H., Z. Zhou, R. Yang, and A. Yu (2007). Discrete particle simulation of particulate systems: theoretical developments. *Chemical Engineering Science* 62(13), 3378–3396.
- Zhu, H., Z. Zhou, R. Yang, and A. Yu (2008). Discrete particle simulation of particulate systems: A review of major applications and findings. *Chemical Engineering Science* 63(23), 5728–5770.

Appendix A: Additional Wall-Normal Statistics

A.1 Wall-Normal Locations of Maximum Streamwise Velocities

The wall-normal locations of the maximum of averaged freestream velocity profiles are compared in Figure A.1. As expected, wall-normal locations are consistent at phase times separated by a half oscillation period, since the numerical ripple is more strongly symmetric than that in the experiment. The maximums at phase time 0 and π are nearly identical for the numerical work, and differ by roughly a single particle diameter in the experimental data. In the numerical work, the max streamwise velocity location for the phase time pairs $\pi/4 - 5\pi/4$ and $\pi/2 - 3\pi/2$ are also nearly identical. The pair $3\pi/4 - 7\pi/4$ shows a discrepancy of roughly two particle diameters. In all cases, the numerical data shows very similar maximum freestream velocity magnitudes for phase time pairs. The experimental data displays slight discrepancies, ranging from one to four particle diameters, for phase time pairs separated by a half oscillation period. This is likely a result of the asymmetry of the experimental ripple. The magnitudes of maximum freestream velocities, however, do show a strong symmetry for phase time pairs.

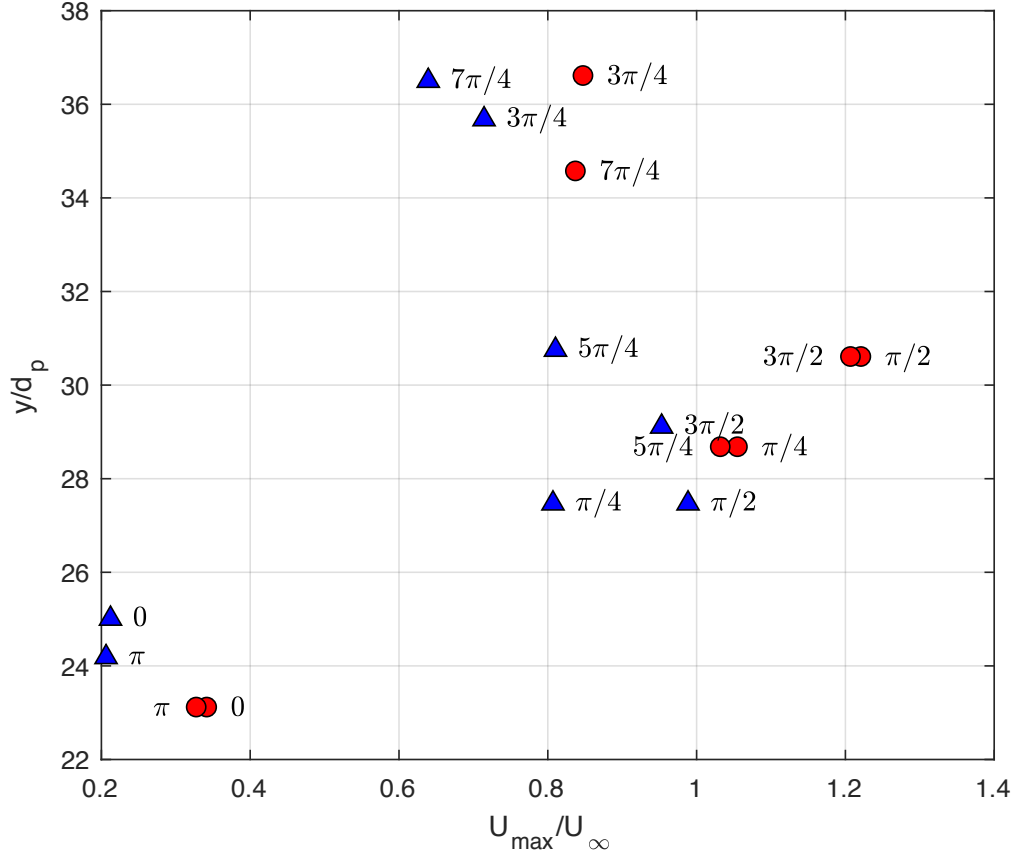


Figure A.1: Maximum velocities of streamwise profiles, averaged over the entire wavelength of the ripple, shown at phase angles $\frac{n\pi}{4}$, for $n = 0, 1, \dots, 6, 7$. The velocities are normalized by the maximum achieved freestream streamwise velocity, U_∞ . The wall-normal position is normalized by the particle diameter. The experimental data is denoted by blue triangles, and the numerical results by red circles.

A.2 Wall-Normal TKE Profiles at Different Locations on Ripple

Figures A.2, A.3, and A.4 show the wall-normal TKE profiles, normalized by the square of the maximum freestream velocity, at the ripple crest, trough and face, respectively. Much like the velocity profiles, the TKE profiles are best predicted by the numerical model at the crest and face, while there is greater deviation from the experimental profiles at the ripple trough.

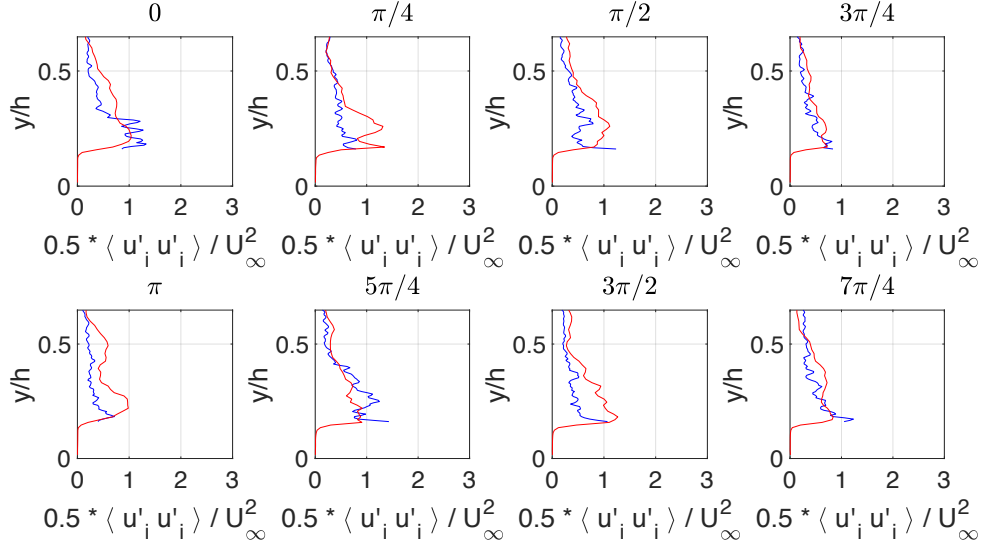


Figure A.2: Turbulent kinetic energy (TKE) wall-normal profiles, at the ripple crest, shown at phase angles $\frac{n\pi}{4}$, for $n = 0, 1, \dots, 6, 7$. The TKE is normalized by the square of the maximum achieved freestream streamwise velocity, U_∞ . The wall-normal position is normalized by the half-height of the channel, h . The experimental results are denoted by a red line, and the numerical results by a blue line. In some cases, the range of the PIV data was limited, therefore, the entire profile was not available.

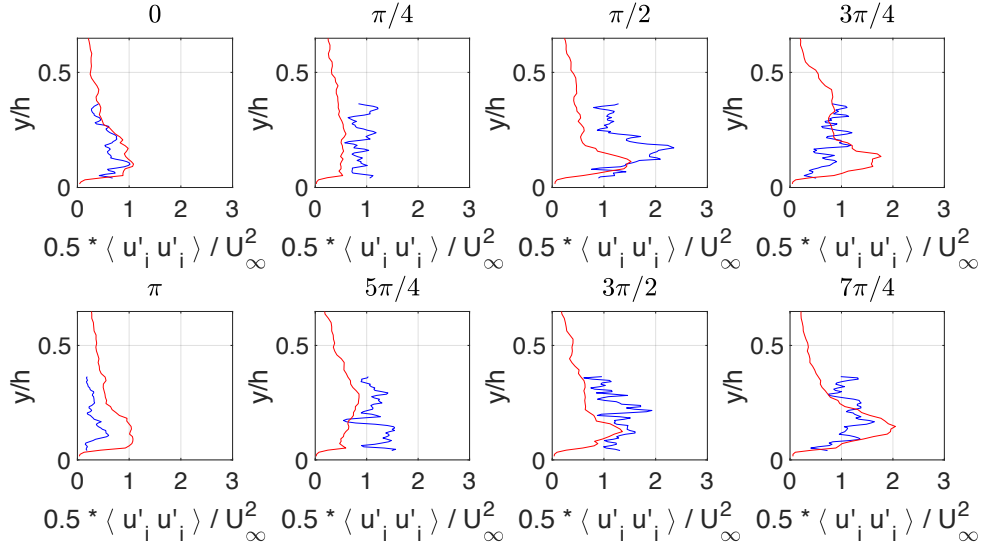


Figure A.3: Turbulent kinetic energy (TKE) wall-normal profiles, at the ripple trough, shown at phase angles $\frac{n\pi}{4}$, for $n = 0, 1, \dots, 6, 7$. The TKE is normalized by the square of the maximum achieved freestream streamwise velocity, U_∞ . The wall-normal position is normalized by the half-height of the channel, h . The experimental results are denoted by a red line, and the numerical results by a blue line. In some cases, the range of the PIV data was limited, therefore, the entire profile was not available.

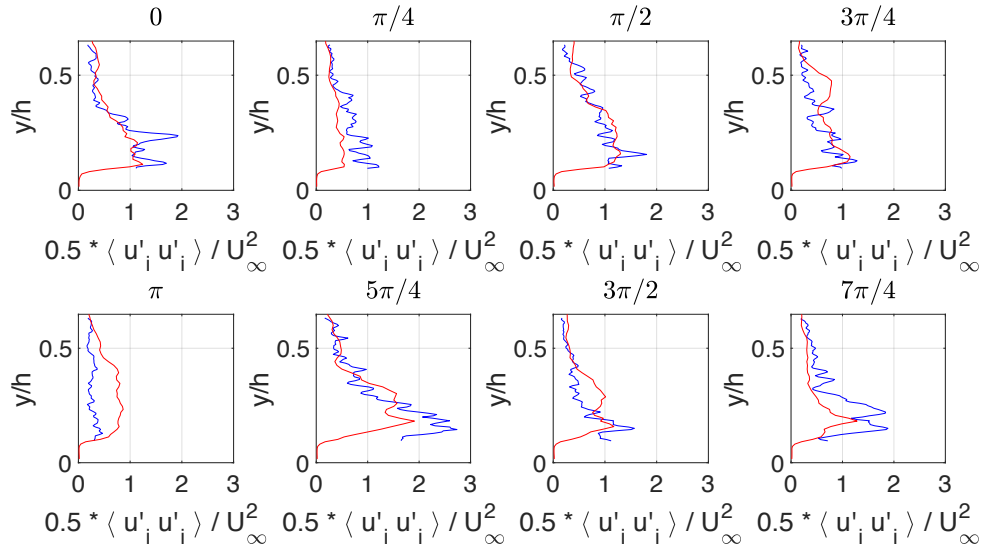


Figure A.4: Turbulent kinetic energy (TKE) wall-normal profiles, at the ripple face, shown at phase angles $\frac{n\pi}{4}$, for $n = 0, 1, \dots, 6, 7$. The TKE is normalized by the square of the maximum achieved freestream streamwise velocity, U_∞ . The wall-normal position is normalized by the half-height of the channel, h . The experimental results are denoted by a red line, and the numerical results by a blue line. In some cases, the range of the PIV data was limited, therefore, the entire profile was not available.

A.3 Wall-Normal Reynolds Stress Profiles at Different Locations on Ripple

Figures A.5, A.6, and A.7 show the wall-normal Reynolds shear stress profiles at the ripple crest, trough, and face. Here, again, the numerical model does the best predictions at the ripple crest, while the profiles at the trough and face show some gross over-predictions, even if the trends are mostly predicted qualitatively.

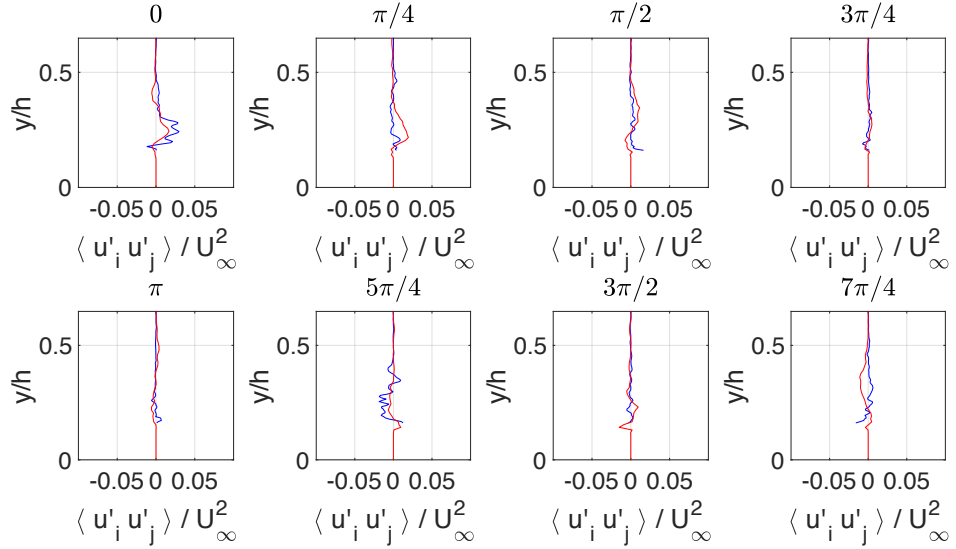


Figure A.5: Reynolds stress wall-normal profiles, at the ripple crest, shown at phase angles $\frac{n\pi}{4}$, for $n = 0, 1, \dots, 6, 7$. The Reynolds stress is normalized by the square of the maximum achieved freestream streamwise velocity, U_∞ . The wall-normal position is normalized by the half-height of the channel, h . The experimental results are denoted by a blue line, and the numerical results by a red line. In some cases, the range of the PIV data was limited, therefore, the entire profile was not available.

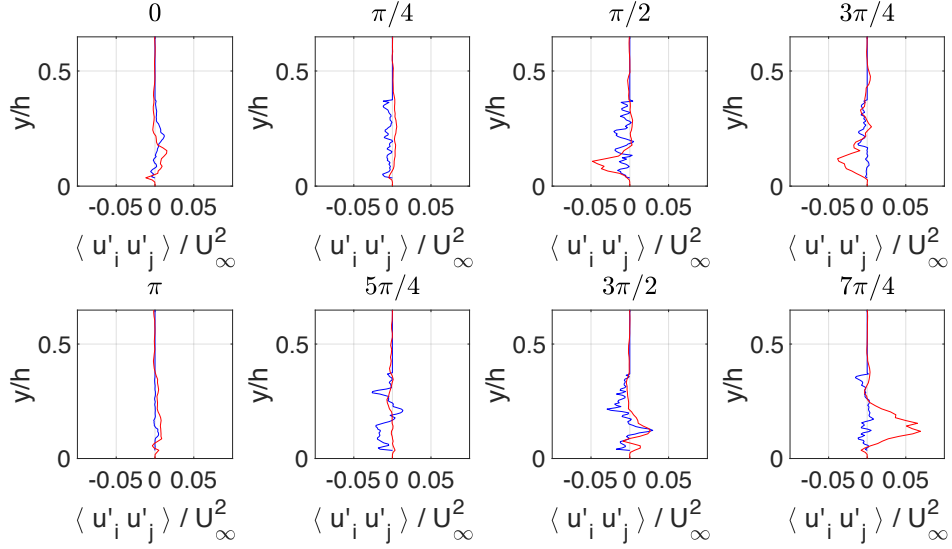


Figure A.6: Reynolds stress wall-normal profiles, at the ripple trough, shown at phase angles $\frac{n\pi}{4}$, for $n = 0, 1, \dots, 6, 7$. The Reynolds stress is normalized by the square of the maximum achieved freestream streamwise velocity, U_∞ . The wall-normal position is normalized by the half-height of the channel, h . The experimental results are denoted by a blue line, and the numerical results by a red line. In some cases, the range of the PIV data was limited, therefore, the entire profile was not available.

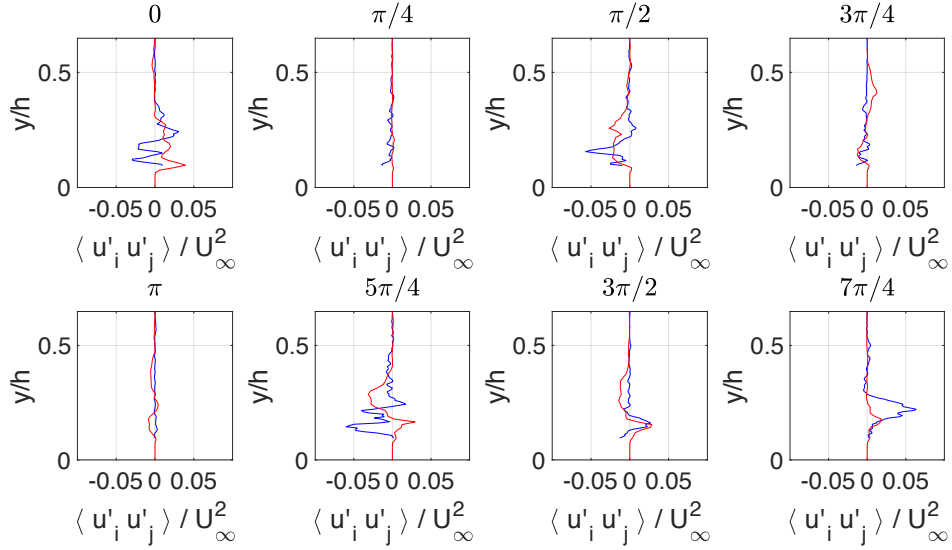


Figure A.7: Reynolds stress wall-normal profiles, at the ripple face, shown at phase angles $\frac{n\pi}{4}$, for $n = 0, 1, \dots, 6, 7$. The Reynolds stress is normalized by the square of the maximum achieved freestream streamwise velocity, U_∞ . The wall-normal position is normalized by the half-height of the channel, h . The experimental results are denoted by a blue line, and the numerical results by a red line. In some cases, the range of the PIV data was limited, therefore, the entire profile was not available.

A.4 Wall-Normal Profiles of Reynolds stresses (Wall-Normal, Streamwise, Spanwise) at Different Locations on Ripple

The final quantities utilized to quantify the deviation in velocity fluctuations from the mean profiles, and the turbulent intensity, are the Reynolds stresses in the wall-normal, streamwise, and spanwise. These are denoted by $\langle u'_j u'_j \rangle$, $\langle u'_i u'_i \rangle$, and $\langle u'_k u'_k \rangle$, respectively, where the repeating Einstein indices are not summations. These Reynolds stresses are normalized by the square of the maximum achieved freestream streamwise velocity, U_∞ . Figures A.8, A.9, A.10, and A.11 show the wall-normal profiles of the Reynolds wall stress at the ripple crest, trough, face, and averaged over the entire wavelength of the ripple. Figures A.12, A.13, A.14, and A.15 show the wall-normal profiles of the Reynolds streamwise stress at the ripple crest, trough, face, and averaged over the entire wavelength of the ripple. Figures A.16, A.17, A.18, and A.19 show the wall-normal profiles of the Reynolds spanwise stress at the ripple crest, trough, face, and averaged over the entire wavelength of the ripple. Looking at the individual profiles at the crest, trough, or face, all of these metrics show significant differences between the experimental and numerical data. But the data averaged over the entirety of the ripple wavelength shows much better agreement. The numerical model accurately predicts the shape and magnitude of the Reynolds wall stress profile. The Reynolds streamwise stress, however appears to be consistently over predicted by the numerical model. Additionally, the numerical model predicts large peaks in the Reynolds streamwise stress profiles that are not observed in the experimental data. In contrast, the Reynolds spanwise stress is grossly under-predicted at all locations, and even when it is averaged over the entire wavelength of the ripple.

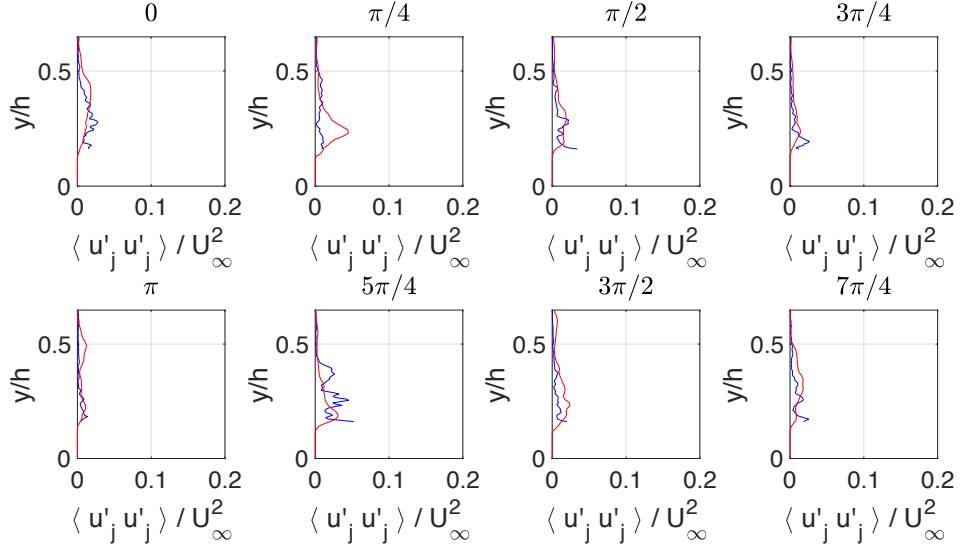


Figure A.8: Reynolds wall stress wall-normal profiles, at the ripple crest, shown at phase angles $\frac{n\pi}{4}$, for $n = 0, 1, \dots, 6, 7$. The Reynolds wall stress is normalized by the square of the maximum achieved freestream streamwise velocity, U_∞ . The wall-normal position is normalized by the half-height of the channel, h . The experimental results are denoted by a blue line, and the numerical results by a red line. In some cases, the range of the PIV data was limited, therefore, the entire profile was not available.

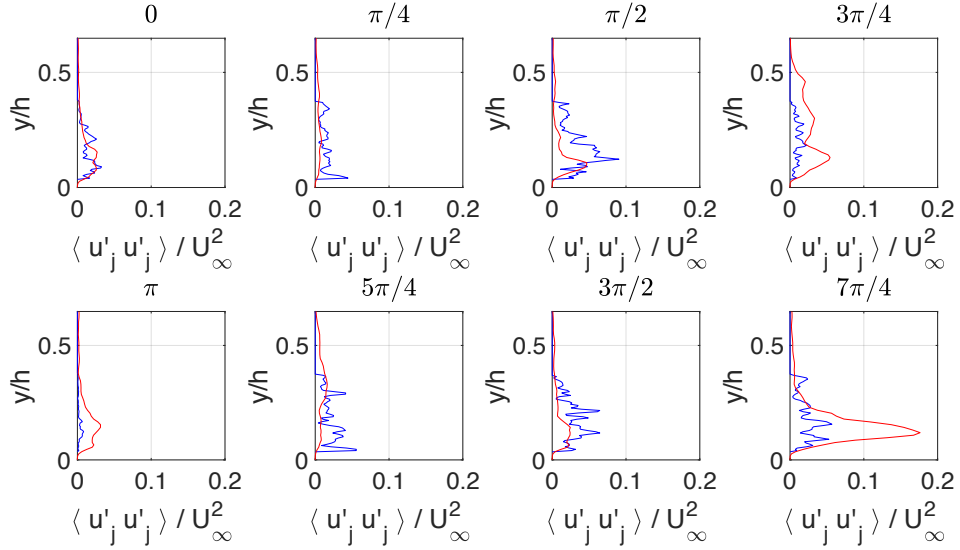


Figure A.9: Reynolds wall stress wall-normal profiles, at the ripple trough, shown at phase angles $\frac{n\pi}{4}$, for $n = 0, 1, \dots, 6, 7$. The Reynolds wall stress is normalized by the square of the maximum achieved freestream streamwise velocity, U_∞ . The wall-normal position is normalized by the half-height of the channel, h . The experimental results are denoted by a blue line, and the numerical results by a red line. In some cases, the range of the PIV data was limited, therefore, the entire profile was not available.

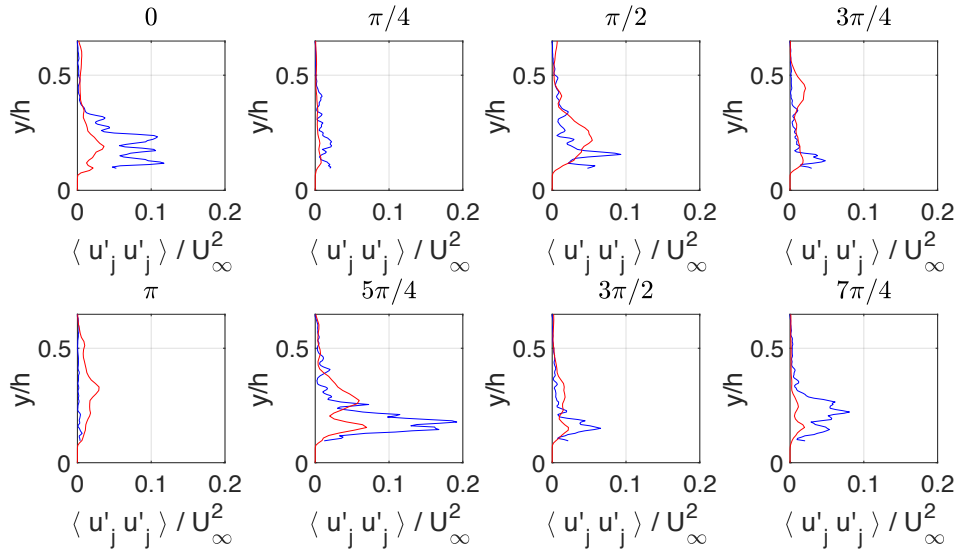


Figure A.10: Reynolds wall stress wall-normal profiles, at the ripple face, shown at phase angles $\frac{n\pi}{4}$, for $n = 0, 1, \dots, 6, 7$. The Reynolds wall stress is normalized by the square of the maximum achieved freestream streamwise velocity, U_∞ . The wall-normal position is normalized by the half-height of the channel, h . The experimental results are denoted by a blue line, and the numerical results by a red line. In some cases, the range of the PIV data was limited, therefore, the entire profile was not available.

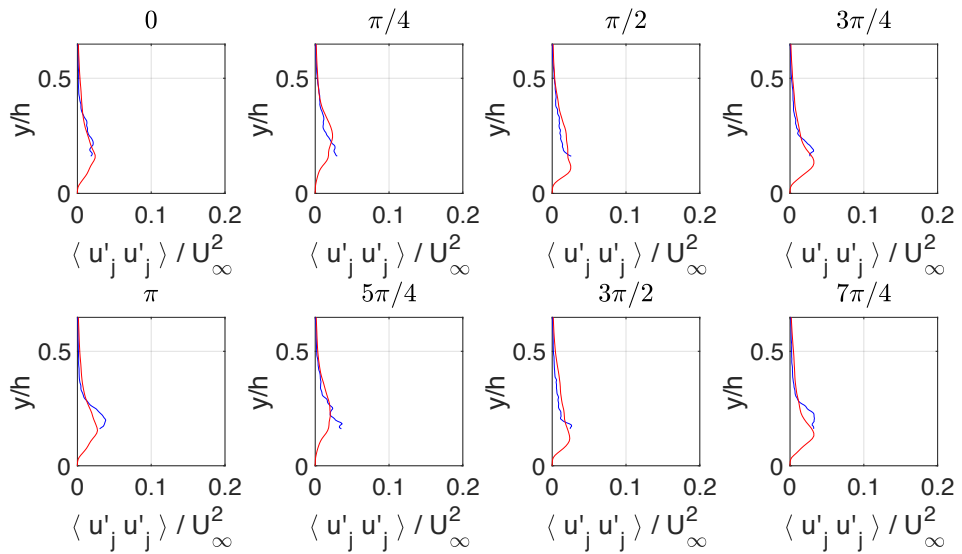


Figure A.11: Reynolds wall stress wall-normal profiles, averaged over the entire wavelength of the ripple, shown at phase angles $\frac{n\pi}{4}$, for $n = 0, 1, \dots, 6, 7$. The Reynolds wall stress is normalized by the square of the maximum achieved freestream streamwise velocity, U_∞ . The wall-normal position is normalized by the half-height of the channel, h . The experimental results are denoted by a blue line, and the numerical results by a red line. In some cases, the range of the PIV data was limited, therefore, the entire profile was not available.

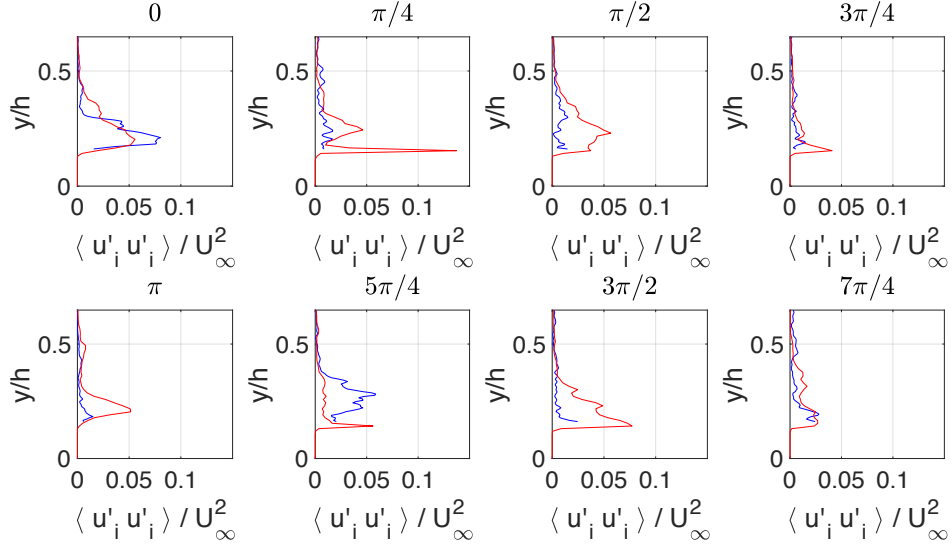


Figure A.12: Reynolds streamwise stress wall-normal profiles, at the ripple crest, shown at phase angles $\frac{n\pi}{4}$, for $n = 0, 1, \dots, 6, 7$. The Reynolds wall stress is normalized by the square of the maximum achieved freestream streamwise velocity, U_∞ . The wall-normal position is normalized by the half-height of the channel, h . The experimental results are denoted by a blue line, and the numerical results by a red line. In some cases, the range of the PIV data was limited, therefore, the entire profile was not available.

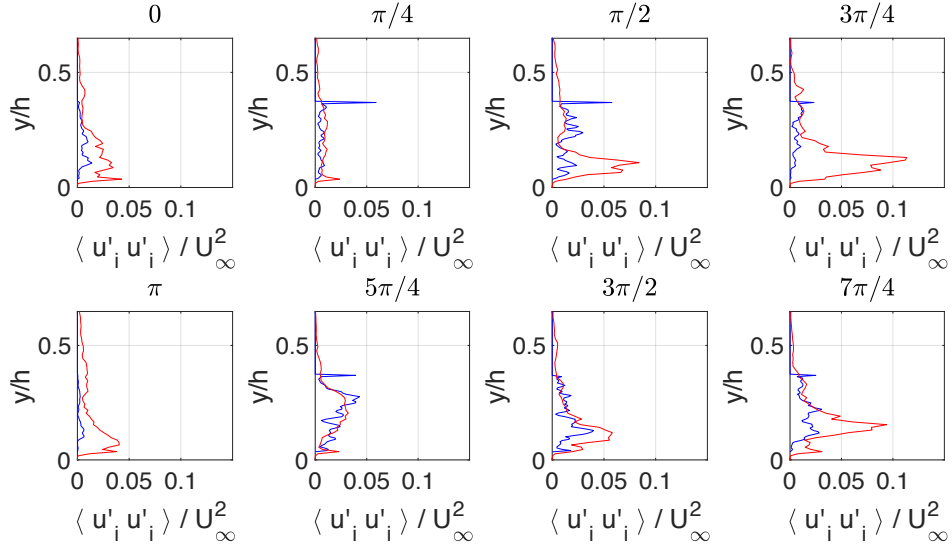


Figure A.13: Reynolds streamwise stress wall-normal profiles, at the ripple trough, shown at phase angles $\frac{n\pi}{4}$, for $n = 0, 1, \dots, 6, 7$. The Reynolds wall stress is normalized by the square of the maximum achieved freestream streamwise velocity, U_∞ . The wall-normal position is normalized by the half-height of the channel, h . The experimental results are denoted by a blue line, and the numerical results by a red line. In some cases, the range of the PIV data was limited, therefore, the entire profile was not available.

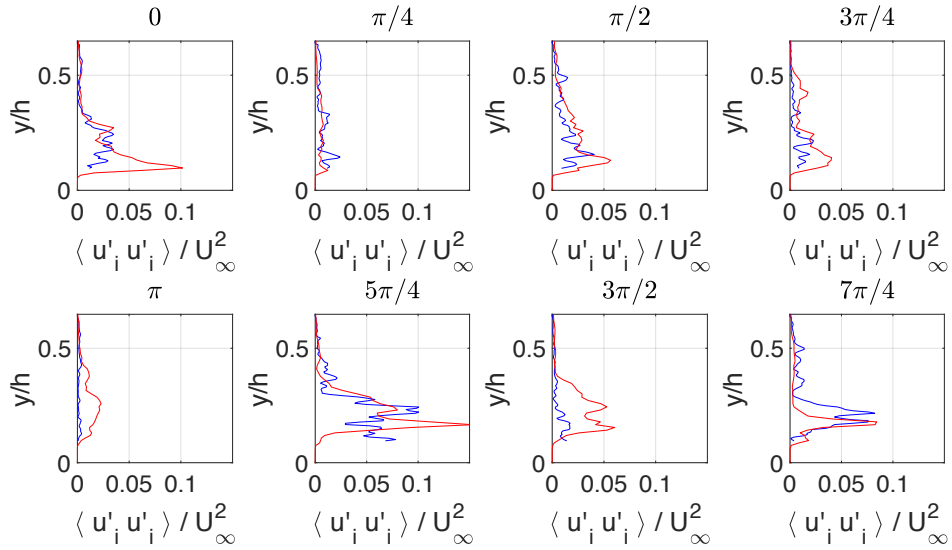


Figure A.14: Reynolds streamwise stress wall-normal profiles, at the ripple face, shown at phase angles $\frac{n\pi}{4}$, for $n = 0, 1, \dots, 6, 7$. The Reynolds wall stress is normalized by the square of the maximum achieved freestream streamwise velocity, U_∞ . The wall-normal position is normalized by the half-height of the channel, h . The experimental results are denoted by a blue line, and the numerical results by a red line. In some cases, the range of the PIV data was limited, therefore, the entire profile was not available.

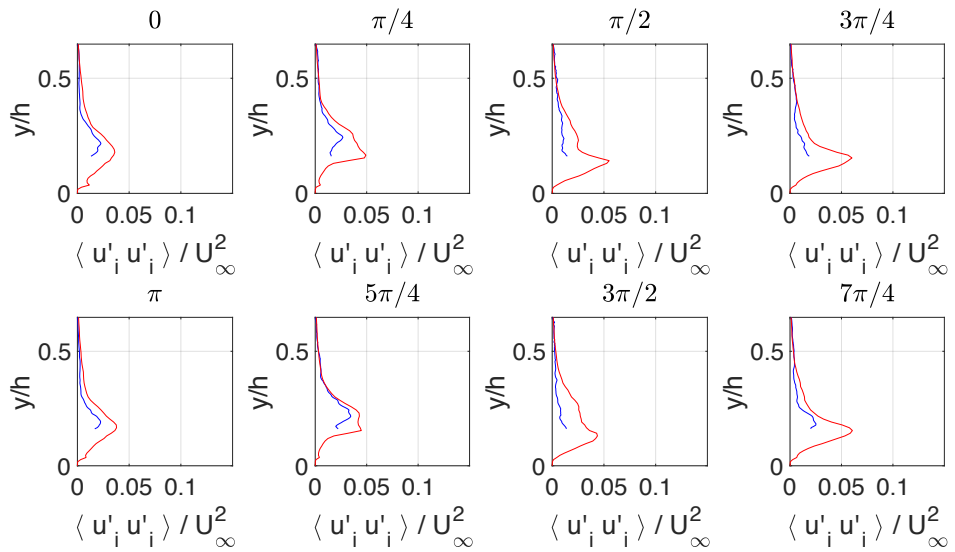


Figure A.15: Reynolds streamwise stress wall-normal profiles, averaged over the entire wavelength of the ripple, shown at phase angles $\frac{n\pi}{4}$, for $n = 0, 1, \dots, 6, 7$. The Reynold wall stress is normalized by the square of the maximum achieved freestream streamwise velocity, U_∞ . The wall-normal position is normalized by the half-height of the channel, h . The experimental results are denoted by a blue line, and the numerical results by a red line. In some cases, the range of the PIV data was limited, therefore, the entire profile was not available.

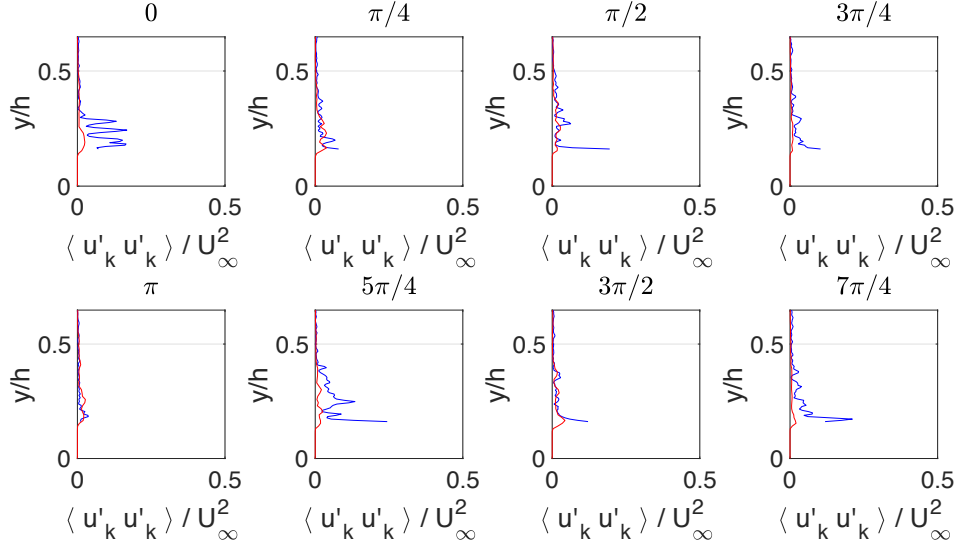


Figure A.16: Reynolds spanwise stress wall-normal profiles, at the ripple crest, shown at phase angles $\frac{n\pi}{4}$, for $n = 0, 1, \dots, 6, 7$. The Reynolds spanwise stress is normalized by the square of the maximum achieved freestream streamwise velocity, U_∞ . The wall-normal position is normalized by the half-height of the channel, h . The experimental results are denoted by a blue line, and the numerical results by a red line. In some cases, the range of the PIV data was limited, therefore, the entire profile was not available.

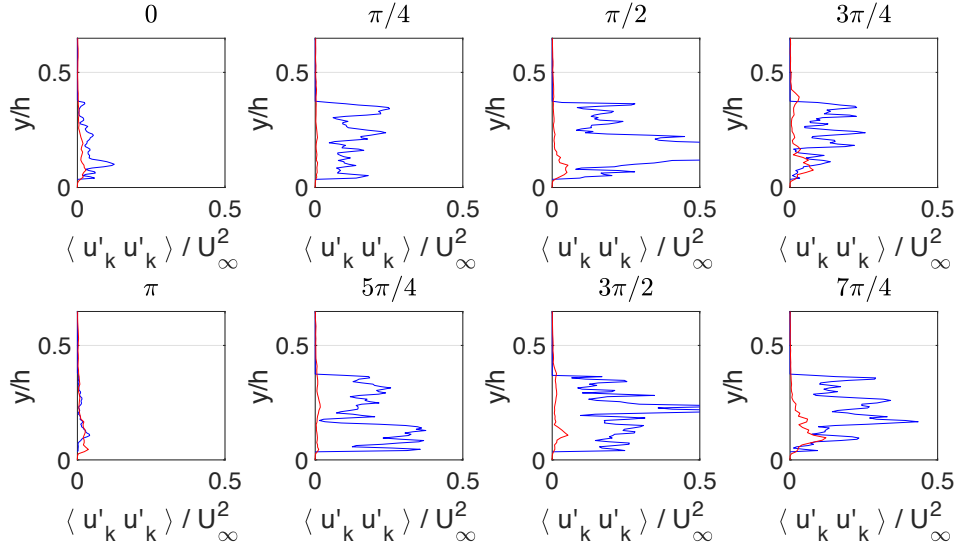


Figure A.17: Reynolds spanwise stress wall-normal profiles, at the ripple trough, shown at phase angles $\frac{n\pi}{4}$, for $n = 0, 1, \dots, 6, 7$. The Reynolds spanwise stress is normalized by the square of the maximum achieved freestream streamwise velocity, U_∞ . The wall-normal position is normalized by the half-height of the channel, h . The experimental results are denoted by a blue line, and the numerical results by a red line. In some cases, the range of the PIV data was limited, therefore, the entire profile was not available.

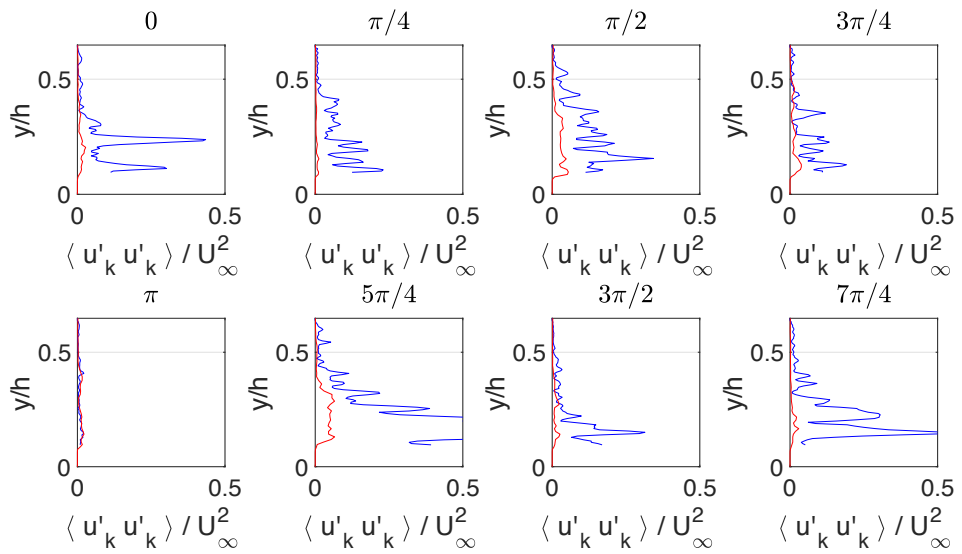


Figure A.18: Reynolds spanwise stress wall-normal profiles, at the ripple face, shown at phase angles $\frac{n\pi}{4}$, for $n = 0, 1, \dots, 6, 7$. The Reynolds spanwise stress is normalized by the square of the maximum achieved freestream streamwise velocity, U_∞ . The wall-normal position is normalized by the half-height of the channel, h . The experimental results are denoted by a blue line, and the numerical results by a red line. In some cases, the range of the PIV data was limited, therefore, the entire profile was not available.

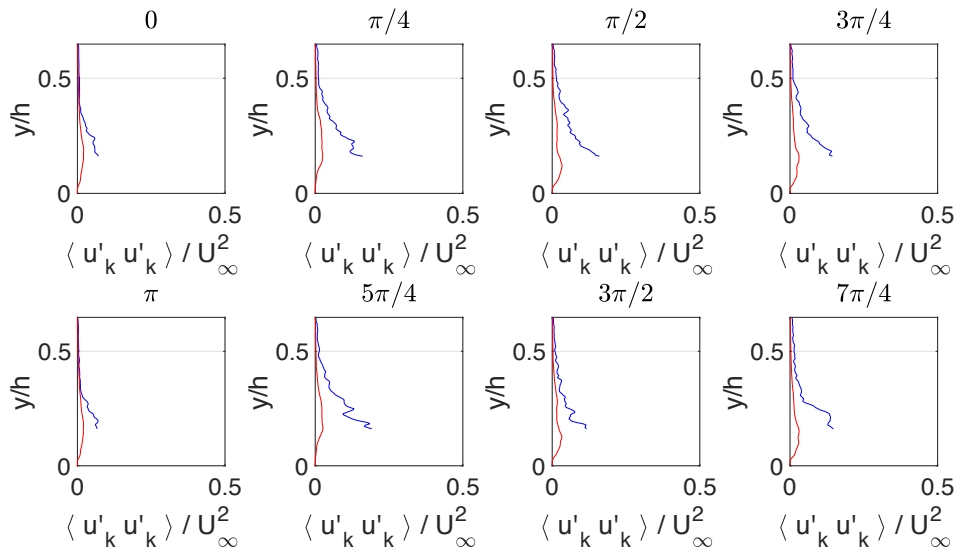


Figure A.19: Reynolds spanwise stress wall-normal profiles, averaged over the entire wavelength of the ripple, shown at phase angles $\frac{n\pi}{4}$, for $n = 0, 1, \dots, 6, 7$. The Reynold spanwise stress is normalized by the square of the maximum achieved freestream streamwise velocity, U_∞ . The wall-normal position is normalized by the half-height of the channel, h . The experimental results are denoted by a blue line, and the numerical results by a red line. In some cases, the range of the PIV data was limited, therefore, the entire profile was not available.

Appendix B: Integral Method

B.1 Fukagata Integral approach for two-dimensional wall-bounded flows

This core of this section is a summary of previous work by Ian Pond et al. (2017), and used with the courtesy of collaborator Meagan Wengrove. It has been modified for continuity in this context.

Following the approach of Fukugata (2002), for a two-dimensional, wall-bounded incompressible flow, the momentum equation becomes

$$-\frac{\partial \bar{p}}{\partial x} = \frac{\partial}{\partial y} \left[\bar{u}'v' - \frac{1}{Re_b} \frac{\partial \bar{u}}{\partial y} \right] + \bar{I}_x + \frac{\partial \bar{u}}{\partial t}, \quad (\text{B.1})$$

where \bar{I}_x contains the terms that appear when the flow is inhomogeneous in the streamwise direction.

$$\bar{I}_x = \frac{\partial \overline{(uu)}}{\partial x} + \frac{\partial \overline{(uv)}}{\partial y} - \frac{1}{Re_b} \frac{\partial^2 \bar{u}}{\partial x^2} \quad (\text{B.2})$$

And the Reynolds Averaging is shown as

$$f = \bar{f} + f'. \quad (\text{B.3})$$

For a RANS, not an LES or DNS, $\bar{I}_x = 0$, so

$$-\frac{\partial \bar{p}}{\partial x} = \frac{\partial}{\partial y} \left[\bar{u}'v' - \frac{1}{Re_b} \frac{\partial \bar{u}}{\partial y} \right] + \frac{\partial \bar{u}}{\partial t}. \quad (\text{B.4})$$

Using a control volume approach, and the definition of the skin friction coefficient, C_f ,

$$-\int_y \frac{\partial \bar{p}}{\partial x} = \frac{1}{8} C_f + \bar{I}_x = \frac{1}{8} C_f. \quad (\text{B.5})$$

Where,

$$C_f = \frac{\tau_w}{\frac{1}{2} \rho u_{bulk}^2} = \frac{8}{Re_{bulk}} \left. \frac{d\bar{u}}{dy} \right|_{wall}. \quad (\text{B.6})$$

Plugging Equation B.5 into Equation B.4 yields

$$\frac{1}{8} C_f = \frac{\partial}{\partial y} \left[\overline{u'v'} - \frac{1}{Re_b} \frac{\partial \bar{u}}{\partial y} \right] + \frac{\partial \bar{p}}{\partial x} - \int_y \frac{\partial \bar{p}}{\partial x} + \frac{\partial \bar{u}}{\partial t}. \quad (\text{B.7})$$

The integration process, $\int_0^1 dy \int_0^y dy \int_0^y dy$, yields the force balance after the first integration, the mean velocity profile after the second, and ultimately the flow rate from the velocity profile after the final integration. With $\int_0^1 \bar{u} dy = 1/2$, the triply integration equation becomes

$$\frac{1}{2} = Re_b \left[\frac{C_f}{24} - \int_0^1 (1-y)(-\overline{u'v'}) dy + \frac{1}{2} \int_0^1 (1-y)^2 dy \left(\frac{\partial \bar{p}}{\partial x} - \int_y \frac{\partial \bar{p}}{\partial x} + \frac{\partial \bar{u}}{\partial t} \right) dy \right]. \quad (\text{B.8})$$

Rearranging,

$$C_f = \underbrace{\frac{12}{Re_b}}_I + \underbrace{12 \int_0^1 2(1-y)(-\overline{u'v'}) dy}_{II} - \underbrace{12 \int_0^1 (1-y)^2 dy \left(\frac{\partial \bar{p}}{\partial x} - \int_y \frac{\partial \bar{p}}{\partial x} + \frac{\partial \bar{u}}{\partial t} \right) dy}_{III}. \quad (\text{B.9})$$

This equation represents the physical contributions of different components of the flow. The first term, I , is the laminar contribution from the mean flow. The second term, II , is the turbulent contribution. And, the third term, III , is the inhomogeneous/transient contribution. Finally, the wall shear stress can be backed out by using the definition of the skin friction coefficient,

$$C_f = \frac{\tau_w}{\frac{1}{2} \rho u_{bulk}^2}. \quad (\text{B.10})$$

Appendix C: Nelder-Mead Optimization technique

Although I was not able to complete the optimization of RANS-constants study, another student of my Advisor's has picked up where I left off. Appendices A, B, and C contain descriptions of the optimization technique, the RANS models to be optimized, and the Integral Method used to identify effectiveness of the constants used in the RANS solvers, respectively.

Initial point is defined by vector x_0 . To create the n -dimensional equal sided simplex, the points for $i = 1, \dots, n$ are generated by adding a vector to x_0 whose components are all b , except for the i^{th} component, which is set to a :

$$b = \frac{c}{n\sqrt{2}}(\sqrt{n+1} - 1), \quad (\text{C.1})$$

$$a = b + \frac{c}{\sqrt{2}} \quad (\text{C.2})$$

So, the new vectors, x_i are calculated as

$$x_i[\text{index} \neq i] = x_0[\text{index} \neq i] + b \quad (\text{C.3})$$

$$x_i[\text{index} = i] = x_0[\text{index} = i] + a \quad (\text{C.4})$$

The average of all points, except the worst, is calculated

$$x_a = \frac{1}{n} \sum_{i=1, i \neq w}^{n+1} x_i \quad (\text{C.5})$$

There are four basic operations. The first is reflection

$$x_r = x_a + \alpha(x_a - x_w), \quad \alpha = 1.0 \quad (\text{C.6})$$

Expansion

$$x_e = x_r + \gamma(x_r - x_a), \quad \gamma = 1.0 \quad (\text{C.7})$$

Inside contraction

$$x_c = x_a - \beta(x_a - x_w), \quad \beta = 0.5 \quad (\text{C.8})$$

Outside contaction

$$x_o = x_a + \beta(x_a - x_w), \quad \beta = 0.5 \quad (\text{C.9})$$

Shrinking

$$x_i = x_b + \rho(x_i - x_b), \quad \rho = 0.5 \quad (\text{C.10})$$

Operations are performed until a convergence criteria is met. Usually the size of the simplex must be below a certain threshold, where the size is calculated as

$$s = \sum_{i=1}^n |x_i - x_{n+1}|, \quad (\text{C.11})$$

or, in this case, the standard deviation of the function values at the simplex nodes

$$\sigma = \sqrt{\frac{\sum_{i=1}^{n+1} (f_i - \bar{f})^2}{n + 1}} \quad (\text{C.12})$$

where \bar{f} is the average of all functions values at all simplex nodes

$$\bar{f} = \frac{\sum_{i=1}^{n+1} f_i}{n + 1} \quad (\text{C.13})$$

C.1 Rosenbrock function example

Commonly used as performance test in optimization field due to function's non-convex behavior. Finding the minimum is trivial, but converging to it is not. The Rosenbrock function is

$$f(x, y) = (a - x)^2 + b(y - x^2)^2 \quad (\text{C.14})$$

$$a = 1, \quad b = 100 \quad (\text{C.15})$$

$$f_{min} @ (a, a^2) = (1, 1) \rightarrow f_{min} = 0 \quad (\text{C.16})$$

C.2 Application to Integral Method

Minimize the difference between the integral contribution to τ_w and q''_w between the DNS and the RANS solver.

$$\Delta_i = |i_{DNS} - i_{RANS}|, \quad i = I, II, III \quad (\text{C.17})$$

Where, as a reminder, the integral contributions to the shear wall stress are

$$\tau_w = \underbrace{\frac{2\mu}{y_t^2} \int_0^{y_t} U dy}_I - \underbrace{\frac{2\rho}{y_t^2} \int_0^{y_t} (y_t - y) \overline{u'v'} dy}_{II} - \underbrace{\frac{\rho}{y_t^2} \int_0^{y_t} (y_t - y)^2 \frac{\partial}{\partial y} \left[\nu \frac{\partial U}{\partial y} - \overline{u'v'} \right] dy}_{III}, \quad (\text{C.18})$$

And the contributions the wall heat flux are

$$q_w'' = \underbrace{\frac{2\lambda}{y_t^2} \int_0^{y_t} (\Theta_w - \Theta) dy}_{I*} + \underbrace{\frac{2\rho C_p}{y_t^2} \int_0^{y_t} (y_t - y) \bar{v' \theta'} dy}_{II*} + \underbrace{\frac{\rho C_p}{y_t^2} \int_0^{y_t} (y_t - y)^2 \frac{\partial}{\partial y} \left[\frac{\lambda}{\rho C_p} \frac{\partial \Theta}{\partial y} - \bar{v' \theta'} \right] dy}_{III*}. \quad (C.19)$$

where the difference between DNS and RANS is

$$\Delta_{i*} = |i*_{DNS} - i*_{RANS}|, \quad i* = I*, II*, III* \quad (C.20)$$

The convergence criteria, Cr , for this optimization process is to minimize the difference between integral contribution to τ_w and q_w'' between the DNS and the RANS solver. Therefore, for whichever integral contribution, Δ_i , is being minimized, the optimization algorithm is applied until

$$\Delta_i \leq Cr \quad (C.21)$$

Appendix D: 1D $k - \epsilon$ turbulence model code

Utilizing the $k - \epsilon$ turbulence model, a 1D code will be used to simulate a pulsatile channel flow. The pulsation flow will be driven by a sinusoidal pressure gradient in the streamwise direction.

D.1 Governing Equations

The general Navier-Stokes equations govern the flow. Respectively, the conservation of mass (continuity equation) and the conservation of momentum are

$$\frac{\partial u_i}{\partial x_i} = 0 \quad (\text{D.1})$$

and

$$\frac{\partial u_i}{\partial t} + u_j \frac{\partial u_i}{\partial x_j} = -\frac{1}{\rho} \frac{\partial p}{\partial x_i} + \nu \frac{\partial^2 u_i}{\partial x_j^2} + \frac{1}{\rho} P_{x,0} \cos(wt) \delta_{i1}. \quad (\text{D.2})$$

Temperature is solved as a passive scalar

$$\frac{\partial \theta}{\partial t} + u_j \frac{\partial \theta}{\partial x_j} = \frac{\nu}{Pr} \frac{\partial^2 \theta}{\partial x_j^2}, \quad (\text{D.3})$$

where $Pr = \nu/(\lambda/\rho Cp)$, λ is the fluid thermal conductivity and Cp is the fluid specific heat. Pr is assumed to be constant, $Pr = 0.7$.

D.2 Reynolds Averaged Navier-Stokes (RANS) Equations

By Reynolds' decomposition, the flow characteristics are broken into average and fluctuating components.

$$u_i(x_i, t) = U_i(x_i) + u'_i(x_i, t) \quad (\text{D.4})$$

$$U_i(x_i) = \lim_{T \rightarrow \infty} \frac{1}{T} \int_0^T u_i(x_i, t) \quad (\text{D.5})$$

Application of Reynolds' decomposition to Equation D.2, results in the Reynolds Averaged continuity equation

$$\frac{\partial U_i}{\partial x_i} = 0, \quad (\text{D.6})$$

The left hand side of momentum equation, Equation D.2, becomes

$$\text{Avg} \left[\frac{Du_i}{Dt} \right] = \frac{\partial U_i}{\partial t} + \frac{\partial \text{Avg}[u_i u_j]}{\partial x_j} \quad (\text{D.7})$$

The non-linear term becomes (where $\text{Avg}[\dots]$ is the average value of the contents of the brackets, $\text{Avg}[u_i] = U_i$)

$$\text{Avg}[u_i u_j] = \text{Avg}[(U_i + u'_i)(U_j + u'_j)] \quad (\text{D.8})$$

$$= \text{Avg}[U_i U_j + u'_j U_i + u'_i U_j + \text{Avg}[u'_i u'_j]] \quad (\text{D.9})$$

$$= \text{Avg}[U_i U_j] + \text{Avg}[u'_j U_i] + \text{Avg}[u'_i U_j] + \text{Avg}[u'_i u'_j] \quad (\text{D.10})$$

$$= U_i U_j + \text{Avg}[u'_i u'_j] \quad (\text{D.11})$$

Since

$$\text{Avg}[u'_j U_i] = \text{Avg}[u'_i U_j] = 0 \quad (\text{D.12})$$

Plugin Equation D.11 into Equation D.7

$$Avg\left[\frac{Du_i}{Dt}\right] = \frac{\partial U_i}{\partial t} + \frac{\partial [U_i U_j + Avg[u'_i u'_j]]}{\partial x_j} \quad (D.13)$$

$$= \frac{\partial U_i}{\partial t} + \frac{\partial [U_i U_j]}{\partial x_j} + \frac{\partial [Avg[u'_i u'_j]]}{\partial x_j} \quad (D.14)$$

$$= \frac{\partial U_i}{\partial t} + U_j \frac{\partial U_i}{\partial x_j} + U_i \frac{\partial U_j}{\partial x_j} + \frac{\partial [Avg[u'_i u'_j]]}{\partial x_j} \quad (D.15)$$

$$= \frac{\partial U_i}{\partial t} + U_j \frac{\partial U_i}{\partial x_j} + \frac{\partial [Avg[u'_i u'_j]]}{\partial x_j} \quad (D.16)$$

$$= \frac{\partial U_i}{\partial t} + U_j \frac{\partial U_i}{\partial x_j} + \frac{\partial [\overline{(u'_i u'_j)}]}{\partial x_j} \quad (D.17)$$

$$(D.18)$$

Here we have swapped the average of the product of the fluctuations for a correlation of the product.

$$Avg[u'_i u'_j] = \overline{(u'_i u'_j)} \quad (D.19)$$

And since, because a velocity average in a direction j , does not change with that direction, by definition,

$$\frac{\partial U_j}{\partial x_j} = 0 \quad (D.20)$$

The spatial derivative commutes with the averaging operation in the remaining terms. Therefore, the Reynolds Averaged momentum equation becomes

$$\frac{\partial U_i}{\partial t} + U_j \frac{\partial U_i}{\partial x_j} = -\frac{1}{\rho} \frac{\partial P}{\partial x_j} + \nu \frac{\partial^2 U_i}{\partial x_j^2} - \frac{\partial \overline{(u'_i u'_j)}}{\partial x_j}, \quad (D.21)$$

So, the Reynolds Averaged momentum equation is

$$\frac{\partial U_i}{\partial t} + U_j \frac{\partial U_i}{\partial x_j} = -\frac{1}{\rho} \frac{\partial}{\partial x_j} \left[P \delta_{ij} + \mu \left(\frac{\partial U_i}{\partial x_j} + \frac{\partial U_j}{\partial x_i} \right) - \overline{(u'_i u'_j)} \right], \quad (D.22)$$

The square brackets contain the stresses in the flow - the mean pressure field stress, the viscous stress, and the fluctuating velocity, or Reynolds', stresses. And, the scalar temperature equation becomes,

$$\frac{\partial \Theta}{\partial t} + U_j \frac{\partial \Theta}{\partial x_j} = \frac{\nu}{Pr} \frac{\partial^2 \Theta}{\partial x_j^2} - \frac{\partial \overline{(u'_j \theta')}}{\partial x_j}. \quad (\text{D.23})$$

Where an overbar is a correlation. The last term of Equation D.22, $-\overline{(u'_i u'_j)}$, is the Reynolds stresses due to fluctuating velocity. This equation cannot be solved directly, so the Reynolds stress term must be modeled.

D.3 Boussinesq approximation for the Reynolds stress tensor

Boussinesq proposed the use of an eddy viscosity, or “turbulent viscosity”, ν_T , by making an analogy between momentum transfer by molecular motion (molecular viscosity) and momentum transfer caused by turbulent eddies (“eddy viscosity”). The Boussinesq assumption asserts that the Reynolds stress tensor is proportional to the mean strain rate tensor:

$$\tau_{ij} = 2\mu_t S_{ij}^* - \frac{2}{3}\rho k \delta_{ij} \quad (\text{D.24})$$

The relation can also be written as

$$-\overline{(u'_i u'_j)} = \nu_T \left(\frac{\partial U_i}{\partial x_j} + \frac{\partial U_j}{\partial x_i} \right) - \frac{2}{3}k \delta_{ij} \quad (\text{D.25})$$

Keep in mind that i, j, k are Einstein notation indices only if they are subscripts. k in the last term of D.25 is the turbulent kinetic energy, which is half the trace of the Reynolds stress tensor,

$$k = \frac{1}{2} \overline{(u'_i u'_j)}. \quad (\text{D.26})$$

Plugging Equation D.25 into Equation D.22,

$$\frac{\partial U_i}{\partial t} + U_j \frac{\partial U_i}{\partial x_j} = \frac{\partial}{\partial x_j} \left[(\nu + \nu_T) \left(\frac{\partial U_i}{\partial x_j} + \frac{\partial U_j}{\partial x_i} \right) \right] - \frac{1}{\rho} \frac{\partial}{\partial x_j} \left(P \delta_{ij} + \frac{2}{3}k \delta_{ij} \right). \quad (\text{D.27})$$

Of course, determining the value of ν_T is the key.

D.4 High Reynolds number $k - \epsilon$ turbulence model

This high Reynolds number model does not require a refined grid at the wall due to the use of wall models. The first computational cell is placed in the log-law region (where $u^+ = \frac{1}{\kappa} \ln y^+ + C^+$), and the region between the wall and the first cell is assumed to be a viscous sublayer where $u^+ = y^+$. The closure of the eddy viscosity in the $k - \epsilon$ model is

$$\nu_T = C_\mu \frac{k^2}{\epsilon} \quad (\text{D.28})$$

Where C_μ is a constant, k is, again, the turbulent kinetic energy, and ϵ is the dissipation rate of turbulent kinetic energy. ν_T is determined by solving the transport equations for both k and ϵ ,

$$\frac{\partial k}{\partial t} + U_j \frac{\partial k}{\partial x_j} = \frac{\partial}{\partial x_j} \left[\left(\nu + \frac{\nu_T}{\sigma_k} \right) \frac{\partial k}{\partial x_j} \right] + \nu_T \left(\frac{\partial U_i}{\partial x_j} + \frac{\partial U_j}{\partial x_i} \right) \frac{\partial U_i}{\partial x_j} - \epsilon \quad (\text{D.29})$$

$$\frac{\partial \epsilon}{\partial t} + U_j \frac{\partial \epsilon}{\partial x_j} = \frac{\partial}{\partial x_j} \left(\frac{\nu_T}{\sigma_\epsilon} \frac{\partial \epsilon}{\partial x_j} \right) + C_{\epsilon 1} \frac{\epsilon}{k} \nu_T \left(\frac{\partial U_i}{\partial x_j} + \frac{\partial U_j}{\partial x_i} \right) \frac{\partial U_i}{\partial x_j} - C_{\epsilon 2} \frac{\epsilon^2}{k}. \quad (\text{D.30})$$

$C_\mu, \sigma_k, \sigma_\epsilon, C_{\epsilon 1}$, and $C_{\epsilon 2}$ are all constants.

The closure of the turbulent heat flux, $-\overline{(u'_j \theta')}$, is similar to the simple eddy viscosity approach. The Reynolds analogy assumes that the heat flux in a turbulent system is analogous to the momentum flux,

$$-\overline{(u'_j \theta')} = \frac{\nu_t}{Pr_T} \frac{\partial \Theta}{\partial x_j}. \quad (\text{D.31})$$

Where the turbulent Prandtl number is $Pr_T = \nu_T/\alpha_T$, and α_T is the turbulent thermal diffusivity. Pr_T is set to 0.9 for the RANS simulations. This closure is derived from the Reynolds analogy, which states that heat flux is analogous to the momentum flux. The temperature equation becomes

$$\frac{\partial \Theta}{\partial t} + U_j \frac{\partial \Theta}{\partial x_j} = \frac{\partial}{\partial x_j} \left[\left(\frac{\nu}{Pr} + \frac{\nu_T}{Pr_T} \right) \frac{\partial \Theta}{\partial x_j} \right]. \quad (\text{D.32})$$

D.5 Low Reynolds number $v^2 - f$ $k - \epsilon$ turbulence model

This low Reynolds number model requires that the grid is refined at the wall(s) and the first computational cell must be placed $y^+ = 1$.

$$\nu_T = C_\mu \overline{v'^2} T \quad (\text{D.33})$$

The standard $k - \epsilon$ equations are augmented by two more equations. The first is for the velocity fluctuation normal to the streamlines, which can provide the right scaling for the representation of damping near the wall,

$$\frac{\partial \overline{v'^2}}{\partial t} + U_j \frac{\partial \overline{v'^2}}{\partial x_j} = \frac{\partial}{\partial x_j} \left[\left(\nu + \frac{\nu_\tau}{\sigma_{v'^2}} \right) \frac{\partial \overline{v'^2}}{\partial x_j} \right] + kf - \frac{\overline{v'^2}}{k} \epsilon \quad (\text{D.34})$$

And the elliptic equation for the relaxation function is

$$L^2 \nabla^2 f - f = \frac{C_1 - 1}{T} \left(\frac{\overline{v'^2}}{k} - \frac{2}{3} \right) - C_2 \frac{P_k}{\epsilon} \quad (\text{D.35})$$

Where the turbulence length scale and turbulence time scale are, respectively,

$$L = C_L \max \left[\frac{k^{3/2}}{\epsilon}, C_\eta \left(\frac{\nu^3}{\epsilon} \right)^{1/4} \right] \quad (\text{D.36})$$

$$T = \max \left[\frac{k}{\epsilon}, C_T \left(\frac{\nu}{\epsilon} \right)^{1/2} \right] \quad (\text{D.37})$$

The constants are

$$C_\mu, \sigma_k, \sigma_\epsilon, C_{\epsilon 1}, C_{\epsilon 2} \quad (\text{D.38})$$

$$\sigma_{\overline{v'^2}}, C_1, C_2, C_T, C_L, C_\eta \quad (\text{D.39})$$

D.6 Low Reynolds Launder-Sharma $k - \epsilon$ turbulence model

$$\nu_T = C_\mu f_\mu \frac{k^2}{\tilde{\epsilon}} \quad (\text{D.40})$$

$$\frac{\partial k}{\partial t} + U_j \frac{\partial k}{\partial x_j} = \frac{\partial}{\partial x_j} \left[\left(\nu + \frac{\nu_\tau}{\sigma_k} \right) \frac{\partial k}{\partial x_j} \right] + \nu_T \left(\frac{\partial U_i}{\partial x_j} + \frac{\partial U_j}{\partial x_i} \right) \frac{\partial U_i}{\partial x_j} - (\tilde{\epsilon} + D) \quad (\text{D.41})$$

$$\frac{\partial \tilde{\epsilon}}{\partial t} + U_j \frac{\partial \tilde{\epsilon}}{\partial x_j} = \frac{\partial}{\partial x_j} \left(\frac{\nu_\tau}{\sigma_\epsilon} \frac{\partial \tilde{\epsilon}}{\partial x_j} \right) + C_{\epsilon 1} \frac{\tilde{\epsilon}}{k} \nu_T \left(\frac{\partial U_i}{\partial x_j} + \frac{\partial U_j}{\partial x_i} \right) \frac{\partial U_i}{\partial x_j} - C_{\epsilon 2} f_2 \frac{\tilde{\epsilon}^2}{k} + E. \quad (\text{D.42})$$

$$\tilde{\epsilon} = \epsilon + D \quad (\text{D.43})$$

$$D = 2\nu \left(\frac{\partial \sqrt{k}}{\partial n} \right)^2 \simeq 2\nu \left(\nabla \sqrt{k} \right)^2 \quad (\text{D.44})$$

$$E = 2\nu \nu_T \left(\frac{\partial^2 U}{\partial y^2} \right)^2 \quad (\text{D.45})$$

$$f_\mu = \exp \left(\frac{-3.4}{(1 + Re_T/50)^2} \right) \quad (\text{D.46})$$

$$f_2 = 1 - 0.3 \exp(-Re_T^2) \quad (\text{D.47})$$

$$Re_T = \frac{k^2}{\nu \tilde{\epsilon}} \quad (\text{D.48})$$

The constants for this model are

$$C_\mu, \sigma_k, \sigma_\epsilon, C_{\epsilon 1}, C_{\epsilon 2} \quad (\text{D.49})$$

D.7 $k - \omega$ turbulence model

$$\nu_T = \frac{k}{\omega} \quad (\text{D.50})$$

$$\frac{\partial k}{\partial t} + U_j \frac{\partial k}{\partial x_j} = \frac{\partial}{\partial x_j} \left[\left(\nu + \frac{\nu_\tau}{\sigma_k} \right) \frac{\partial k}{\partial x_j} \right] + \nu_T \left(\frac{\partial U_i}{\partial x_j} + \frac{\partial U_j}{\partial x_i} \right) \frac{\partial U_i}{\partial x_j} - \beta^* k \omega \quad (\text{D.51})$$

$$\frac{\partial \omega}{\partial t} + U_j \frac{\partial \omega}{\partial x_j} = \frac{\partial}{\partial x_j} \left[\left(\nu + \frac{\nu_\tau}{\sigma_\omega} \right) \frac{\partial \omega}{\partial x_j} \right] + \alpha \frac{\omega}{k} \left[\nu_T \left(\frac{\partial U_i}{\partial x_j} + \frac{\partial U_j}{\partial x_i} \right) \frac{\partial U_i}{\partial x_j} \right] - \beta \omega^2. \quad (\text{D.52})$$

$\sigma_k, \sigma_\omega, \alpha, \beta^*$ and β are all constants.

D.8 1D RANS Equations

The code will simulate a 1D channel flow, which is flow between two parallel infinite plates. It is assumed that the velocity is only non-zero in the streamwise (x) direction, but only *changes* in the y direction. Therefore, the 1D grid will be generated in the y direction. No-slip boundary conditions will be used ($u = 0$ at the walls).

Thus, for the 1D channel flow

$$v = w = 0, \quad (\text{D.53})$$

$$\frac{\partial u}{\partial x} = \frac{\partial u}{\partial z} = 0. \quad (\text{D.54})$$

And, the derivatives of v and w must be zero, since v and w are zero themselves (only the derivative $\frac{\partial u}{\partial y}$ is non-zero). Therefore, the convective terms disappears completely. The exact equation for the pressure gradient is

$$-\frac{1}{\rho} \frac{\partial}{\partial x_j} \left(P \delta_{ij} + \frac{2}{3} k \delta_{ij} \right) = H \cos(\omega t). \quad (\text{D.55})$$

So, pulsatile pressure gradient drives the flow and is applied essentially as a source term for the velocity. Finally, the 1D RANS equation becomes

$$\frac{\partial u}{\partial t} = \frac{\partial}{\partial y} \left[(\nu + \nu_T) \frac{\partial u}{\partial y} \right] + H \cos(\omega t). \quad (\text{D.56})$$

By the same approach, the transport equations for k and ϵ become, respectively,

$$\frac{\partial k}{\partial t} = \frac{\partial}{\partial y} \left[\left(\nu + \frac{\nu_T}{\sigma_k} \right) \frac{\partial k}{\partial y} \right] + \nu_T \left(\frac{\partial u}{\partial y} \right)^2 - \epsilon, \quad (\text{D.57})$$

and,

$$\frac{\partial \epsilon}{\partial t} = \frac{\partial}{\partial y} \left[\left(\frac{\nu_T}{\sigma_\epsilon} \right) \frac{\partial \epsilon}{\partial y} \right] + C_{\epsilon 1} \frac{\epsilon}{k} \nu_T \left(\frac{\partial u}{\partial y} \right)^2 - C_{\epsilon 2} \frac{\epsilon^2}{k}, \quad (\text{D.58})$$

Again,

$$\nu_T = C_\mu \frac{k^2}{\epsilon}. \quad (\text{D.59})$$

So, each gridpoint can a unique value of u , k , ϵ , and ν_T - they can change with both space and time. And, the five constants are σ_k , σ_ϵ , $C_{\epsilon 1}$, $C_{\epsilon 2}$, and C_μ .

D.9 Algorithm

The values of k , ϵ and, ultimately ν_T , are determined at each iteration. However, initial values are also required to begin the simulation. Since the flow will be purely driven by the pressure gradient, the simulation can be started with no flow, $u = 0$, for the entire domain. With these starting conditions, k and ϵ are zero,

and ν_T , likewise is assigned a value of zero. This effectively reduces to laminar initial equations, but once the pressure gradient begins to drive the flow, the ν_T will take on non-zero values.

D.10 Boundary Conditions

The no-slip wall condition requires that the velocity is always zero at the wall,

$$u\Big|_{wall} = 0. \quad (\text{D.60})$$

The turbulent kinetic energy is also always zero at the wall,

$$k\Big|_{wall} = 0. \quad (\text{D.61})$$

The dissipation rate of the turbulent kinetic energy at the wall is given by

$$\epsilon\Big|_{wall} = 0. \quad (\text{D.62})$$

D.11 Discretization

Equations D.56, D.57, and D.58 are solved in a similar way. Beginning with Equation D.56, the first term on the right hand side (RHS) of the equation will be discretized using a second order accurate scheme for non-linear diffusion (since ν_T changes with time and space)

$$\frac{\partial}{\partial y} \left[(\nu + \nu_T) \frac{\partial u}{\partial y} \right] = \frac{(\nu + \nu_T)_{j+1/2} \left(\frac{u_{j+1} - u_j}{y_{j+1} - y_j} \right) - (\nu + \nu_T)_{j-1/2} \left(\frac{u_j - u_{j-1}}{y_j - y_{j-1}} \right)}{y_{j+1/2} - y_{j-1/2}} \quad (\text{D.63})$$

Where the subscript is a spatial index. Since the grid will not necessarily be uniform, we cannot simply replace $y_{j+1/2} - y_{j-1/2}$ with Δy . Factoring out each term, and assigning $\Delta_{j+1}^2 = \frac{1}{(y_{j+1} - y_j)(y_{j+1/2} - y_{j-1/2})}$ and $\Delta_j^2 = \frac{1}{(y_j - y_{j-1})(y_{j+1/2} - y_{j-1/2})}$, Equation D.63 becomes

$$\left(\frac{(\nu + \nu_T)_{j-1/2}}{\Delta_j^2} \right) u_{j-1} + \left(- \frac{(\nu + \nu_T)_{j-1/2}}{\Delta_j^2} - \frac{(\nu + \nu_T)_{j+1/2}}{\Delta_{j+1}^2} \right) u_j + \left(\frac{(\nu + \nu_T)_{j+1/2}}{\Delta_{j+1}^2} \right) u_{j+1}. \quad (\text{D.64})$$

The temporal derivative, on the lefthand side (LHS) of the equation, is integrated using the Crank-Nicolson approach. Assigning the right hand side of Equation D.56 to *RHS*,

$$\frac{\partial u}{\partial t} = \frac{u_j^{n+1} - u_j^n}{\Delta t} = \frac{1}{2} \left[RHS^{n+1} + RHS^n \right], \quad (\text{D.65})$$

where the superscript is the time index. The full equation becomes

$$\begin{aligned} & \frac{u_j^{n+1} - u_j^n}{\Delta t} = \\ & \frac{1}{2} \left[\left(\frac{(\nu + \nu_\tau)_{j-1/2}^{n+1}}{\Delta_j^2} \right) u_{j-1}^{n+1} + \left(- \frac{(\nu + \nu_\tau)_{j-1/2}^{n+1}}{\Delta_j^2} - \frac{(\nu + \nu_\tau)_{j+1/2}^{n+1}}{\Delta_{j+1}^2} \right) u_j^{n+1} \right. \\ & \quad \left. + \left(\frac{(\nu + \nu_\tau)_{j+1/2}^{n+1}}{\Delta_{j+1}^2} \right) u_{j+1}^{n+1} + H \cos(\omega t^{n+1}) \right. \\ & \quad \left. + \left(\frac{(\nu + \nu_\tau)_{j-1/2}^n}{\Delta_j^2} \right) u_{j-1}^n + \left(- \frac{(\nu + \nu_\tau)_{j-1/2}^n}{\Delta_j^2} - \frac{(\nu + \nu_\tau)_{j+1/2}^n}{\Delta_{j+1}^2} \right) u_j^n \right. \\ & \quad \left. + \left(\frac{(\nu + \nu_\tau)_{j+1/2}^n}{\Delta_{j+1}^2} \right) u_{j+1}^n + H \cos(\omega t^n) \right]. \end{aligned} \quad (\text{D.66})$$

D.12 The tridiagonal system

Once the system has been fully discretized, like terms must be grouped together. To calculate the values of u^{n+1} , at terms at time $n + 1$ are grouped on the left hand side of the equation. The remaining terms are grouped on the right hand side. All terms on the right hand side are known quantities.

$$\begin{aligned} & A_j^{n+1} u_{j-1}^{n+1} + B_j^{n+1} u_j^{n+1} + C_j^{n+1} u_{j+1}^{n+1} \\ & = A_j^n u_{j-1}^n + B_j^n u_j^n + C_j^n u_{j+1}^n + \frac{\Delta t}{2} H \cos(\omega t^{n+1}) + \frac{\Delta t}{2} H \cos(\omega t^n), \end{aligned} \quad (\text{D.67})$$

where the coefficients are

$$\begin{aligned} A_j^{n+1} &= -\frac{\Delta t}{2} \frac{(\nu + \nu_\tau)_{j-1/2}^{n+1}}{\Delta_j^2}, \\ B_j^{n+1} &= 1 - \frac{\Delta t}{2} \left[-\frac{(\nu + \nu_\tau)_{j-1/2}^{n+1}}{\Delta_j^2} - \frac{(\nu + \nu_\tau)_{j+1/2}^{n+1}}{\Delta_{j+1}^2} \right], \\ C_j^{n+1} &= -\frac{\Delta t}{2} \frac{(\nu + \nu_\tau)_{j+1/2}^{n+1}}{\Delta_{j+1}^2}. \end{aligned} \quad (\text{D.68})$$

The values of A , B , and C at time n are calculated in a similar way, but are known from the previous timestep so they don't have to be recalculated. Since the values of k , ϵ , ν_T , and the velocity field u are known at time n , the right hand side of Equation D.67 is known (the pressure gradient terms can be calculated exactly with time values at n and $n + 1$). So, the right hand side becomes

$$R_j^n = A_j^n u_{j-1}^n + B_j^n u_j^n + C_j^n u_{j+1}^n + \frac{\Delta t}{2} H[\cos(\omega t^{n+1}) + \cos(\omega t^n)] \quad (\text{D.69})$$

Therefore, the set of implicit equations is tridiagonal

$$\left(\begin{array}{ccccccc} B_0^{n+1} & C_0^{n+1} & 0 & \cdot & \cdot & 0 & 0 \\ A_1^{n+1} & B_1^{n+1} & C_1^{n+1} & 0 & \cdot & \cdot & 0 \\ 0 & A_2^{n+1} & B_2^{n+1} & C_2^{n+1} & 0 & \cdot & 0 \\ & \cdot & \cdot & \cdot & & & \\ 0 & \cdot & 0 & A_{N-1}^{n+1} & B_{N-1}^{n+1} & C_{N-1}^{n+1} & 0 \\ 0 & \cdot & \cdot & 0 & A_N^{n+1} & B_N^{n+1} & C_N^{n+1} \\ 0 & \cdot & \cdot & \cdot & \cdot & 0 & A_{N+1}^{n+1} & B_{N+1}^{n+1} \end{array} \right) \begin{pmatrix} u_0^{n+1} \\ u_1^{n+1} \\ u_2^{n+1} \\ \vdots \\ u_{N-1}^{n+1} \\ u_N^{n+1} \\ u_{N+1}^{n+1} \end{pmatrix} = \begin{pmatrix} R_0^n \\ R_1^n \\ R_2^n \\ \vdots \\ R_{N-1}^n \\ R_N^n \\ R_{N+1}^n \end{pmatrix} \quad (\text{D.70})$$

Since the code is written in Python, the first index is $j = 0$. The indices $j = 0$ and $j = N + 1$ are at the bottom and top walls, respectively. The grid is staggered - the velocity is stored at each of the $N + 1$ cell faces, and the viscosity is stored at each of the N cell centers. This approach obviates any interpolation calculations, which are potential sources of error.

D.13 Solving the tridiagonal system using the Thomas algorithm

Since the system is tridiagonal, a computationally expensive matrix inversion does not have to be used. Instead the Thomas algorithm is used. The Thomas algorithm is stable when the matrix is diagonally dominant, which means that the magnitude of the diagonal entry is greater than or equal to the sum of all the non-diagonal terms from the same row. In this case, that requires that

$$|B_j| \geq |A_j| + |C_j|. \quad (\text{D.71})$$

Plugging in Equations D.68, and noting that the $(\nu + \nu_\tau)$ terms must always be positive,

$$\begin{aligned} \left| 1 - \frac{\Delta t}{2} \left[-\frac{(\nu + \nu_\tau)_{j-1/2}^{n+1}}{\Delta_j^2} - \frac{(\nu + \nu_\tau)_{j+1/2}^{n+1}}{\Delta_{j+1}^2} \right] \right| &\geq \left| -\frac{\Delta t}{2} \frac{(\nu + \nu_\tau)_{j-1/2}^{n+1}}{\Delta_j^2} \right| + \left| -\frac{\Delta t}{2} \frac{(\nu + \nu_\tau)_{j+1/2}^{n+1}}{\Delta_{j+1}^2} \right| \\ 1 + \frac{\Delta t}{2} \frac{(\nu + \nu_\tau)_{j-1/2}^{n+1}}{\Delta_j^2} + \frac{\Delta t}{2} \frac{(\nu + \nu_\tau)_{j+1/2}^{n+1}}{\Delta_{j+1}^2} &\geq \frac{\Delta t}{2} \frac{(\nu + \nu_\tau)_{j-1/2}^{n+1}}{\Delta_j^2} + \frac{\Delta t}{2} \frac{(\nu + \nu_\tau)_{j+1/2}^{n+1}}{\Delta_{j+1}^2} \\ 1 &\geq 0 \end{aligned} \quad (\text{D.72})$$

Thus, the diagonal elements are always greater than the sum of the remaining elements, and, therefore, the matrix is diagonally dominant, and unconditionally stable. (Equation D.72 also highlights that the coefficient on the diagonal $B_j = 1 - A_j - C_j$.)

The Thomas algorithm is an application of Gaussian elimination, modified for the specific case of tridiagonal matrices. Starting with the second row, the first row is used to eliminate the A coefficient of the second row. Then, the A coefficient of the third row is eliminated using the modified second row. This process is repeated until the final row, which leaves only the B coefficient, and thus produces the solution for the last value of u at time $n + 1$. This value is then used to determine the second to last value of u , via the second to last row. This back-substitution is repeated until the first value of u , from the first row, is determined.

This process produces complicated modified coefficients, but they can be defined recursively. Cn_j and Rn_j are the modified versions of the C_j and R_j coefficients

$$Cn_j = \begin{cases} \frac{C_j}{B_j}, & j = 0, \\ \frac{C_j}{B_j - A_j Cn_{j-1}}, & j = 1, 2, 3, \dots, N, \end{cases} \quad (\text{D.73})$$

$$Rn_j = \begin{cases} \frac{R_j}{B_j}, & j = 0, \\ \frac{R_j - A_j Rn_{j-1}}{B_j - A_j Cn_{j-1}}, & j = 1, 2, 3, \dots, N. \end{cases} \quad (\text{D.74})$$

Then, back-substitution produces the solution,

$$\begin{aligned} u_N &= Rn_N \\ u_j &= Rn_j - Cn_j u_{j+1}. \end{aligned} \quad (\text{D.75})$$

Since the equations for k and ϵ are similar to the equation for u , the same approach is used to solve those equations.

D.14 Simulation parameters

The square of the Womersley number, α^2 , is the ratio of the diffusion time scale to the oscillation time scale.

$$\alpha = h \sqrt{\frac{\omega}{\nu}} \quad (\text{D.76})$$

$$h = \text{channel half height} \quad (\text{D.77})$$

$$\omega = 2\pi/T \quad (\text{D.78})$$

$$\nu = \text{kinematic viscosity} \quad (\text{D.79})$$

$$T = \text{period of oscillation} \quad (\text{D.80})$$

$$Re_{peak} = \frac{2U_{max}h}{\nu} \quad (\text{D.81})$$

$$Re_{Stokes} = \frac{U_{max}l_{Stokes}}{\nu} \quad (\text{D.82})$$

$$l_{Stokes} = \sqrt{2\nu/\omega} \quad (\text{D.83})$$